ABSTRACT

Title of Dissertation:	A CYBER-PHYSICAL APPROACH TO THE OPTIMAL DESIGN OF CIVIL STRUCTURES USING BOUNDARY LAYER WIND TUNNELS AND MECHATRONIC MODELS
	Michael Lee Whiteman II, Doctor of Philosophy, 2020
Dissertation directed by:	Associate Professor, Brian M. Phillips, Department of Civil & Environmental Engineering, University of Maryland

The threat of wind-related hazards to vulnerable coastal locations necessitates the development of economical approaches to design and construct resilient buildings. This study investigates using a cyber-physical systems (CPS) approach as a replacement for traditional trial-and-error methods for civil infrastructure design for wind loads. The CPS approach combines the accuracy of boundary layer wind tunnel (BLWT) testing with the efficiency of numerical optimization algorithms. The approach is autonomous: experiments are executed in a BLWT, sensor feedback is monitored and analyzed, and optimization algorithms dictate physical changes to the model through actuators. The cyberinfrastructure for this project was developed with the collaboration of multiple researchers at the University of Florida Experimental

Facility (UFEF) under the Natural Hazard Engineering Research Infrastructure (NHERI) program.

A proof-of-concept was developed to optimally design the parapet wall of a low-rise building. Parapet walls nominally reduce suction loads on the roof but lead to an increase in positive roof pressure and base shear. A mechatronic low-rise building model was created with a parapet wall of adjustable height for BLWT testing. Various single-objective optimization algorithms were implemented to minimize the magnitude of roof wind pressures. Multi-objective optimization was used to simultaneously minimize both the magnitude of roof suction pressures and building base shear. A multi-objective procedure can consider the competing objectives of multiple stakeholders often present in engineering design.

The CPS approach was extended to optimize the performance of a landmark tall building for wind loads. A 1:200 multi-degree-of-freedom (MDOF) aeroelastic model was created to represent the building in a BLWT. Aeroelastic models directly simulate the scaled dynamic behavior of the building including effects of aerodynamic damping, vortex shedding, coupling within modes, and higher modes. The model was equipped with a series of variable stiffness devices (adjustable leaf springs) in the base to enable quick adjustments to the model's dynamics. Additionally, the model was equipped with an active fin system (AFS) consisting of individually controllable fins installed at the four corners to modify the building aerodynamics and suppress vortex-induced vibrations. Multiple design problems were explored where the model's dynamics and aerodynamics were refined using heuristic optimization algorithms to minimize costs while satisfying acceleration and drift limits.

The traditional design process for wind requires lengthy collaboration between designers and wind tunnel operators. This process may include the construction of a limited set of building models, leading to a non-exhaustive exploration of potential designs. Using mechatronic models guided by optimization algorithms enables optimum designs to be attained quicker than conventional methods. In future work, the proposed cyber-physical framework can be expanded to integrate machine learning and other computational tools to improve efficiency and reduce the reliance on experimental testing.

A CYBER-PHYSICAL APPROACH TO THE OPTIMAL DESIGN OF CIVIL STRUCTURES USING BOUNDARY LAYER WIND TUNNELS AND MECHATRONIC MODELS

by

Michael Lee Whiteman II

Dissertation submitted to the Faculty of the Graduate School of the
University of Maryland, College Park, in partial fulfillment
of the requirements for the degree of
Doctor of Philosophy
2020

Advisory Committee:
Professor Brian M. Phillips, Chair
Professor Amde M. Amde
Dr. Dat Duthinh
Professor Chung C. Fu
Professor Norman M. Wereley

Dedication

To my family.

Acknowledgements

I would like to express my sincere thanks to my advisor, Professor Brian M. Phillips for his continued advice and support during my graduate studies, and for his encouragement to pursue further graduate studies at the University of Maryland. He opened up a world of opportunities for me. Under his guidance, I developed both academic and professional skills that will ensure my future success. I am honored to have studied in his group and will keep the experience and insight that I gained with me for my entire life.

I sincerely appreciate the time and efforts of my committee members, Professor Amde M. Amde, Professor Chung C. Fu, Dr. Dat Duhinh, and Professor Norman M. Wereley. Their comments and suggestions have enriched my dissertation and are greatly appreciated. Additionally, I would like to thank Professor Phillips, Professor Peter C. Chang, and Professor Fu for serving on my candidacy exam committee and helping to bolster my dissertation preparations.

The research of this dissertation is based upon work supported by the National Science Foundation (NSF) under Grant No. 1636039. This support was gratefully appreciated. Any opinions, findings, and conclusions or recommendations expressed in this material are those of the author and do not necessarily reflect the views of NSF. I also acknowledge the NSF Natural Hazard Engineering Research Infrastructure (NHERI) awardee that contributed to the research results reported within this dissertation under Grant No. 1520843: Natural Hazards Engineering Research Infrastructure: Experimental Facility with Boundary Layer Wind Tunnel, Wind Load and Dynamic Flow Simulators, and Pressure Loading Actuators

(University of Florida) and Grant No. 1520817: Natural Hazards Engineering Research Infrastructure: Cyberinfrastructure (DesignSafe).

I would like to thank Professor Forrest J. Masters, Professor Jennifer A. Bridge, and Dr. Justin R. Davis for their conceptualization efforts and guidance throughout the research during weekly meetings. I appreciate the help of Professor Pedro Luis Fernández-Cabán for his friendship, guidance, and significant contributions to the research presented in this dissertation during his tenure as a postdoctoral researcher at the University of Maryland. I would like to offer my appreciation to my fellow graduate students and friends, Parteek Middha, Meru Pathak, Jingzhe Wu, and Ruiyang Zhang, for their collaboration and assistance, as well as inspiring discussions on research. Finally, I would like to thank and acknowledge the staff of the Powell Structures and Materials Laboratory at the University of Florida for their dedication to ensuring that all wind tunnel testing went as smoothly as possible. Their passionate involvement certainly made all testing possible.

Last but not least, I would like to thank my friends and family for their endless support and encouragement – especially my wife, Kathleen, for being a source of advice, respect, reassurance, and love and my brother, Richard, for always being willing to help me or offer advice whenever I have needed his assistance. Moreover, I would like to thank my parents, Kirk and Christina, for their endless support and understanding as I pursued my goals. Without their love and support I would never be the person who I am today. I love you both.

Table of Contents

List of Tables

List of Figures

List of Abbreviations

AFS	Active fin system
BLWT	Boundary layer wind tunnel
CFD	Computational fluid dynamics
CPS	Cyber physical system
ETE	Explore-then-exploit
GSS	Golden section search
LIMO	Loop-in-the-model optimization
MO-PSO	Multi-objective particle swarm optimization
MRI	Mean recurrence interval
NHERI	Natural Hazard Engineering Research Infrastructure
NI	National Instruments
NSF	National Science Foundation
PSO	Particle swarm optimization
RTHS	Real-time hybrid simulation
SO-PSO	Single-objective particle swarm optimization
VSD	Variable stiffness device

Chapter 1: Introduction

1.1 Background and motivation

The number of deaths from severe wind-related weather events (e.g., tornados, hurricanes, and tropical storms) comprised 34.3% of all deaths from natural disasters in the United States from 2000 through 2018 and accounted for a combined $211.57B of property damages (National Weather Service, 2001 – 2019). Wind-related hazards have the potential to become an increasing threat as vulnerable coastal locations within the United States continue to see steady population growth but lack a corresponding increase in evacuation route capacity (Cohen, 2019). As a result, many coastal cities will have to rely on shelter-in-place strategies. The significant loss of life and economic loss due to wind-related weather events and the expected population increase in vulnerable areas highlight the ongoing need to develop new economical means to deliver buildings capable of surviving extreme wind events.

A boundary layer wind tunnel (BLWT) is the primary tool in wind engineering to characterize the pressure loading on wind-sensitive structures. In particular, BLWT testing is valuable when studying new structures for which the simplified provisions of ASCE 7 are inadequate or computational fluid dynamics (CFD) approaches cannot be applied with confidence (ASCE 7-16). Recent advances in computationally-based optimization techniques for structural design allow for the examination of more complex structures. Meta-heuristic algorithms such as particle swarm and genetic algorithms are problem-independent algorithms that efficiently explore a complex solution space, providing new opportunities to study multi-variate and multi-objective optimization problems. New optimization techniques are promising for delivering cost-effective design solutions, but they must be combined with methods such as BLWT testing to accurately evaluate the candidate solutions under wind loads.

This dissertation proposes the use of cyber-physical systems for optimal design in wind engineering. The approach is fully automated, with experiments executed in a BLWT, sensor feedback monitored by a high-performance computer, and optimization techniques used to bring about physical changes to the structural model in the BLWT. Because the model is undergoing physical change as it approaches the optimal solution, this approach is given the name “loop-in-the-model” testing.

There are two buildings selected for independent study; first, a low-rise building with a parapet wall and second, a landmark tall building. Parapets are common on industrial and commercial buildings and help to alleviate extreme roof wind loads (Kopp et al., 2005a; Kopp et al., 2005b; Kopp et al., 2005c; Mans et al., 2005). Parapet walls alter the location of the roof corner vortex, mitigating the extreme corner and edge suction loads on the roof of the building. Conversely, parapet walls increase the downward roof wind loads which combine with other roof loads. This influence from parapet height on roof wind loads creates an interesting optimal structural design problem. The determination of an optimal parapet height using the traditional design guidance of ASCE 7-16 is difficult due to the lack of refinement in regard to the distribution of parapet loading.

A mechatronic model was created with a variable height parapet wall to capture the impact of parapet height on building performance. The model's parapet height is adjusted automatically using servo-motors to reach a particular candidate design. The building envelope is instrumented with pressure taps to measure the envelope pressure loading. The taps are densely spaced on the roof and uniformly spaced elsewhere to provide sufficient resolution to capture the change in roof corner vortex formation and the behavior of wind on the remaining structure, respectively.

The second building selected for this study is a tall building represented as an aeroelastic model in the BLWT. To capture the impact of design decisions regarding building dynamics and aerodynamics, the model has an independently adjustable stiffness and aerodynamic shape. The stiffness properties govern the natural frequency of the building and affect the structure's dynamic response to loading (i.e., displacements and accelerations). Increasing the building's stiffness reduces overall deflections. Conversely, a stiffer building increases the accelerations which affect occupant comfort. The aerodynamic properties (e.g., external shape of the building) significantly alter the wind-structure interaction and either mitigate or intensify the structural dynamic response. The influence from stiffness and aerodynamics on the structural dynamic response of the building sets up an interesting optimal design problem with non-trivial solutions. The determination of an optimal stiffness using the traditional design guidance of ASCE 7-16 is difficult due to the simplified provisions, while the determination of an optimal shape using CFD is difficult due to the challenge with numerically modeling the turbulent flow around bluff bodies.

In the BLWT, the model stiffness is adjusted automatically using servo-motors and variable stiffness devices (VSDs) to reach a particular candidate design. The physical adjustment of the aerodynamic properties (i.e., shape) of the specimen is achieved through stepper motors and an active fin system (AFS) consisting of individually controllable fin assemblies. The model's structural spine is instrumented with accelerometers to measure accelerations along the height of the building and laser displacement sensors to capture deflections at the mid-height and top of the building. Both accelerations and deflections are captured in the local along and cross-wind directions. All experiments are conducted using a BLWT located at the University of Florida Natural Hazard Engineering Research Infrastructure (NHERI) Experimental Facility.

1.2 Overview of dissertation

This dissertation uses cyber-physical systems (CPS) to optimize the structural design of both a low-rise building with parapet walls and a tall building with independently adjustable stiffness properties and aerodynamic shape. The focus of this dissertation is the development of a cyber-physical approach to the optimal design of structures for wind hazards. The overall goal of this research is to improve the efficiency and accuracy of the optimization process for wind-sensitive structures under user-specified objectives. This study investigates design parameters that have a non-monotonic influence on the performance of wind-sensitive structures. A description of the contents of each chapter is provided below.

Chapter 2 contains a detailed review of current knowledge regarding the effect of wind on both low-rise buildings with parapets and tall buildings and previous studies on different optimization techniques. A review of current practices using BLWTs and constructing building models is also presented.

Chapters 3 and 4 cover the BLWT model design and CPS optimization of a low-rise building with a parapet wall. Chapter 3 discusses the experimental equipment and sensor instrumentation used for the BLWT testing of the low-rise parapet model. The method of processing the measured pressure data into the non-dimensional pressure coefficient C_p and the application of the Gumbel distribution to obtain the maximum and minimum C_p values is explained as well. The model development is described, including the geometry, scaling, a description of the materials and components which are used in the model's fabrication, and the physically adjustable model design variable of the outer parapet wall height.

Chapter 4 presents the setup and results of the different optimization runs obtained using the low-rise model. A combination of non-stochastic and stochastic single-objective algorithms were implemented for separate optimization runs to minimize the magnitude of suction and positive pressures on the roof, followed by stochastic multi-objective optimization to simultaneously minimize the magnitude of suction pressures and minimize base shear.

Chapters 5 through 9 cover the BLWT model design and CPS optimization of a tall building. Chapter 5 discusses the experimental equipment and sensor instrumentation used for the aeroelastic, tall building model. The process for integrating Kalman filtering to estimate the full-scale building response is introduced.

The development of the aeroelastic model is described, including the model geometry and scaling, as well as the materials and components which are used in the model's fabrication.

Chapter 6 introduces the variable stiffness devices (VSDs), the physically-adjustable actuation device to adjust the model structural dynamic properties (i.e., stiffness). The initial system identification to validate the VSDs and the cyber-physical setup for dynamic optimization are presented as well.

Chapter 7 covers experimental results and discussion using the VSDs to optimize the building's dynamics. A test matrix exploring the impact of VSD length on building performance is first presented. The approach to optimal design considering model stiffness is then presented, and the results of the different optimization runs obtained are subsequently presented. Stochastic single-objective algorithms were implemented for separate optimization runs to minimize the acceleration or displacement responses of the structure.

Chapter 8 introduces the mechanics of an active fin system (AFS) for modifying the building model's aerodynamics. The cyber-physical setup for aerodynamic optimization and the approach to performing aerodynamic optimization is subsequently introduced.

Chapter 9 covers the experimental results and discussion using the AFS to optimize the building's aerodynamics. First, a test matrix is presented to illustrate the impact of various fin angles on building performance. The results of the different optimization runs incorporating the AFS are subsequently presented. Stochastic single-objective algorithms were implemented for separate optimization runs to minimize the acceleration or displacement response of the structure.

Chapter 10 summarizes the research that is presented in this dissertation. Recommendations for future work are proposed in regard to the low-rise parapet model and the aeroelastic tall building model. Additionally, improvement in efficiency to the CPS approach are proposed through the inclusion of machine learning.

Chapter 2: Literature Review

This chapter presents a review of the literature on the effects of wind on buildings and the structural design procedure, with a focus on low-rise buildings with parapets and tall buildings. A brief review of boundary layer wind tunnel (BLWT) testing procedures and model construction, with a focus on rigid models and aeroelastic models, is also included. Non-stochastic and stochastic optimization techniques are described in detail for both single-objective and multi-objective optimization problems.

2.1 Cyber-physical systems

CPSs link the real world with the cyber world, leveraging the capabilities of computers to monitor and control physical attributes (Al-Hammouri, 2012). Common components of CPSs include sensing, actuation, and communication systems for interfacing, computation for executing numerical models or algorithms, and a physical phenomenon of interest. The applications for CPS in civil engineering are diverse, including hybrid simulation (Shing & Mahin, 1984; Takanashi & Nakashima, 1987; Shing et al., 1996) online health monitoring and model updating (Song & Dyke, 2013), and decision-making frameworks (Lin et al., 2012). In civil engineering, experimental testing is essential to capture complex behavior for which numerical models are insufficient (e.g., strong nonlinearities, new devices and materials, and complex loads such as wind loads on bluff bodies). Physical models that capture these behaviors can be linked to numerical algorithms to create a versatile cyber-physical framework. Experimental testing has experienced a revolution through the use of

CPSs. Applications including the substructuring of physical systems and the substructuring of optimization algorithms are explored below.

In civil engineering, the first use of CPSs as an experimental method began in earthquake engineering with what is now known as hybrid simulation (Shing & Mahin, 1984; Hakuno et al., 1969; Takanashi & Nakashima, 1987). Hybrid simulation is a type of hardware-in-the-loop (HIL) test where the structural system is separated into numerical and experimental components that are linked together through a loop of action and reaction using actuators and sensors. In this way, the entire structural system is evaluated with a cost savings in the numerical components and enhanced realism in the experimental components. Hybrid simulation traditionally uses an extended time-scale for the experimental components, capturing the quasi-static nonlinear behavior of the specimen while modeling damping and inertia numerically. The development of rate-dependent structural control devices such as base isolation bearings and fluid dampers spurred interest in expanding hybrid simulation to run both experimental and numerical components in real time. The first modern real-time hybrid simulation (RTHS) was conducted by Nakashima et al. on a single degree of freedom system (1992).

Figure 1 shows an incomplete set of applications of CPS in civil engineering with a focus on experimental testing in earthquake and wind engineering. HIL testing has been developed for earthquake engineering in the form of hybrid simulation and RTHS. Similar HIL frameworks can be developed for wind engineering to study complex problems such as progressive failure and fluid-structure interaction, represented by the dashed boxes with X's under the *Hardware-in-the-Loop Testing* group in Figure 1.

Another opportunity for CPS in civil engineering is a substructuring of the optimization process, shown in the *Cyber-Physical Optimization Group* in Figure 1. Key to this framework is the numerical exploration of the design space coupled with the experimental creation and evaluation of a candidate design. Experimental evaluation can take the form of either traditional testing methods (e.g., BLWT) or HIL methods (e.g., RTHS). The former is explored in this paper using a mechatronic specimen to explore candidate designs subject to accurate wind loading created using a BLWT. This application is termed "loop-in-the-model" optimization (LIMO) because the model is iteratively adapting toward an optimal configuration. The name is complementary to "model-in-the-loop" or "hardware-in-the-loop" testing where instead of substructuring a physical system, a physical system's properties are iteratively adjusted through optimization. Additional possibilities for cyber-physical optimization are identified with dashed boxes and X's in Figure 1, for example, hardware-in-the-loop optimization, which combines HIL testing with LIMO.

There are many opportunities for developing new cyber-physical experimental techniques across civil engineering as identified in Figure 1. This study takes a new approach, namely the substructuring of the optimization process, to create a new family of experimental methods with rich possibilities for improving structural design.

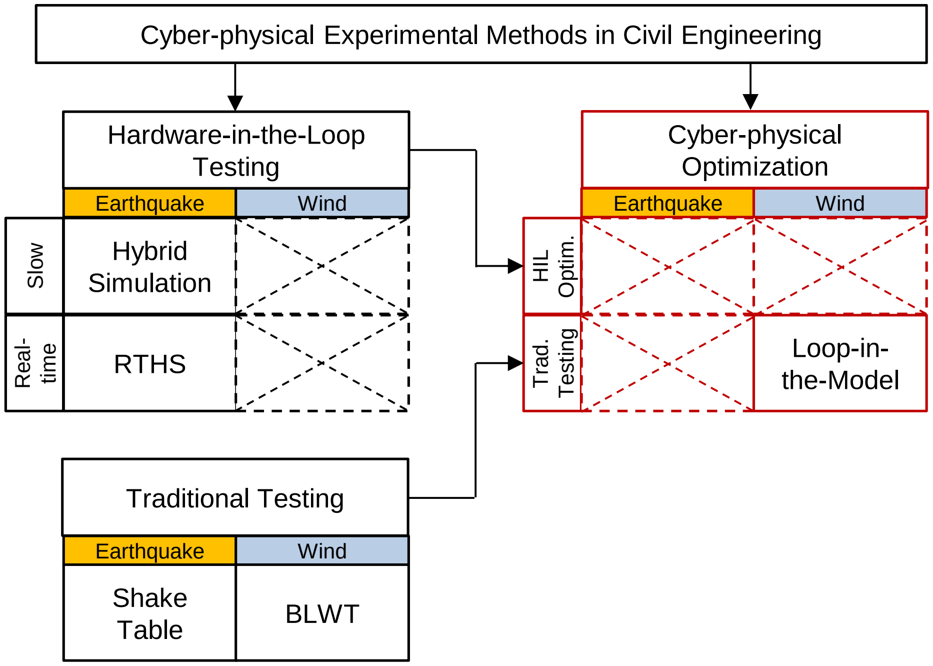

Figure 1. CPS experimental methods in earthquake and wind engineering.

2.2 Boundary layer wind tunnel testing

BLWTs are the primary tool used by wind engineers to characterize wind loading acting on civil structures. The continued reliance on experimental BLWT testing can be attributed to ongoing challenges with numerically modeling the flow structure around bluff bodies, such as buildings. These wind tunnels simulate the atmospheric boundary layer structure where the flow is conditioned through a series of mixing devices to generate target turbulence characteristics in the flow. Typical BLWTs consist of vortex generators and a long fetch of roughness elements for boundary layer development. Building models are placed downwind of the roughness element grid, as illustrated in Figure 2. The boundary layer flow at the test section is validated using analytical and empirical models of the mean velocity and turbulence intensity profiles (ESDU, 1974).

Figure 2. Boundary layer wind tunnel with model low-rise building, upwind view.

2.2.1 Boundary layer wind tunnel building models

Scaled building models are immersed in turbulent boundary layers simulated in the BLWT to accurately characterize wind-induced effects. The models are commonly instrumented with sensors to capture the pressure distribution or structural response. Typical model building scales range from 1:10 to 1:100 for low-rise buildings and 1:200 to 1:600 for tall buildings. These model scales are carefully selected depending on several factors including geometric scaling requirements of the incoming flow; such as the depth of the simulated boundary layer; and the BLWT cross section (blockage effects). Building models are constructed to be either rigid or aeroelastic depending on the subject of study.

2.2.1.1 Rigid models

Rigid models allow for the study of the effect of wind on the main wind force resisting system or components and cladding through the analysis of surface pressure measurements. Differential pressures from taps on the model building surfaces are measured simultaneously using a pressure scanner, such as Scanivalve ZOC33 (2016). For each test the non-dimensional pressure coefficient, C_p, can be calculated using the equation

$$C_p = \frac{(p - p_0)'_M}{\frac{1}{2}\rho U_{ref}^2 R_h^2} \tag{1}$$

where p is the wind pressure on the surface of the model measured by Scanivalve, p_0 is the static pressure at the reference height, and ρ is the air density. The reference height for all tests is taken to be the eave height of the building model. In order to estimate this value, a reference wind speed measurement, U_{ref} is obtained from pitot tubes above the boundary layer. This reference wind speed measurement is then converted to a mean wind speed at the eave height through a conversion factor, R_h. The sign of the pressure coefficient indicates the direction of the wind pressure on the surface of the model; a positive value indicates wind pressure acting towards the surface while a negative value indicates away from the surface. The C_p values could be normalized differently for comparison with ASCE 7-16 values; however, this was not necessary for the scope of the work herein.

The maximum and minimum pressure coefficients are often estimated for each wind attack angle using a Gumbel distribution (Cook & Mayne, 1980). The Gumbel distribution fitting method is a commonly used method for estimating peak pressures on low-rise buildings. The cumulative distribution function (CDF) for the Gumbel distribution is

$$F_g = \exp\{-\exp[-\alpha(C_p - u)]\} \tag{2}$$

where α (scale factor) and u (mode) are the shape parameters to determine based on the observed peaks. The measured record of C_p of model-scale length T is divided into n segments of equal length from which the peak (i.e., maximum and minimum) pressure coefficients from each segment are taken. The largest peak U_m ($m = 1, 2, \dots, n$) from each segment is extracted and then ordered in magnitude from smallest to largest. A probability of non-exceedance p_m is assigned for each peak according to $p_m = \frac{m}{N+1}$. The reduced variate y_m is calculated from $y_m = -\exp(-\exp p_m)$, U_m vs. y_m is plotted for $m = 1, 2, \dots, n$, and linear regression is used to estimate the Gumbel shape parameters α and u (Gavanski et al., 2016). Values of $n = 50$ and p = 78% are commonly used. In this case, a given probability of non-exceedance of p% estimates the maximum and minimum C_p values using the p^{th} percentile.

2.2.1.2 Aeroelastic models

The main objective of aeroelastic modeling is to obtain an accurate prediction of the structural response under a given wind loading. This is achieved when both the wind and the structure are properly modeled such that the model structure dynamically responds to the loading in a similar manner as the full-scale structure. Aeroelastic models are used to study fluid-structure interaction and capture the static and/or dynamic structural response, such as displacements or accelerations. Aeroelastic modeling removes the approximation of wind-induced effects by directly measuring the dynamic loads in the wind tunnel.

2.3 Optimization techniques

A cyber-physical optimization framework (e.g. LIMO) can be built around any optimization algorithm by replacing the evaluation of a numerical model with physical testing. Popular optimization algorithms are broadly categorized as deterministic or stochastic. Deterministic optimization algorithms involve no probability or uncertainty when determining the best solution for the objective, whereas stochastic methods introduce a use of randomness in an effort to escape local optima. Deterministic methods are further classified as to those which require convexity (gradient-based methods) and those which do not (e.g., pattern search methods or the simplex method). Stochastic methods are problem independent and better suited for solving multi-objective and constrained problems without the need for gradient information (Luke, 2013; Talbi, 2009). Gradient-based methods are faster than stochastic methods assuming that the function is not difficult to solve (i.e., smooth, low dimensionality, and/or separability), but stochastic algorithms broadly explore candidate solutions within a search space to avoid premature or local convergence, which can lead to non-intuitive solutions for complex optimization problems. Therefore, there is no guarantee that a global optimal solution, or even bounded solution, will be found using stochastic methods (Perez & Behdinan, 2007). Additionally, due to the inherent randomness of stochastic methods there is no guarantee that repeating an optimization process will result in an identical optimal result. Alternatively, because there is no probability or uncertainty assumed for deterministic methods the optimal solution to a problem is expected to be repeatable.

2.3.1 Non-stochastic optimization

2.3.1.1 Golden-section search

Based on a preliminary test matrix exploring the effects of parapet height and wind angle on roof pressures, the optimal parapet height for minimizing the magnitude of peak suction pressure on the roof and parapet surfaces (i.e., the inner parapet walls and top of the parapet) considering all approach angles is anticipated to occur at one unique height (i.e., a unimodal problem). Golden section search (GSS) is a non-stochastic, deterministic optimization technique for finding the extremum of a strictly unimodal function by successively narrowing the search space within which the extremum is known to exist. The GSS algorithm is similar to the bisection method because it iteratively reduces the search space, and it derives its name from the fact that the length of the search space is linearly reduced each iteration by the golden ratio (Luenberger & Ye, 1984). The GSS is explored herein for its simplicity and quick convergence.

Assume that a function f is unimodal on the interval $[a, b]$. The search space is divided into three sections $[a, x_1]$, $[x_1, x_2]$, and $[x_2, b]$ by adding two intermediate points, x_1 and x_2 as shown in Figure 3.

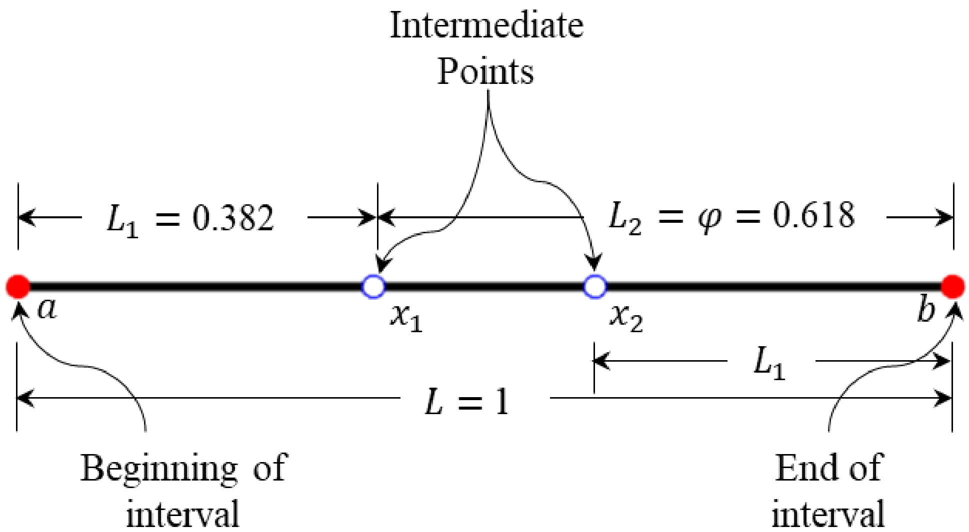

Figure 3. Sections of golden section search for a unit interval.

The function is then evaluated at the two intermediate points and the results $f(x_1)$ and $f(x_2)$ are compared. The subinterval of either $[a, x_1]$ or $[x_2, b]$ can then be discarded such that the minimum (for minimization) is bracketed within the remaining subinterval (Nazareth & Tseng, 2002). The locations of x_1 and x_2 are chosen so that two conditions are satisfied: x_1 and x_2 are equidistant from a and b respectively, and the ratio of lengths of the three intervals, $L/L_2 = L_2/L_1$, is constant. Based on these two conditions, $L_2 = \varphi \cong 0.618$, and $L_1 = 1 - \varphi \cong 0.382$. As a result, only one new function evaluation is needed every successive iteration for the standard GSS algorithm as one of the previous intermediate points is reused. The two intermediate points are calculated according to the following,

$$x_1 = a + (b - a)(1 - \varphi) \tag{3}$$
$$x_2 = a + (b - a)\varphi \tag{4}$$

BLWT testing is subject to uncertainty; peak pressures tend to vary from experiment to experiment for the same specimen configuration (e.g., same parapet height and wind angle). To some degree, this uncertainty is mitigated by estimating peak pressures from the data (e.g., using extreme value analysis) rather than directly using instantaneous peak pressures (i.e., simple worst peak method). This paper uses a Fisher-Tippet Type I (Gumbel) extreme value distribution to estimate peak pressures. Despite the application of the Gumbel distribution, variability in the estimate of peak pressures remain (Gavanski et al., 2016). Peaks may be linked to a specimen configuration that is not truly representative of that configuration due to the chaotic nature of wind and the experimental error from the Scanivalve pressure scanner. To avoid sensitivity to a non-representative test (i.e., an outlier), the standard GSS algorithm is modified such that the previous intermediate point that is reused will be retested rather than directly using test results from the previous iteration.

With each iteration, the search space is reduced around the extremum until a pre-defined tolerance for the remaining search space size is met. The tolerance is defined as the precision at the final iteration of the calculated extremum. Based on the linear reduction of the search space by φ for each iteration, the number of required design iterations N for a given tolerance Tol can be predetermined according to the following,

$$(b-a) * \varphi^N = Tol \tag{5}$$

$$N = \frac{\ln\left(\frac{Tol}{b-a}\right)}{\ln(\varphi)} \tag{6}$$

2.3.2 Stochastic optimization

2.3.2.1 Particle swarm optimization

Particle swarm optimization (PSO) is a population-based stochastic optimization technique. Particle swarm optimization mimics the social behavior where a population of individuals adapts to its environments by discovering and jointly exploring promising regions. This swarm intelligence method is based on the simulation of social interactions of members of a species, such as the movement of flocks of birds, schools of fish, and swarm of bees. Particle swarm optimization was inspired by evolutionary programming, genetic algorithms, and evolution strategies and shares similarities with genetic algorithms and evolutionary algorithms.

Particle swarm optimization is a non-gradient-based, meta-heuristic optimization method (Talbi, 2009). Non-gradient-based optimization techniques are especially useful in solving problems in structural engineering due to their versatility in handling multiple design variables. Particle swarm optimization efficiently explores a large number of candidate solutions over a large search space without prematurely converging, which can lead to non-intuitive solutions. The technique is simple to program because it is an inherently iterative process reliant on only a few formulas to govern the iterations. Complexities only arise in the analysis of candidate solutions (e.g., in wind engineering) and calculation of the objective function. Also, the problem definition does not require continuity and is capable of handling nonlinear, nonconvex design spaces. In comparison to genetic algorithms, there is no mutation calculation; only the best-performing particle transmits information to the others. As a meta-heuristic method, there is no guarantee that a global optimal solution, or even bounded solution will be found (Perez & Behdinan, 2007). Because the solution is not necessarily optimal, the solution from a PSO algorithm is more precisely termed a sub-optimal solution. Additionally, probabilistic search algorithms tend to require more function evaluations than gradient-based methods to reach an acceptable optimum solution. The technique is also very slow to working out local optimal solutions and may gravitate towards a particle's personal best solution. The technique overall is relatively new so limited studies have been performed related to structural engineering; however, research is actively being conducted to improve the optimization framework with specific structural engineering considerations.

In the context of structural engineering, the swarm represents a group of candidate design solutions. Each particle within the swarm is a candidate design which consists of an *N*-dimensional finite position and velocity. The position refers to the values of *N* design parameters (e.g., cross-sectional areas of the members) while the velocity refers to the changes in the design parameters from one iteration to the next. The position of the particles is often initially randomly distributed throughout the design space. These candidate solutions then iteratively move throughout the search space seeking better positions with the expectation that the swarm of particles will move toward the best solutions. This process is repeated either for a predetermined number of design iterations, or until convergence is reached. An outline of a basic PSO algorithm is given in Figure 4.

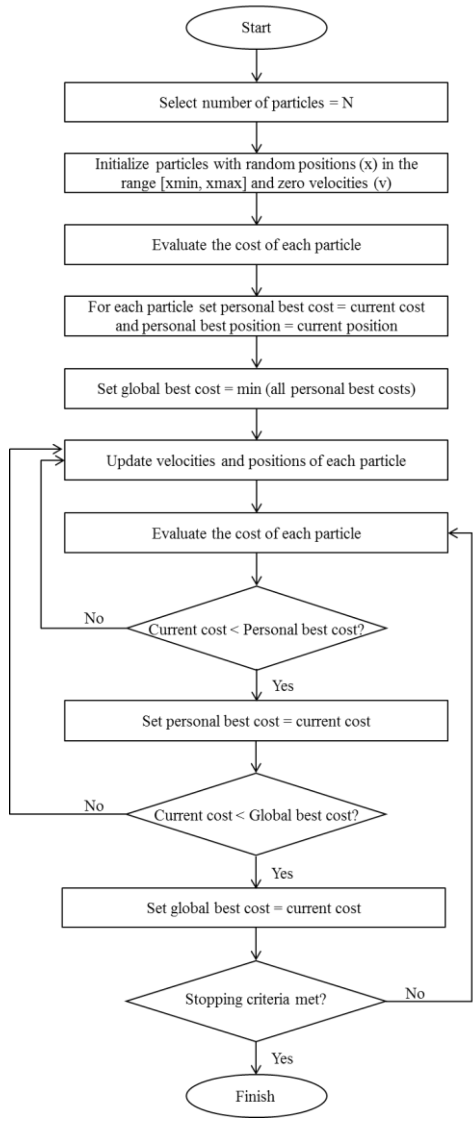

Figure 4. Outline of a basic particle swarm optimization algorithm.

The process for updating the position of each particle is

$$x_{j+1}^{i} = x_{j}^{i} + v_{j+1}^{i}\Delta t \tag{7}$$

where x_{j+1}^{i} is the position of particle i at iteration $j+1$, v_{j+1}^{i} is the corresponding velocity vector of the particle, and Δt is the time step value.

The procedure for determining the velocity vector of each particle in the swarm depends on the particular PSO algorithm. The process which is commonly used for updating the velocity vector was first introduced by Shi and Eberhart (1998a) as

$$v_{j+1}^{i} = wv_{j}^{i} + c_1 r_1 \frac{\left(p_j^i - x_j^i\right)}{\Delta t} + c_2 r_2 \frac{\left(p_j^g - x_j^i\right)}{\Delta t} \tag{8}$$

where r_1 and r_2 are independent random numbers in the range [0,1], p_j^i is the best known position of particle i considering iterations 1 through j, p_j^g is the best known position of all particles considering iterations 1 through j, and Δt is the time step value. Throughout the present work a unit time step of one iteration is used. An alternative method for determining p_j^g is to use the best position of all particles only considering the current iteration (Fourie & Groenwold, 2002). In Equation (8), there are three problem-dependent parameters that influence every particle's velocity: the inertia of the particle, w and two trust parameters, c_1 and c_2. The inertia controls the algorithm's exploration properties; a larger inertia enables a more global search of the design space because particles are more inclined to continue on their previous trajectory. The trust parameters indicate how much confidence the current particle has in itself, c_1 and in the swarm, c_2 and will draw the particle to these respective best positions. When PSO was originally introduced, Kennedy and Eberhart (1995) proposed that c_1 = c_2 = 2 in order to give the products of $c_1 r_1$ and $c_2 r_2$ each a mean of 1. Shi and Eberhart (1998b) analyzed the difference in performance and accuracy for both fixed and time-decreasing inertia weights. Based on empirical studies, an inertia weight of $w = 0.8$ was the only fixed inertia weight to never fail in finding an acceptable solution regardless of velocity limits. A time-decreasing inertia weight from 1.4 to 0 was found to be better than a fixed inertia weight; the larger initial inertia weight enables a broad global search while the smaller final inertia weight forces more local searches (Shi & Eberhart, 1998b). Shi and Eberhart conclude that it is best to use a fixed inertia weight of w = 0.8 or w = 1.0 dependent upon the selection of the values of the velocity limits, and that a time varying inertia weight would result in an even better performance. Ultimately, the selection of inertia and trust weights are problem dependent and their values must be determined case-by-case. A poor selection of parameters may lead to premature convergence to a solution that is not globally optimal, or at the other extreme, a solution that takes an excessive number of iterations to converge. Parameter selection can be done through trial-and-error or through deduction and personal judgment.

To increase the performance and accuracy of PSO, multiple enhancements to the standard algorithm have been proposed and tested. The first of these enhancements is the inclusion of convergence criterion within the problem statement. The purpose of proper convergence criterion is to ensure that the optimization process avoids unnecessary calculations once an optimum solution is reached. Preferably the convergence criterion should be general (i.e., not include parameters that are specific to the problem). One common practice is to assume that convergence is obtained if the change in the objective function is below a particular threshold for a specified number of iterations (Venter & Sobieszczanski-Sobieski, 2003). Basic PSO is for unconstrained problems only, and original literature for basic PSO does not address particles which violate design constraints. Thus, constrained optimization has been introduced which usually addresses this problem through the use of different methods including penalty functions, a fly-back mechanism, or resetting the particle velocity to zero.

A penalty function penalizes the objective function when one or more constraints are violated. If penalty coefficients are used, but appropriate coefficients cannot be provided, then difficulties will be encountered. Additionally, penalty functions reduce the overall efficiency of the PSO; it resets infeasible particles to their previous best positions, sometimes preventing the search from reaching global max.

Another method for addressing particles which violate design constraints involves the use of a "fly-back mechanism" which is able to accelerate the convergence rate and improve the accuracy effectively in comparison with previous improvements (He et al., 2004) and basic PSO, respectively. With the use of a fly-back mechanism, if it is determined that a particle would violate the position constraints of the design space, then the direction of the particle's velocity is reversed and the position is recalculated for the particle so that it will reach its original position. The global minima of design problems have been found to usually be close to the boundaries of the feasible search space. By enforcing a particle to return to its original position and assuming that the global best particle remains in the same position, then the direction of the velocity in the next iteration will still point to the boundary but will point closer to the global best particle (He et al., 2004).

Another method involves resetting particle i's velocity to zero if it violates one or more constraints at iteration j. The velocity vector for particle i at iteration $j + 1$ would then be given as

$$v_{j+1}^{i} = c_1 r_1 \frac{\left(p_j^i - x_j^i\right)}{\Delta t} + c_2 r_2 \frac{\left(p_j^g - x_j^i\right)}{\Delta t} \tag{9}$$

Therefore, the velocity of particle i at iteration $j+1$ would only be influenced by the best-known position of particle i considering iterations 1 through j, and the best-known position of all particles considering iterations 1 through j. This would remove all influence of the particle's current trajectory and would likely cause the particle to return to the feasible design space in the next iterations (Mans et al., 2005).

2.3.2.2 Big bang-big crunch

The Big Bang-Big Crunch method originally developed by Erol and Eksin (2006) is a population-based heuristic algorithm. The Big Bang-Big Crunch method is based primarily on a theory of the universe's evolution. The optimization method consists of two main phases: the Big Bang phase and the Big Crunch phase. In the Big Bang phase, candidate solutions are randomly distributed throughout the design domain. The random nature of Big Bang can be attributed to the dissipation of energy in nature, while convergence to a local or global optimal point represents a gravitational attraction (Erol & Eksin, 2006). The Big Bang phase is followed by the Big Crunch phase. In the Big Crunch phase, a convergence operator uses the current candidate positions and their corresponding fitness function values, φ_i to compute a "center of mass" ($\boldsymbol{X}_c^{k,j}$), which can be calculated according to Equation (10):

$$\boldsymbol{X}_c^{k,j} = \frac{\sum_{i=1}^{N}\left(\frac{1}{\varphi_i}\right)\boldsymbol{X}_i^{k,j}}{\sum_{i=1}^{N}\left(\frac{1}{\varphi_i}\right)} \; j = 1, \dots, nd \tag{10}$$

where $\boldsymbol{X}_i^{k,j}$ is the *j*th component of the *i*th solution generated in the *k*th iteration, *N* is the population size during the Big Bang phase, and *nd* is the number of components. The candidate solutions for the current iteration are then discarded, and the positions of new candidate solutions for the next iteration are normally distributed around the center of mass as follows

$$\boldsymbol{X}_i^{k+1} = \boldsymbol{X}_c^k + \alpha \boldsymbol{r}_i \left(\frac{\boldsymbol{X_{max}} - \boldsymbol{X_{min}}}{k+1}\right) \; i = 1, \ldots, N \tag{11}$$

where $\boldsymbol{r}_i$ is a random number from a standard normal distribution, α is a parameter for controlling the size of the search space, and $\boldsymbol{X_{max}}$ and $\boldsymbol{X_{min}}$ are the position vectors of the upper and lower bounds of each design variable, respectively.

2.3.3 Multi-objective optimization

Multi-objective optimization is necessary when two or more objectives are in conflict and a compromise between objectives is desired. This conflict is often the case when considering the requirements of multiple stakeholders in engineering design. If there is no single solution that will simultaneously optimize each objective, there instead exists an infinite number of Pareto optimal solutions. A solution is a Pareto optimal solution if any of the objective functions cannot be improved without degrading one or more of the other objective functions. The set of solutions that are Pareto optimal is said to make up the Pareto front. Obtaining the Pareto front allows the user to make a focused tradeoff between potential solutions to obtain the desired solution. To determine an optimal solution from the set of Pareto optimal solutions, subjective preference from a user is required; all Pareto optimal solutions are considered equally acceptable until the user preference is applied.

Multi-objective optimization can be divided into four classes based on the user's preference: no-preference, a priori, a posteriori, and interactive (Hwang & Masud, 1979). In no-preference methods, the user does not indicate their preference (often defaulting to equal weight (Luque et al., 2009)), while a priori, a posteriori, and interactive methods utilize preference information before, after, and iteratively while searching for a solution, respectively (Miettinen, 1999).

2.4 Low-rise buildings with parapets

2.4.1 Effect of wind on low-rise buildings with parapets

Architectural detailing significantly impacts the magnitude, direction, and correlation of distribution pressures over a roof surface. The worst mean and peak suctions on flat, low-rise building roofs occur near the upwind corner and edges (Pindado & Meseguer, 2003) for cornering or oblique incident wind angles (Kind, 1988). These large suctions along the roof edges are the result of strong conical vortices known as delta wing vortices due to their similarity to the vortices produced at the leading edge of aircraft with delta wings. Parapet walls reduce these extreme suction loads, preventing roof gravel and other loose material from becoming wind-borne debris capable of damaging the building envelope and leading to wind and rain intrusion. Solid, perimetric parapets taller than one meter reduce both the mean and peak pressure coefficients, most notably in the corner regions (Stathopoulos & Baskaran, 1987). Research regarding parapets has primarily focused on characterizing the local pressure distributions on the roof surface, specifically for components and cladding. Some studies have determined that the use of parapets with non-uniform or modified geometries reduces the extreme suction loads caused by the corner vortices (Kopp et al., 2005a). Other studies have considered the underlying structural members (Kopp et al., 2005b) and parapet itself (Stathopoulos et al., 2002) under wind loading. Recent studies have determined that it is essential to have a high density of pressure taps in the upwind corner region to ensure that the peak suction pressures are captured (Kopp et al., 2005a; Kopp et al., 2005b; Kind, 1988).

Building codes (e.g., ASCE 7-16) often allow for a pressure reduction over different roof regions in the presence of parapets; however, there has not been extensive research regarding accurate regions of reduction based upon the geometry of the building and parapet (ASCE 7-16). Additionally, research has primarily focused on the corner zones of roofs with limited research on the edge and interior zones focused on mitigating local loading through the use of alternative geometries. There has not been much research on the effect of different parapet heights or on the optimal height of solid, perimetric parapets for a given low-rise building (Kopp et al., 2005c).

2.4.2 Design implications of parapets on low-rise buildings

The windward roof edges on low-rise structures cause a separation of the boundary layer and generate vortex flow with large suction loading that is particularly severe for oblique approaching wind angles. Increasing the parapet height has a significant effect on these wind suction loads because it alters the location of the roof corner vortex, which mitigates extreme corner and edge suction loads, a components and cladding design load (Kopp et al., 2005c; Mans et al., 2005). At the same time, the presence of parapet walls increases the surface area of the building, leading to an increase in demand on the main wind force resisting system.

2.5 Tall buildings

2.5.1 Effect of wind on tall buildings

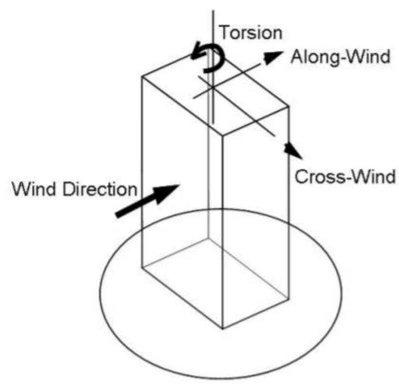

Figure 5. Wind response directions (Mendis et al., 2007).

Tall, slender structures are often more susceptible to dynamic motion perpendicular to the direction of the wind than parallel, defined in Figure 5 as cross-wind and along-wind, respectively. This form of oscillation can be very significant if the structural damping is small. The cross-wind excitation of modern tall buildings is predominantly controlled by vortex-induced vibrations (Mendis et al., 2007). Tall buildings are bluff (as opposed to streamlined) bodies which cause the flow to separate from the surface of the structure, known as vortex shedding. Vortex shedding induces fluctuating surface pressures which can cause oscillations if the body is flexible. These shed vortices oscillate at a frequency defined by the Strouhal number of the structure. The equation for the Strouhal number, St, of a structure is given as

$$\mathrm{St} = \frac{fL}{U} \tag{12}$$

where f is the frequency of vortex shedding, L is the characteristic length, and U is the flow velocity. Thus, the structure is subjected to periodic cross pressure loading resulting in an alternating crosswind force as these vortices shed. If the structure's natural frequency and the shedding frequency of the vortices coincide, large and damaging displacements can occur in a phenomenon known as "lock-in".

2.5.2 Design implications of tall buildings

Serviceability failures are more prevalent in tall buildings than low-rise buildings due to larger top-story deflections and vibration-induced accelerations. In contrast to strength limit states, serviceability limit states are usually non-catastrophic and involve the perceptions of the user. Exceeding a serviceability limit state in a building means that its function is disrupted because of local minor damage, deterioration, or occupant discomfort. Table 1 presents some guidelines on general human perception levels of different acceleration levels (Mendis et al., 2007).

Table 1. Human perception levels.

Level	Acceleration (ms^{-2})	Effect
1	< 0.05	Humans cannot perceive motion
2	0.05 – 0.10	a) Sensitive people can perceive motion b) Hanging objects may move slightly
3	0.10 – 0.25	a) Majority of people will perceive motion b) Level of motion may affect desk work c) Long-term exposure may produce motion sickness
4	0.25 – 0.40	a) Desk work becomes difficult or almost impossible b) Ambulation still possible
5	0.40 – 0.50	a) People strongly perceive motion b) Difficult to walk naturally

		c) Standing people may lose balance
6	0.50 – 0.60	Most people cannot tolerate motion and are unable to walk naturally
7	0.60– 0.70	People cannot walk or tolerate motion
8	> 0.85	Objects begin to fall and people may be injured

An alternative proposal for acceleration thresholds by Chang (1973) for the acceleration “a” using a theoretical extrapolation of aerospace industry data (considering that 1 milli-g is equivalent to 1/1000 of the gravity acceleration) are

1) Non-perceptible: a < ~0.05 ms^{-2}
2) Perceptible: ~0.05 ms^{-2} < a < ~ 0.10 ms^{-2} - ~ 0.15 ms^{-2}
3) Annoying: ~ 0.10 ms^{-2} - ~ 0.15 ms^{-2} < a < ~ 0.50 ms^{-2}
4) Very Annoying: ~ 0.50 ms^{-2} < a < ~ 1.50 ms^{-2}
5) Unbearable: a > ~ 1.50 ms^{-2}

Based on interviews with building occupants, Hansen et al. (1973) suggested that: “The return periods, for storms causing an RMS[root-mean-square] horizontal acceleration at the building top that exceeds 0.5% [of the standard acceleration due to gravity], shall not be less than 6 years. The RMS shall represent an average over the 20-min period of the highest storm intensity and be spatially averaged over the building floor.”

The structural design of most modern tall and slender buildings is predominantly governed by wind-induced serviceability design criteria related to the comfort of occupants and lateral building drift (i.e., sway) requirements. Infrequent wind events of long return periods (e.g., 50-years) are commonly assumed for evaluating lateral drift criteria and strength limit states for safety requirements (Huang et al., 2012). Yet, wind sensitive tall buildings designed to meet drift and strength requirements may still experience excessive low-frequency (< 1 Hz; ISO 6897, 1984) motion that can adversely affect the comfort of occupants during more frequent wind events (e.g., less than 10-years). Therefore, designers must provide adequate lateral stiffness (or damping) to control wind-induced motion that may cause discomfort to the occupants and jeopardize the functionality of the building.

Studies have shown that the perception of wind-induced motion can be linked to the horizontal acceleration of the building (e.g., Kwok et al., 2009; Bernardini et al., 2014). Peak and RMS floor accelerations are typically considered to represent building motion (Boggs, 1997), although some researchers have argued that the rate of change of acceleration (i.e., jerk) may be a superior indicator of human perception of motion (e.g., McNamara et al., 2002). Experiments in the field and in motion simulators (Chen & Robertson, 1972; Irwin, 1981; Denoon & Kwok, 2011) have been conducted to investigate the effect of other factors that may impact motion perception, including building motion frequency, amplitude, event duration, and waveform (Kijewski-Correa & Pirnia, 2009). As a result of these studies, prescriptive provisions have been developed and are included in some building codes and standards to address serviceability requirements related to controlling wind-induced motion for the comfort of occupants (e.g., ISO 1984, 2007; NRCC, 2010). Particularly, the horizontal acceleration criteria in ISO 6897 (1984) is based on the root-mean square acceleration for the worst 10 consecutive minutes in a 5-year return period for structures in the frequency range of 0.063 to 1 Hz. Melbourne and Palmer (1992) later generalized the acceleration criteria in ISO 6897 to accommodate for other return periods

$$a_{L,RMS} = \left(0.68 + \frac{\ln(\mathrm{MRI})}{5}\right)\exp(-3.65 - 0.41n) \tag{13}$$

where $a_{L,RMS}$ is the RMS horizontal acceleration threshold, MRI is the mean recurrence interval (i.e., return period) in years, and n is the frequency of the building in hertz. As described in Melbourne and Palmer (1992), peak acceleration criterion $\hat{a}_L$ can be obtained from Equation (13) by introducing a peak factor value g; $\hat{a}_L = g a_{L,RMS}$. If the acceleration is related to a normally distributed process, then $g = \sqrt{2\ln(nT)}$ where T is the event duration in seconds.

Serviceability limit states that address excessive building deflections (i.e., sway) are also of concern to designers for ensuring the integrity of non-structural elements (e.g., components and cladding) under wind-induced deformations (Simiu, 2011). Serviceability design criteria for lateral building deflection (i.e., sway) is commonly verified by linear-elastic static analysis using unfactored equivalent static wind loads (ESWLs), which are usually based on wind events of 50-year or 100-year MRI (Griffis, 1993). The ESWLs can be calculated from wind code provisions (ASCE 7-16) or derived from wind tunnel tests (e.g., Huang & Chen, 2007). After determining the ESWLs and applying them to the structural system, the overall (i.e., total) and inter-story displacements can be obtained from static analysis and compared against drift limit states.

Overall building drift limits for most tall buildings are defined as the lateral deflection of the top-most occupied floor divided by the height from grade to the top story of the building, while inter-story drift is defined as the relative horizontal displacements between consecutive stories divided by the height of the floor (Griffis, 1993). Common drift limit ratios range from 1/100 to 1/600 of the building height for overall drift (i.e., sway) and 1/400 to 1/500 of the story height for inter-story drift.

2.5.3 Reducing response of tall buildings through aerodynamic modifications

2.5.3.1 Aerodynamic mitigation techniques

One approach for reducing the dynamic response of buildings is to use aerodynamic mitigation techniques. These methods use simple, innovative architectural features to modify the aerodynamic shape of buildings to reduce the wind loads. Aerodynamic mitigation techniques which modify the external shape of a building (e.g., corner modifications or the twisting of the cross section shape along the height of the building) can significantly alter the wind-structure interaction and reduce the building response, leading to a more economic and user-friendly design in terms of comfort (Irwin, 2008; Kareem et al., 1999). Aerodynamic mitigation techniques assist by disrupting the formation of strong corner vortices, breaking the coherent formation of vortices, and diverting flows in the separation zone over the roof edge or away from weak members. Broadly speaking these can be categorized as minor or major modifications dependent on their effect on the building design.

Minor modifications are considered those which have an insignificant effect on the structural and architectural design of the building. Common building shapes are rectangular in plan and as a result experience strong vortex-induced forces. Applying minor modifications can reduce both the along-wind and across-wind responses from these excitation forces compared to basic corners. Examples of minor aerodynamic corner modifications are highlighted in Figure 6. Existing research on the impact of corner modifications on the aerodynamic forces on tall buildings has focused on variations of chamfered, slotted, rounded, and recessed corners (Mooneghi & Kargarmoakhar, 2016). The effectiveness of corner modifications has been found to be dependent on the approach angle of oncoming wind (Tse et al., 2009). There has been some existing work analyzing the effectiveness of the aerodynamic modifications of vertical fins and slotted fins in reducing the along-wind and across-wind response of tall, square buildings (Kwok & Bailey, 1987). This work focused on fins and slotted fins fixed fin configurations as shown in Figure 6. This current work expands on the previous work by exploring fin configurations at different angles with different symmetries enforced.

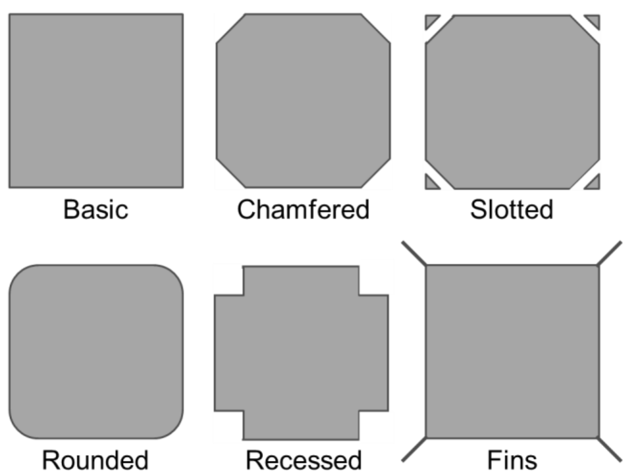

Figure 6. Minor aerodynamic corner modifications (based on Mooneghi & Kargarmoakhar, 2016).

Major modifications are those which have significant effects on the structural and architectural design of the building. Examples are highlighted in Figure 7.

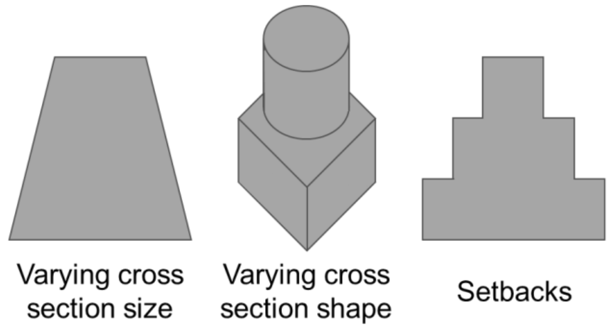

Figure 7. Major aerodynamic structural modifications.

Applying major modifications (e.g., varying cross section size, varying cross section shape, twisting, and setbacks) can alter the wind flow behavior around the building and significantly reduce the wind-induced building response, resulting in a more economic and comfortable design. These modifications vary the Strouhal number with height, and thus the vortices shed over a broad range of frequencies. Varying the cross section size or shape significantly reduce vortex-induced vibrations by avoiding simultaneous vortex shedding along the building height.

2.5.3.2 Aerodynamic shape optimization

Another approach to reduce the dynamic response of buildings is through aerodynamic shape optimization techniques. In an optimal shape design problem, a performance criterion is established and the optimization is dependent on the shape of a boundary. An experienced designer utilizes creativity and insight to form a well-posed optimization problem. Objective functions must be defined based on the goals of the optimization, design variables which affect the aerodynamic shape, and constraints that define a feasible region of the design space. The optimization algorithm finds the values of the geometric parameters which optimize the objective function while satisfying the constraints. Aerodynamic shape optimization allows the designer to explore more alternative aerodynamic shapes than traditional methods, which are limited to a certain number of geometries pre-selected by the designer.

Traditional shape optimization is performed using a combination of experimental and numerical methods using wind tunnel tests or computational fluid dynamics, respectively. Experimental methods accurately characterize the effect of modifying the building shape on the overall wind-induced excitations. Modifying the building shape (e.g., corner tailoring or other aerodynamic modifications) often reduces forces due to drag and vortex shedding, but can also produce a more complicated aerodynamic behavior that is challenging to model numerically (Carassale et al., 2014). These methods typically investigate a discrete number of different configurations to determine the configuration with the optimal aerodynamic performance. Previous experimental work within shape optimization (Merrick & Bitsuamlak, 2009) has examined high-rise buildings with different simple cross-section shapes to determine the relationship between shape and wind loading patterns for tall buildings. Traditional aerodynamic shape optimization using experimental methods is demanding due to being time- and cost-intensive for performing tests on a limited number of possible configurations.

Numerical simulation methods allow for the consideration of many alternative designs, and if coupled with traditional experimental methods can reduce the required number of wind tunnel tests for the examined optimization problem. CFD is currently primarily used for estimating the aerodynamic performance of a given configuration but it does not guarantee the identification of the optimal design. To ensure the optimal design is discovered, CFD can be coupled with appropriate numerical optimization methods for aerodynamic shape optimization problems. The design which satisfies all constraints and optimizes overall performance using numerical optimization methods can then be tested experimentally to better understand wind-structure interaction. Aerodynamic shape optimization using CFD has been used in both the aerospace and automotive industry for years (Kim et al., 2009; Muyl et al., 2004, respectively), and recently been of increasing interest for the application to the aerodynamic design of the shape of tall buildings.

2.6 Summary

This chapter presented an overview of the effects of wind on buildings and the structural design procedure focusing on low-rise buildings with parapets and tall buildings. A review of current BLWT testing procedure and model construction was presented with a focus on rigid and aeroelastic models. Different optimization techniques (e.g., non-stochastic, stochastic, single-objective, and multi-objective) are presented. The determination of the most suitable optimization technique and algorithm-specific parameters are both problem-dependent. Room for improvement in the area of CPS within wind engineering remains, and the optimization of wind-sensitive structures stands to benefit from the combination of efficient numerical optimization algorithms and accurate BLWT testing.

Chapter 3: Rigid Model Development and CPS Setup

This chapter presents the details of the model low-rise building with a structural parapet, including the scale, dimensions, and materials used for fabrication. Rigid models are a fundamental type of structure for modeling and evaluation through boundary layer wind tunnel (BLWT) testing that offer a simple testing approach sufficient for structures with little aerodynamic response, such as low-rise buildings. The low-rise model created for this study is assumed rigid.

The selection of a physically adjustable design variable and creation of a suitable actuation system for the model building is subsequently presented. The framework for providing data and power for controlling the actuation system is described to thoroughly depict the physical component of the CPS incorporating the rigid model. All experimental equipment used for the BLWT testing with the rigid, low-rise parapet model, the method for processing and analyzing the measured pressure data using the non-dimensional pressure coefficient C_p, and the method for calculating base shear forces are also presented.

3.1 Rigid specimen

The low-rise building was modeled after a two-story office building. A length-to-width ratio of 1.5 was selected to create a rectangular building shape. Model-scale dimensions were selected as 29.25 inches × 19.50 inches in plan with a height of 20 inches. By actuating the outer wall, a parapet wall of up to 4.50 inches model-scale was created. Based on the model dimensions and target design of a two-story office building, a 1:18 model-scale was selected. This corresponds to a building with full-scale dimensions of 29.6 feet × 44.4 feet in plan and 30 feet tall.

Clear, impact-resistant polycarbonate was selected for all building surfaces because it was expected to remain rigid against the anticipated pressures in the BLWT and is easier to machine than other clear plastics. The nominal thickness of the polycarbonate sheets for the parapet walls was selected to be 0.1875 inches to avoid an excessively thick parapet wall, while still providing sufficient rigidity to prevent flexure of the walls. To further increase the rigidity of the parapet structure, 0.625 inch thick polycarbonate blocks were used to connect the outer and inner parapet walls panels with screws. The outer wall (vertically movable) consisting of the outer building walls, inner parapet walls, and top of the parapet and the roof of the inner core of the model (stationary) were the only surfaces exposed to airflow. The nominal thickness of the polycarbonate sheets used to manufacture the inner model was selected to be 0.25 inches.

To capture the envelope wind pressure, 0.054 inch inner diameter urethane tubing was used with 0.063 inch outer diameter bulged stainless steel tubes; the urethane tubing was stretched to securely fit around the bulged stainless steel tubing. The stainless steel tubing was then inserted into 0.0625 inch diameter holes that were drilled into the sheets of polycarbonate.

Urethane tubing and pressure taps were installed on the outer and inner sides of the parapet wall. A total thickness of the model parapet wall (i.e., the outer wall) was selected to be 1 inch, as a thickness of at least 1 inch was required to accommodate the thickness of polycarbonate sheets, metal tubulation, and minimum bend radius for the urethane tubing. The pressure taps on the outer and inner parapet walls were staggered to permit a thinner model parapet wall.

A model-scale 1-inch thick parapet and a 1:18 model-scale correspond to a 1.5 foot (18 inches) thick full-scale parapet. According to the Building Code Requirements for Masonry Structures, parapet walls should have a thickness of at least 8 inches (full-scale) (ACI/ASCE/TMS, 2011). Therefore, the building model represents a realistic two-story full-scale building with a protective parapet.

3.2 Model actuation

The design parameter selected is the parapet wall height of a low-rise building. The outer wall of the model was actuated by four stepper motors, one at each corner of the model. The inner model remained stationary, maintaining a constant building height. As the outer wall rose above the inner model, a parapet wall was created. Strips made from polytetrafluoroethylene were used between the inner model and outer wall to assist in achieving vertical actuation with minimal friction. A foam gasket was used between the outer wall and the turntable to allow the outer wall to move while preventing air from leaking around the base of the model. The model is shown in Figure 8, including the inner model (stationary) and outer wall (vertically movable).

Nanotec stepper motors (LS4118S14004-T6x1-150) with a captured lead screw raised and lowered the outer wall around the inner model to change the eave height. The stepper motors were connected to the outer wall using polycarbonate triangular supports installed in the bottom corners. A PVC pipe installed around the drive shaft of the stepper motor protected the shaft from coming into contact with any urethane pressure tap tubing during actuation. The stepper motor and its installation are shown in Figure 9.

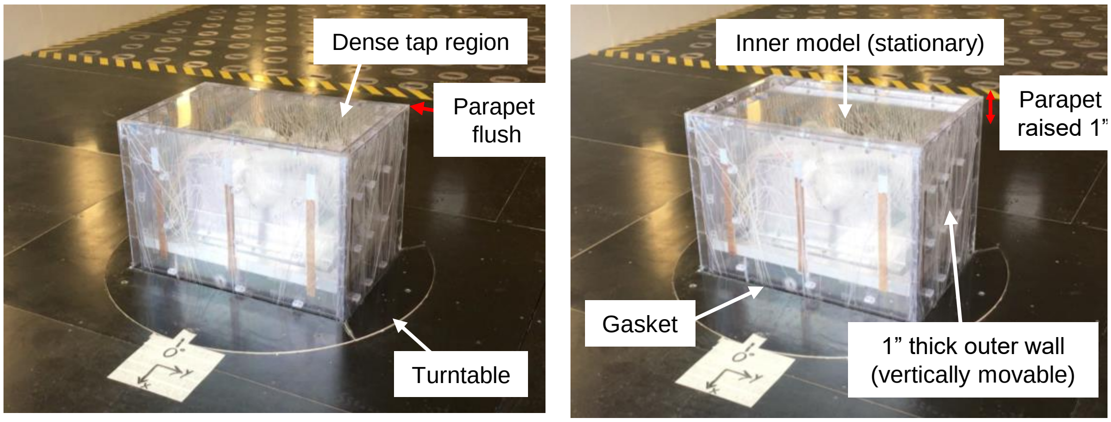

(a) (b)

Figure 8. (a) Rigid, low-rise building model with a 0-inch parapet wall and (b) a 1-inch parapet wall (dimensions are in model-scale).

(a) (b)

Figure 9. (a) Stepper motor and (b) stepper motor installed in corner of parapet wall with PVC shield.

<u>3.3 Stepper motor control</u>

The setup for controlling the stepper motors is given in Figure 10. Data (i.e., commands from the coordinating computer on the University of Florida network) and power passed through a slip ring on the BLWT turntable. A Raspberry Pi 3 was mounted within the turntable to take commands from the coordinating computer and send them to each of the four stepper motor controllers, which in turn actuated the stepper motors. Encoders on the stepper motors provided feedback to ensure the desired displacement was reached.

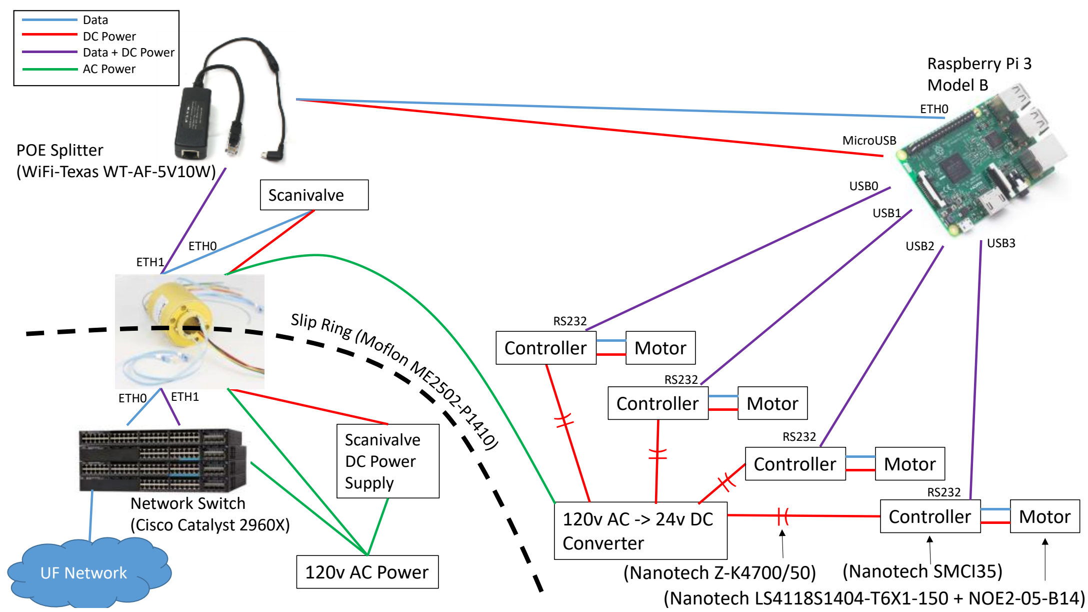

Figure 10. Wiring diagram for stepper motor control.

3.4 Experimental equipment

Experiments were conducted in the BLWT located at the University of Florida Natural Hazard Engineering Research Infrastructure (NHERI) Experimental Facility. The BLWT is 6.1 m wide with a 1 m turntable centered along the 6.1 m width, 31.75 m downwind of 8 fans. The fans were operated at a constant 1050 RPM, corresponding to a reference height velocity of approximately 14 m/s. The pressures on the model building surfaces were measured using Scanivalve ZOC33 (2016) pressure scanners. The rigid model building installed in the BLWT is shown in Figure 11.

Figure 11. Boundary layer wind tunnel with model low-rise building, upwind view.

3.5 Tap tributary areas

The pressure measured at each pressure tap was assumed to act over non-overlapping tributary areas on the envelope of the model. Voronoi diagrams derived from Delaunay triangulation were used to calculate the tributary area of each tap (Gierson et al., 2017). This is a reproducible, automated process – important when the envelope shape is changing during optimization. The flattened view of taps and corresponding tributary areas for the model with a parapet height of 4.50 inches (model-scale) is illustrated in Figure 12.

Surfaces 1 through 4 correspond to the four outer building walls. Surfaces 6 through 9 are inner parapet walls for a parapet height $h_p > 0$. The edges that join the outer building walls (Surfaces 1 to 4) and the inner parapet walls (Surfaces 6 to 9) in Figure 12 are located at the vertical height of the parapet of the physical model. They do not touch on the physical model, but instead are separated by the thickness of the parapet (in this case 1-inch model-scale). Surfaces 5 and 10 are the top of the parapet wall and the building roof, respectively. Additional pressure taps are exposed on the inner parapet walls with increasing height. As the parapet height increases, the tributary areas for the outer building walls and inner parapet walls increases, while the tributary areas for both the top of the parapet wall and the building roof remained constant.

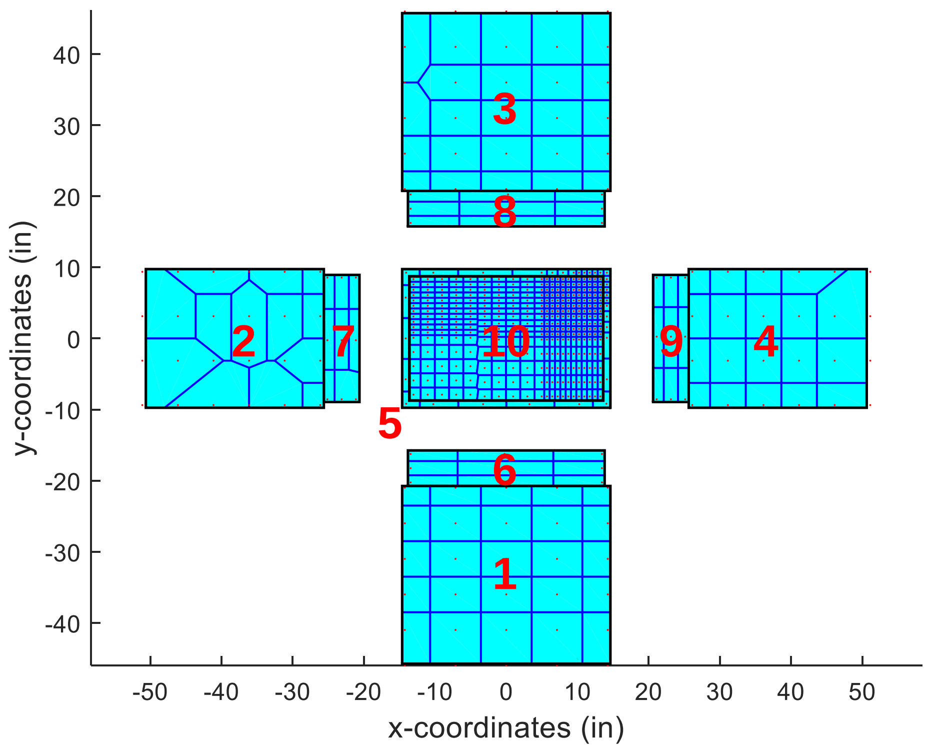

Figure 12. Tap locations, tributary areas, and surface numbers on a flattened representation of the model with a parapet of 4.50 inches (dimensions are in model-scale).

3.6 Base shear force calculation

Horizontal base shear forces were calculated for the direction perpendicular to the long building dimension because this direction was found to control the base shear design. Synchronous measurements from pressure taps located at the windward, leeward, and parapet walls (Surfaces 1, 3, and 6 and 8 in Figure 12, respectively) were multiplied by the tap tributary areas to obtain local base shear force contributions. The total base shear time history was then obtained from the summation of these forces as follows:

$$B_{shear}(t) = \sum_{i=1}^{n} p_i(t) A_i \, \lambda_U^2 \lambda_L^2 \tag{14}$$

where $B_{shear}(t)$ is the equivalent full-scale base shear, $p_i(t)$ is the pressure time history of tap i, A_i is the tributary area of tap i, n is the total number of taps, λ_U is the velocity scale, and λ_L is the length scale (1:18). A full-scale reference mean velocity of 40 m/s was assumed, resulting in $\lambda_U = 3.33$ (U_{BLWT} = 12.1 m/s). The peak base shear $\hat{B}_{shear}$ was estimated from a Fisher-Tippett Type I (Gumbel) distribution with 50 peaks and a probability of non-exceedance of 78%.

3.7 Wind simulation

Simulation of upwind terrain roughness was performed via the Terraformer, an automated terrain generator located upwind of the BLWT testing section. The Terraformer is capable of rapidly reconfiguring both the height and orientation of 1116 elements in a 62 × 18 roughness element grid to achieve specific upwind terrain conditions (Fernández-Cabán & Masters, 2017). Dimensions of the elements are 5 cm by 10 cm in plan, and they are spaced 30 cm apart in a staggered pattern. The height and orientation of each element can be independently varied from 0-160 mm and 0-360°, respectively to simulate a wide range of homogeneous or heterogeneous upwind terrain conditions. For this study, the Terraformer was configured to a uniform element height of h = 20 mm and the wide face of each element was oriented perpendicular to the incident flow. This configuration was selected to simulate open terrain exposure for a geometric scale of 1:18.

Figure 13a depicts the normalized mean velocity profile at a height of 610 mm for the wind velocity tested, where the mean velocity profile was normalized by the reference mean wind velocity U_{ref} measured at a height z_{ref} = 1.48 m. Directional velocity and static pressure measurements were collected at the center of the BLWT testing section without the model installed using Turbulent Flow Instrumentation Cobra probe sensors mounted to an automated gantry system. Each velocity measurement was taken for 120 seconds at a sampling rate of 1250 Hz. A roughness length estimate of 1.59 mm was obtained from a non-linear least-squares fit of the log law in the inertial-sublayer region (z ~ 150-900 mm), following the curve-fitting method in Karimpour et al. (2012). This results in an equivalent full-scale roughness length of 0.029 m, which is within the range of open terrain as defined in ASCE 7-16. The measured spectra was compared with the power spectra model in ESDU (1974), and first derived by von Kármán for isotropic turbulence (Von Karman, 1948). The measured longitudinal integral length scale (L_u^x) in the tunnel at z = 610 mm was 1.06 m. For a 1:18 simulation, this results in a full-scale L_u^x = 18 m (z ~ 11 m), which is ~16% of the expected L_u^x for open terrain – e.g., for z_0 = 0.03 m and z = 10 m, L_u^x = 110 m (ASCE/SEI 49-12). The challenges associated with achieving sufficient length scales of turbulence in the BLWT for large models (e.g., low-rise buildings) are well established (Stathopoulos & Surry, 1983; Tieleman, 2003). The discrepancy in L_u^x

(model versus full-scale) arises from the absence of large-scale turbulence in the BLWT. Recent methods, such as partial turbulence simulation (Mooneghi et al., 2016), have been successful in compensating for a lack of large-scale turbulence. Nevertheless, the mismatch in integral lengths does not detract from the fundamental objective of applying CPS approaches in the BLWT.

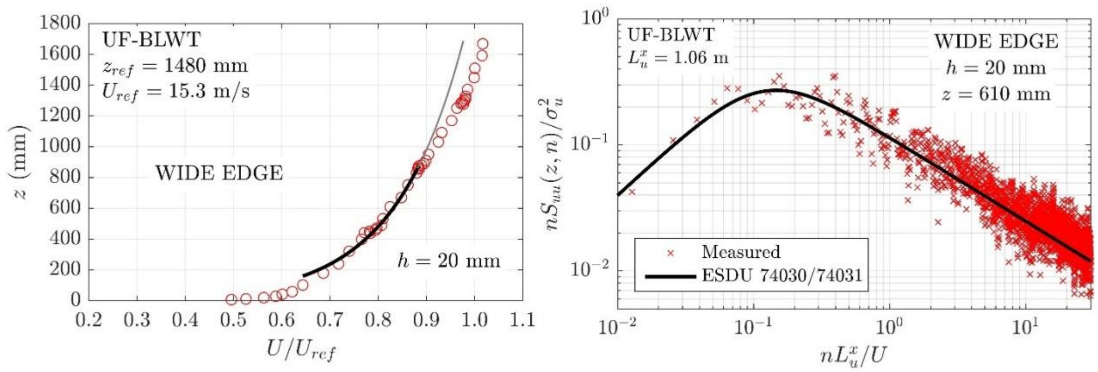

(a) (b)

Figure 13. (a) Mean velocity profile and (b) longitudinal turbulence spectra (z = 610 mm) measured at the center of the test section for h = 20 mm and a wide edge windward element orientation.

3.8 Assessment of pressure coefficients

Differential pressures from 512 taps were simultaneously sampled at 625 Hz for 120 seconds, corresponding to approximately 660 seconds full-scale assuming a basic wind speed of 40 m/s at reference height. Pressure coefficients were referenced to the velocity pressure at the model eave height. This velocity pressure was obtained indirectly by applying a reduction factor to pitot tube measurements at the freestream (*z* = 1.48 m).

The maximum and minimum pressure coefficients for each tap for a particular time history were estimated using a Gumbel distribution as outlined in 2.4.1 with $n =$

50 segments of equal length. The peak maximum and minimum pressure coefficients from each segment were calculated using Equation (1), and maximum and minimum C_p values for the entire time history were estimated using a probability of non-exceedance of $p = 78\%$.

3.9 Summary

In this chapter the parameters of the rigid, low-rise parapet building model and actuation system were described in detail, including the design variable, geometric properties and materials for fabrication. The framework for providing communication and power to the actuation system control was detailed; the model and actuation system are an integral component of testing as the physical component of the CPS.

The experimental equipment used for experimental testing is described, including the Scanivalve ZOC33 pressure scanners and the BLWT used for all testing of the rigid, low-rise parapet model. The details of the simulation of upwind open terrain are presented. In addition, C_p pressure coefficients across tap tributary areas are derived from raw pressure tap data. These pressure coefficients will form the basis of performance evaluation during optimization.

Chapter 4: Rigid Model Testing and CPS Optimization

This chapter describes the approach for formulating the different optimization problems which were examined using the rigid model. A better understanding of the expected pressure envelope had been developed from a previously obtained test matrix (Whiteman et al., 2018). Multiple different modifications to the standard PSO algorithm are proposed for incorporation into a modified single-objective PSO (SO-PSO) algorithm. The results and analysis for the different optimization techniques – single-objective stochastic, single-objective non-stochastic, and multi-objective stochastic optimization are subsequently presented.

4.1 Problem formulation

As the parapet height increases, the peak suction nominally decreases for the roof surface and top of the parapet wall and increases for the inner parapet wall surfaces. Also, an increase in parapet height increases the peak positive pressure on the roof surface and windward side of the leeward parapet. Additionally, a taller parapet increases the projected building area normal to the flow of wind, increasing the base shear of the structure. The aforementioned observations are not comprehensive; however, they include all effects that influenced the optimal design. Critical $\hat{C}_p$ values were observed for suction, positive pressure, and base shear at approach wind angles of 45° (Figure 14), 90° (Figure 15), and 0°, respectively. To minimize the number of boundary layer wind tunnel (BLWT) runs, each candidate solution was only tested from among the set of angles of 0°, 45°, and 90° based on the objective function. All optimization problems were physically constrained by the model-scale minimum and maximum parapet height of 0 and 4.50 inches, respectively. The lower and upper physical bounds of the parapet height were chosen so that the optimal solution for the objective function was confidently located within the search space rather than at a physical bound. The model-scale parapet heights were rounded to the nearest 0.01 inches, consistent with a full-scale design discretization of 0.18 inches. A summary of the details of all non-stochastic and stochastic optimization problems performed incorporating the low-rise parapet model is presented in Table 2 and Table 3.

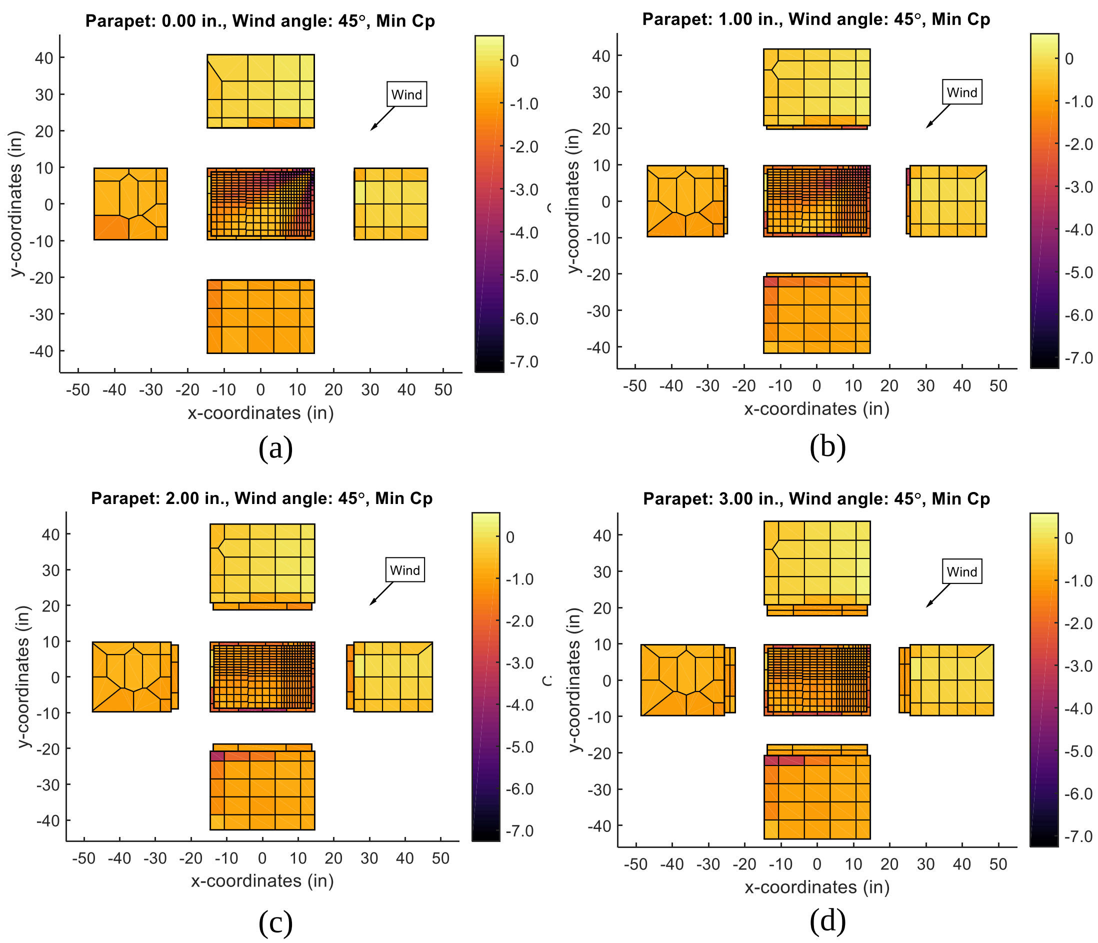

Figure 14. Minimum Cp for 45°, (a) 0-inch parapet, (b) 1-inch parapet, (c) 2-inch parapet, and (d) 3-inch parapet (dimensions are in model-scale).

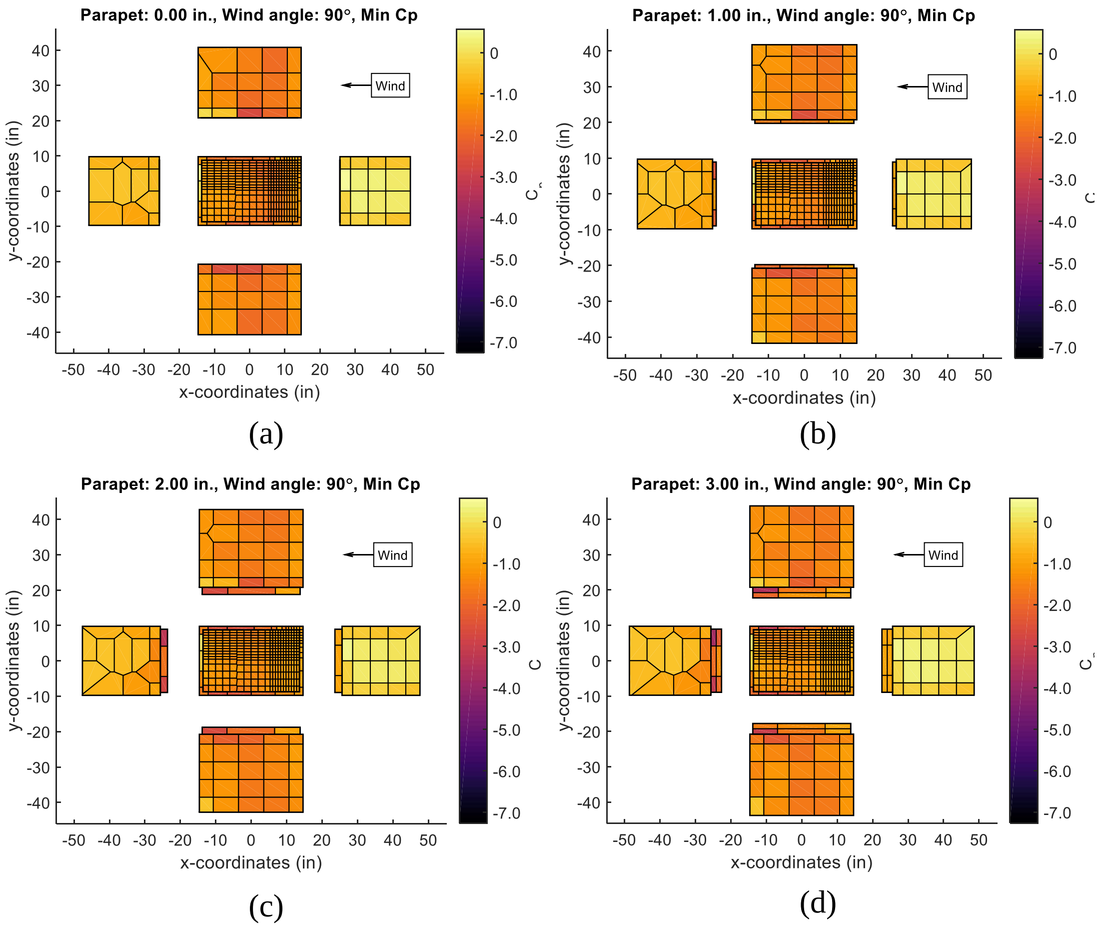

Figure 15. Minimum Cp for 90°, (a) 0-inch parapet, (b) 1-inch parapet, (c) 2-inch parapet, and (d) 3-inch parapet (dimensions are in model-scale).

Table 2. Comparison of details of non-stochastic optimization algorithms.

	Search algorithm	
	GSS (Case 1)	GSS (Case 2)
Objective statement [Minimization]	Magnitude of peak suction	Magnitude of peak suction and positive pressure
Objective function	minimize $\lvert\min(\hat{C}_{p,min})\rvert$	minimize $\max(\lvert\min(\hat{C}_{p,min})\rvert, \lvert\max(\hat{C}_{p,max})\rvert)$
Surfaces considered (Figure 12)	Roof, inner parapet, and top of the parapet (Surfaces 5-10)	Roof, inner parapet, and top of the parapet (Surfaces 5-10)
Approach wind angles considered	45° and 90°	45° and 90°
Result summary	Chapter 4.3.1	Chapter 4.3.2

Table 3. Comparison of details of stochastic optimization algorithms.

	Search algorithm

	Modified single-objective PSO	Multi-objective PSO
Objective statement [Minimization]	Magnitude of peak suction	Magnitude of peak suction; Magnitude of peak base shear
Objective function	minimize $\left\|\min\left(\hat{C}_{p,min}\right)\right\|$	minimize $\left\|\min\left(\hat{C}_{p,min}\right)\right\|$; minimize $\left\|\hat{B}_{shear}\right\|$
Surfaces considered (Figure 12)	Roof, inner parapet, and top of the parapet (Surfaces 5-10)	Roof (Surface 10); Along-wind surfaces
Approach wind angles considered	45° and 90°	0° and 45°
Result summary	Chapter 4.2	Chapter 4.4

4.2 Modified single-objective particle swarm optimization (SO-PSO)

The objective function for the modified SO-PSO algorithm was selected as a minimization of the suction on the building roof and all parapet surfaces (i.e., the inner parapet walls and top of the parapet) considering all wind angles (Surfaces 5-10 in Figure 12). Each candidate solution was evaluated at approach wind angles of 45° and 90° to minimize the number of BLWT runs, as these angles were expected to produce critical $\hat{C}_p$ values. Considering the time limit on experimental resources, a balance was needed between sufficient particles to create the PSO swarm effect and sufficient iterations to converge. Based on an estimated 120 seconds per BLWT run, 60 seconds for all actuation before each BLWT run, and a day of testing, five particles were selected.

The cyber-physical optimization approach specialized for PSO, a predetermined set of evaluation wind angles, and the low-rise parapet model is shown in Figure 16. Loops over all angles, all particles, and all iterations are highlighted to clearly illustrate the experimental timeline.

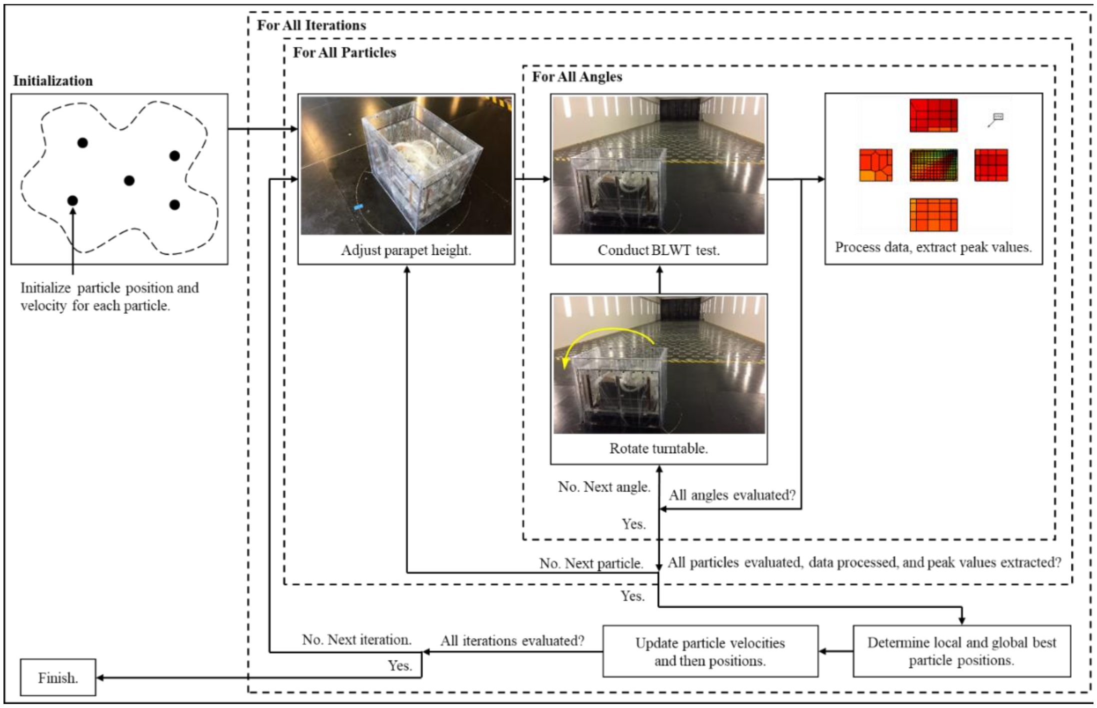

Figure 16. Cyber-physical optimization approach as implemented with PSO.

These experiments were driven by a modified PSO algorithm. Modifications were made to increase the computational efficiency and reduce the number of experiments required. Additionally, the accuracy of the approach was improved by addressing issues which arise with both the cyber and physical components. The issues of premature convergence (cyber) and sensitivity to outliers (physical) were identified and modifications were introduced for evaluation.

4.2.1 Fly-back mechanism: address constraint violations

Traditional PSO does not address particles which violate design constraints. Thus, constrained optimization was introduced to address this problem through the use of a fly-back mechanism. In the traditional fly-back mechanism, a particle that would violate a design constraint is prevented from moving for that iteration. The algorithm proceeds as normal for the next iteration. The global minima (or maxima, depending on objective) of design problems are often close to the boundaries of the feasible search space (He et al., 2004). The traditional fly-back mechanism will exploit solutions around the boundaries. In this study, the solution was not expected to be near the boundaries. Therefore, in addition to preventing the particle from moving beyond the boundary, the direction of the velocity was reversed (i.e., the velocity now points away from the boundary). This modification enables better exploration of the interior of the search space.

4.2.2 Smartest particle: avoid premature convergence

PSO can prematurely converge to solutions found in early iterations if not properly calibrated (Banks et al., 2008). Recalling Equation (8), the calculation of the velocity vector for each particle at iteration j depends on the best-known position of all particles considering iterations 1 through j. If the global best position corresponds to a local optimum, then premature convergence may occur as all particles are attracted to this solution. If weight is placed on the position of the particle which found the global best position, rather than the global best position itself, then premature convergence can be avoided. This particle, the "smartest" particle, will encourage continued exploration by avoiding stagnation of the p_j^g term.

Following the current position of the global best particle rather than its global best positions leads to a new definition for velocity updates

$$v_{j+1}^i = wv_j^i + c_1 r_1 \frac{\left(p_j^i - x_j^i\right)}{\Delta t} + c_2 r_2 \frac{\left(x_j^g - x_j^i\right)}{\Delta t} \quad (15)$$

where r_1 and r_2 are independent random numbers in the range [0,1], w is the inertia of the particle, c_1 and c_2 are two trust parameters indicating a particle's trust in itself and trust in the swarm respectively, p_j^i is the best known position of particle i considering iterations 1 through j, x_j^g is the position at iteration j of the particle g which determined the best known position of all particles considering iterations 1 through j, and Δt is the time step value.

4.2.3 Forgetting function: avoid sensitivity to others

BLWT testing is subject to the chaotic nature of wind and the measurement equipment; results will vary from experiment to experiment, even for the same specimen configuration. Extreme values may be associated with a specimen configuration that are not truly representative of that configuration. With regard to PSO, a non-representative test (i.e., an outlier) can affect both a particle's local best solution and the swarm's global best solution. Even if these extreme values are unrepeatable, they may be retained as the local or global best solution for the remainder of the optimization. Outliers can potentially cause convergence to a position that does not accurately represent the global best position. To address the variability of wind tunnel testing, a modification to the PSO algorithm was proposed.

A "forgetting function" was introduced to the swarm so that particles within the swarm suffer a partial loss of memory and "forget" both global and local best solutions. In evaluating global and local best costs, the modified PSO algorithm would only consider solutions that were created within a specified number of previous iterations. The corresponding positions for this limited horizon will become the new global and local best particle positions. If the solution of a particular parapet height was the result of an outlier experiment, then it would eventually be forgotten, and the global and local best particle positions would be updated in its absence. With the forgetting function, the convergence to the global solution may no longer be monotonic.

After performing simulated (offline) optimization trials using previously recorded data, the number of iterations to consider for global and local best calculations was selected to be 5 (i.e., the current iteration and 4 previous iterations).

The modified velocity equation considering the forgetting function is then defined as expressed by Equation (16) as

$$v_{j+1}^{i} = w v_{j}^{i} + c_1 r_1 \frac{\left(p_k^{i} - x_j^{i}\right)}{\Delta t} + c_2 r_2 \frac{\left(p_k^{g} - x_j^{i}\right)}{\Delta t} \tag{16}$$

where p_k^i is the best known position of particle i considering iterations $(j - j_k)$ through j and p_k^g is the best known position of all particles considering iterations $(j - j_k)$ through j.

4.2.4 Minimization of peak suction

The problem-specific parameters of $w, c_1,$ and c_2 were selected to be 0.5, 1.0, and 1.0 respectively so that an equal weight would be placed on the particle’s inertia, trust in itself, and trust in the swarm by giving the products of $c_1 r_1$ and $c_2 r_2$ each a mean of 0.5. The position of the particles was initially randomly distributed across the range of positions. A total of 15 design iterations were conducted for the 5 particles.

The convergence of the particles towards the optimum model-scale height of 2.70 inches (4.05 feet full-scale) is shown in Figure 17a. All five particles within the swarm converged to the global best cost with the incorporation of the smartest particle (Figure 17a). The loss of diversity of individuals within a population is a symptom of premature convergence because of the loss of the exploration capabilities of the individuals. Rather than having multiple particles close to one another in position and following similar search paths, the particles in Figure 17a retain their diversity.

The global best cost for each iteration is shown in Figure 17b. Points with both particle number and cost identified represent an update to the global best cost. Figure 18 and Figure 19 depict the envelope plot of the minimum C_p for the optimal parapet height at 45° and 90° respectively. This illustrates the balance in minimum C_p on the roof and top of the parapet wall (Figure 18) and inner parapet wall surfaces (Figure 19). This balance is expected because the suction on the roof, top of the parapet, and inner parapet walls were given equal weight in the objective function.

The global best cost non-monotonically converges with the incorporation of the forgetting function. The global best position determined at iteration 10 of 2.68 inches model-scale (4.02 feet full-scale) attracts all particles to this height. Despite repeated testing of this particular position after it is found to be the global best position, the position of 2.70 inches model-scale (4.05 feet full-scale) is found to produce a better cost once the particular test at iteration 10 is forgotten. This suggests that the solution found to be the global best at iteration 10 was not representative of the height of 2.68 inches model-scale (4.02 feet full-scale) and can be considered an outlier. Similarly, the solution at 2.70 inches model-scale (4.05 feet full-scale) may be an outlier, which would be revealed by continued testing.

The optimal result corresponds to a full-scale parapet height of 4.05 feet, an otherwise non-intuitive design. This parapet height simultaneously minimizes suction on the roof and parapet surfaces (i.e., the inner parapet walls and top of the parapet). According to the Building Code Requirements for Masonry Structures, the height of structural parapets should not exceed 3 times their thickness (ACI/ASCE/TMS, 2011). The optimal full-scale height found satisfies this limit of 4.50 feet as applied to the current building.

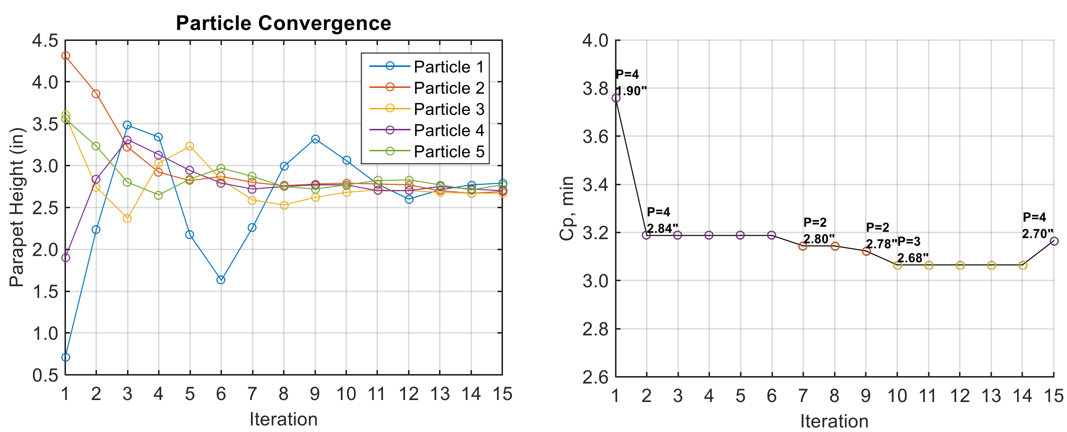

(a) (b)

Figure 17. (a) Particle convergence at each iteration and (b) Iteration history of global best cost (dimensions are in model-scale).

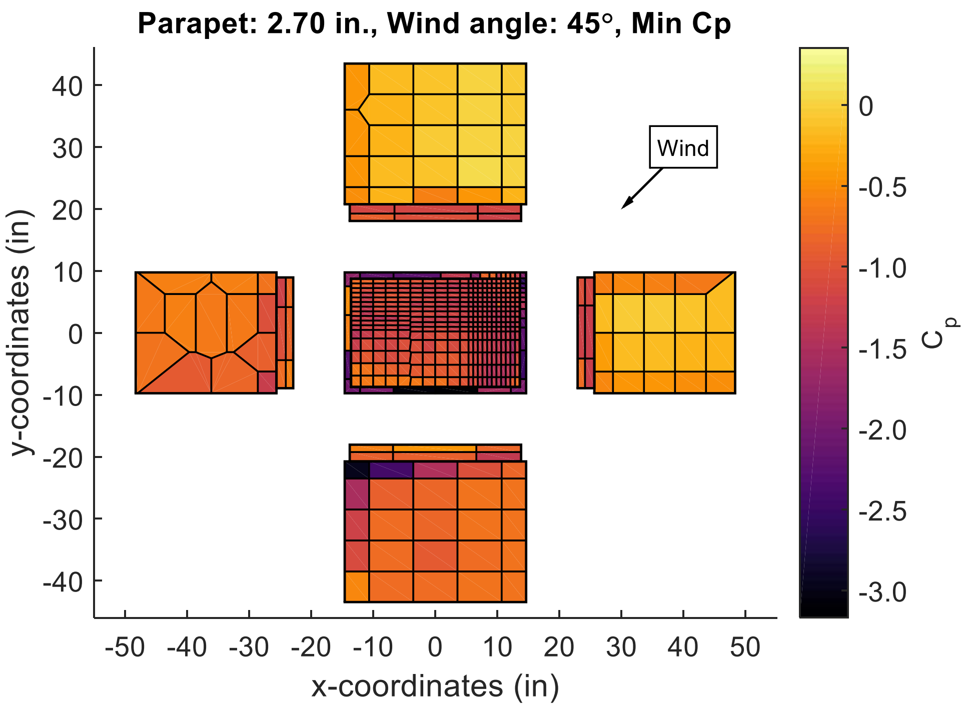

Figure 18. Minimum Cp for optimal parapet height, 45° wind angle shown (dimensions are in model-scale).

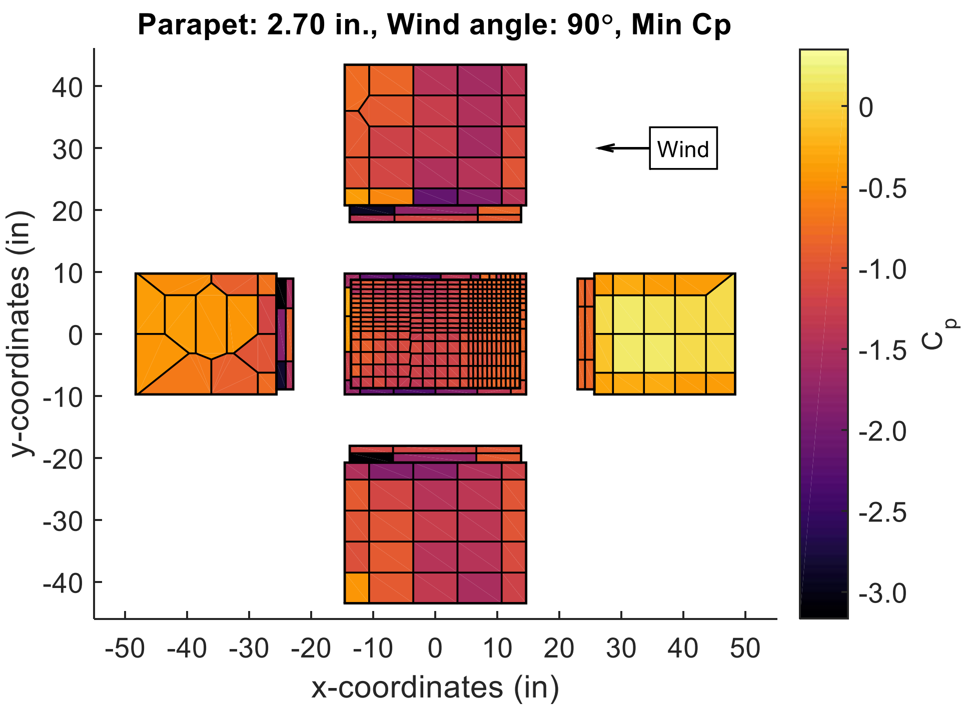

Figure 19. Minimum Cp for optimal parapet height, 90° wind angle shown (dimensions are in model-scale).

4.3 Golden section search (GSS)

Single-objective optimization was performed on the parapet model using GSS integrated into the CPS approach. Two alternative objective functions were considered using GSS: (1) minimizing the magnitude of peak suction on the roof, inner parapet walls, and top of the parapet (Surfaces 5-10 in Figure 12) and (2) minimizing the magnitude of peak suction and positive pressure on the roof, inner parapet walls, and top of the parapet (Surfaces 5-10 in Figure 12). Each candidate solution was evaluated at approach wind angles of 45° and 90° to minimize the number of BLWT runs, as these angles were expected to produce critical $\hat{C}_p$ values. A tolerance of 0.001 inches (model-scale) was selected for the GSS algorithm to ensure that the search space converged to a single parapet height. Based on the desired tolerance and Equation (6), a total of 18 design iterations were performed.

4.3.1 Minimization of peak suction (Case 1)

Large suction can be damaging to both components and cladding or contribute to windborne debris. Increasing the parapet height will reduce the suction on the roof surface, the major benefit of installing parapet walls. At the same time, increasing the parapet height will increase the suction on the inner parapet walls. This balance creates the design tradeoff explored in Case 1. The objective is selected as a minimization of the maximum magnitude of the peak suction considering the building roof and parapet surfaces (i.e., the inner parapet walls and top of the parapet).

CPS optimization was conducted with results summarized in Table 4 and Figure 20. Peak suction values for both GSS intermediate points at each iteration are shown in Table 4. The convergence of the search space towards the optimum height of 2.80 inches model-scale (4.20 feet full-scale) is shown in Figure 20. The initial domain bounds (iteration 1) were [0, 4.50] inches. At iteration 1, the intermediate points produced model-scale parapet heights h_p of 1.72 inches and 2.78 inches based on Equation (3) and (4). The measured $\hat{C}_{p,min}$ of the two intermediate points were 4.71 and 4.24 (Table 4). Since the objective function was to reduce $\hat{C}_{p,min}$ (suction only for Case 1), $h_p = 2.78$ inches was a better candidate design than 1.72 inches. As a result, the domain [0, 1.72] inches was discarded and the domain bounds for the next iteration (iteration 2) became [1.72, 4.50] inches. This procedure was repeated for the maximum number of iterations.

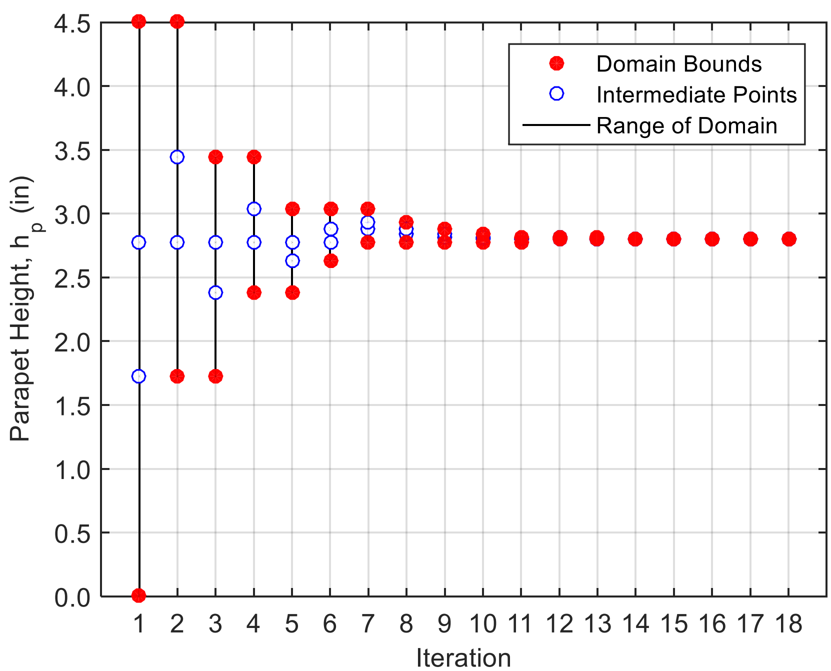

Figure 20. Parapet height iteration history using GSS (Case 1) (dimensions are in model-scale).

Table 4. Parapet height and $\widehat{C}_{p,min}$ by iteration for GSS (Case 1) (dimensions are in model-scale).

Iteration	Intermediate Point, x_1		Intermediate Point, x_2	
	h_p [in]	$\hat{C}_{p,min}$	h_p [in]	$\hat{C}_{p,min}$
1	1.72	4.71	2.78	4.24
2	2.78	4.48	3.44	4.67
3	2.38	4.36	2.78	3.94
4	2.78	3.94	3.03	4.23
5	2.63	4.16	2.78	4.12
6	2.78	4.16	2.88	4.03
7	2.88	4.34	2.94	4.35
8	2.84	4.18	2.88	4.35
9	2.82	3.82	2.84	3.91
10	2.80	3.84	2.82	3.89
11	2.80	4.18	2.80	3.91
12	2.80	3.97	2.80	4.05
13	2.80	4.09	2.80	4.42
14	2.80	4.04	2.80	4.03
15	2.80	3.84	2.80	4.23
16	2.80	3.93	2.80	3.81
17	2.80	3.90	2.80	3.96
18	2.80	4.10	2.80	4.38

Table 5. Parapet height and max($|\widehat{C}_{p,min}|$, $|\widehat{C}_{p,max}|$) by iteration for GSS (Case 2) (dimensions are in model-scale).

Iteration	Intermediate Point, x_1		Intermediate Point, x_2	
	h_p [in]	max($|\hat{C}_{p,min}|$, $|\hat{C}_{p,max}|$)	h_p [in]	max($|\hat{C}_{p,min}|$, $|\hat{C}_{p,max}|$)
1	1.72	4.69	2.78	3.94
2	2.78	4.28	3.44	4.88
3	2.38	4.57	2.78	3.93
4	2.78	4.16	3.03	4.35
5	2.63	4.21	2.78	4.19
6	2.78	4.25	2.88	4.36
7	2.72	4.00	2.78	4.20
8	2.69	3.95	2.72	3.95
9	2.72	4.11	2.74	4.24
10	2.71	4.00	2.72	4.02
11	2.71	3.99	2.71	3.96
12	2.71	3.82	2.71	3.89

13	2.71	4.11	2.71	4.03
14	2.71	3.99	2.71	4.02
15	2.71	4.02	2.71	4.20
16	2.71	4.06	2.71	4.16
17	2.71	4.00	2.71	3.98
18	2.71	3.96	2.71	4.03

The variability of peak suction due to the experimental testing is seen for iterations 12 through 18, as both intermediate points have the same parapet heights for these iterations. Despite being at the same height, the measured $\hat{C}_{p,min}$ for iterations 12 through 18 vary between intermediate points and across iterations. Figure 21 and Figure 22 depict the plot of the $\hat{C}_{p,min}$ values on the envelope of the building for the optimal parapet height at 45° and 90° respectively. This illustrates the balance in large magnitudes of $\hat{C}_{p,min}$ on the roof and top of the parapet wall (Figure 21) and inner parapet walls (Figure 22). Lowering the parapet would increase suction on the roof at 45° while raising the parapet would increase suction on the inner parapet walls at 90°. This balance is expected because the suction on the roof, top of the parapet, and inner parapet walls were given equal weight in the objective function. The optimal result corresponds to a full-scale parapet height of 4.20 feet. This parapet height simultaneously minimizes suction on the roof and inner parapet walls. According to the Building Code Requirements for Masonry Structures, the height of structural parapets should not exceed 3 times their thickness (ACI/ASCE/TMS, 2011). The optimal height found satisfies this limit of 4.50 feet as applied to the current building.

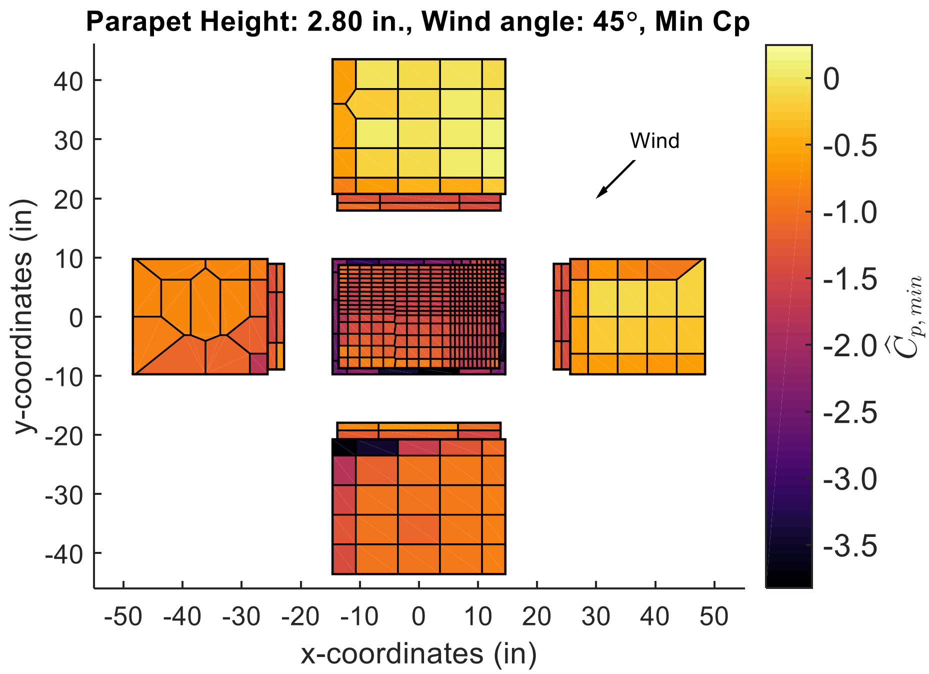

Figure 21. $\widehat{\boldsymbol{C}}_{\boldsymbol{p,min}}$ for optimal parapet height, 45° wind angle shown (dimensions are in model-scale).

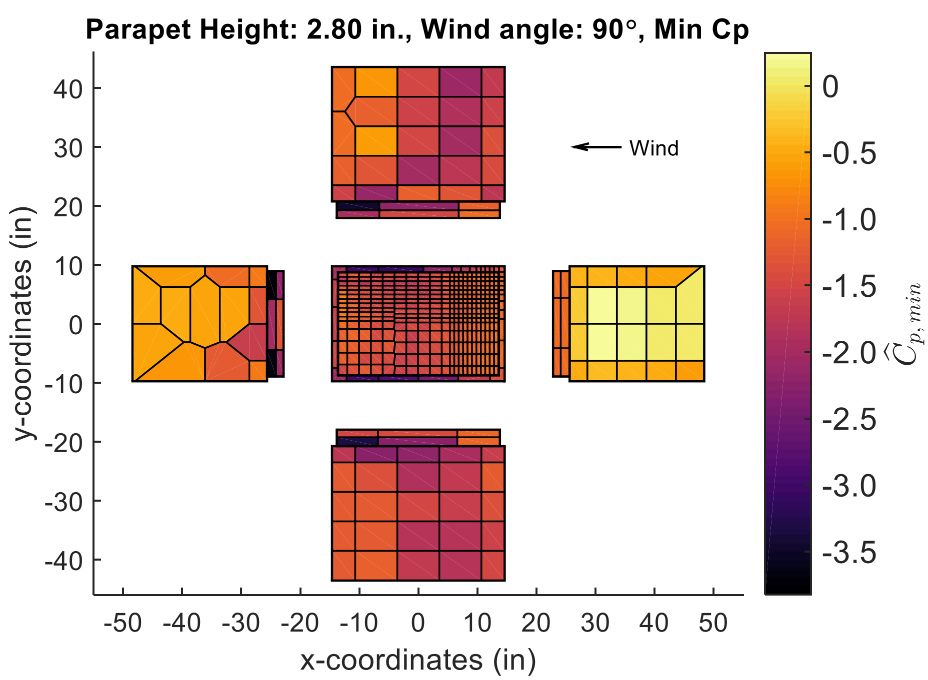

Figure 22. $\widehat{\boldsymbol{C}}_{\boldsymbol{p,min}}$ for optimal parapet height, 90° wind angle shown (dimensions are in model-scale).

4.3.2 Minimization of peak suction and positive pressure (Case 2)

As the parapet height increases, the positive pressure increases for regions of the roof and the windward side of the leeward parapet. Positive pressures on the roof are additive to gravity loads, which can increase the forces on structural members. Positive pressures on the windward side of the leeward parapet wall are additive to the base moment and base shear of the parapet wall and the structure. Formally, the objective of Case 2 is to minimize the maximum magnitude of peak suction and peak positive pressures on the roof and parapet surfaces (i.e., the inner parapet walls and top of the parapet). The relative importance of reducing suction versus positive pressure is not considered; they are treated equally.

CPS optimization was conducted with results summarized in Table 5 and Figure 23. The maximum of ($|\hat{C}_{p,min}|$, $|\hat{C}_{p,max}|$) for both intermediate points at each iteration is shown in Table 5. The convergence of the search space towards the optimum model-scale height of 2.71 inches (4.07 feet full-scale) is shown in Figure 23. Similar to Case 1, there is variability of the maximum suction due to the experimental testing best seen for iterations 12 through 18. For both angles of 45° and 90°, the peak suction on the surfaces considered is greater in magnitude than the peak positive pressure and therefore governs the design. The results for the envelope of peak suction pressures at the optimal parapet height are similar to those of Figure 21 and Figure 22. The optimal height corresponds to a full-scale parapet height of 4.07 feet, which satisfies the limit of 4.50 feet according to the Building Code Requirements for Masonry Structures as applied to the current building (ACI/ASCE/TMS, 2011).

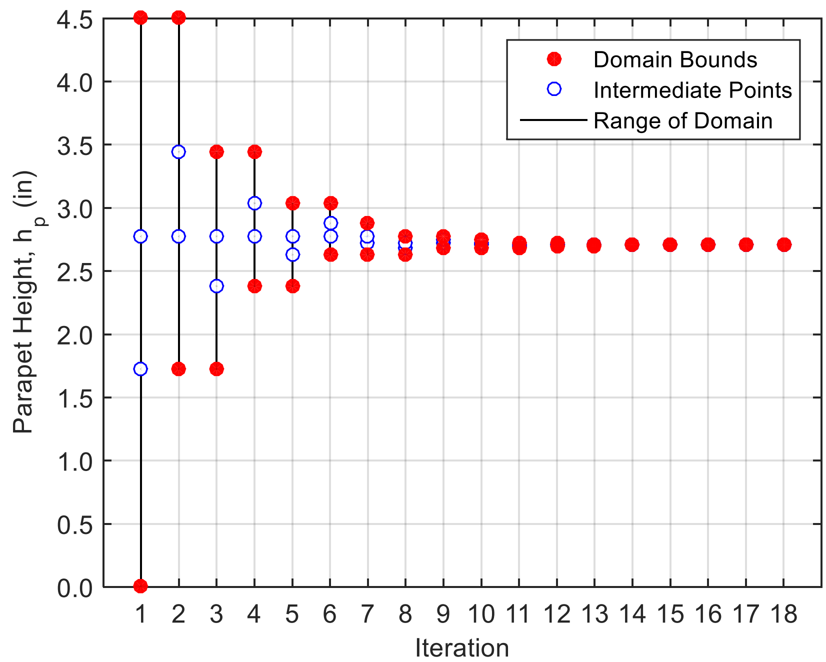

Figure 23. Parapet height iteration history using GSS (Case 2) (dimensions are in model-scale).

4.4 Multi-objective particle swarm optimization (MO-PSO)

Multi-objective optimization was performed on the low-rise building using MO-PSO integrated into the CPS. The objective was to determine the optimal parapet height that achieves the best compromise in reducing peak suction on the roof (Surface 10 in Figure 12) and peak building base shear (Chapter 3.6). As the parapet height increases, the peak suction nominally decreases for the roof surface while the base shear of the structure increases. This introduces an expected tradeoff between objectives.

Assuming objective functions to both minimize the magnitude of suction pressure and minimize the magnitude of base shear, the proposed process for determining the cost for each particle at one example iteration is illustrated in Figure 24. Note that 100 particles are used to clearly illustrate the Pareto front. The cost is taken as the normalized distance *d* of the particle from the intersection of minimums. Particles that are not on the Pareto front are given an arbitrary high cost such that they are ignored, as there is an objectively better solution on the Pareto front. The process is reset at each iteration, only retaining the particle best and global best costs.

1. Identify the Pareto front and locate the intersection point of the minimum objective function values.

2. Normalize the distance between the minimum and maximum objective function values.

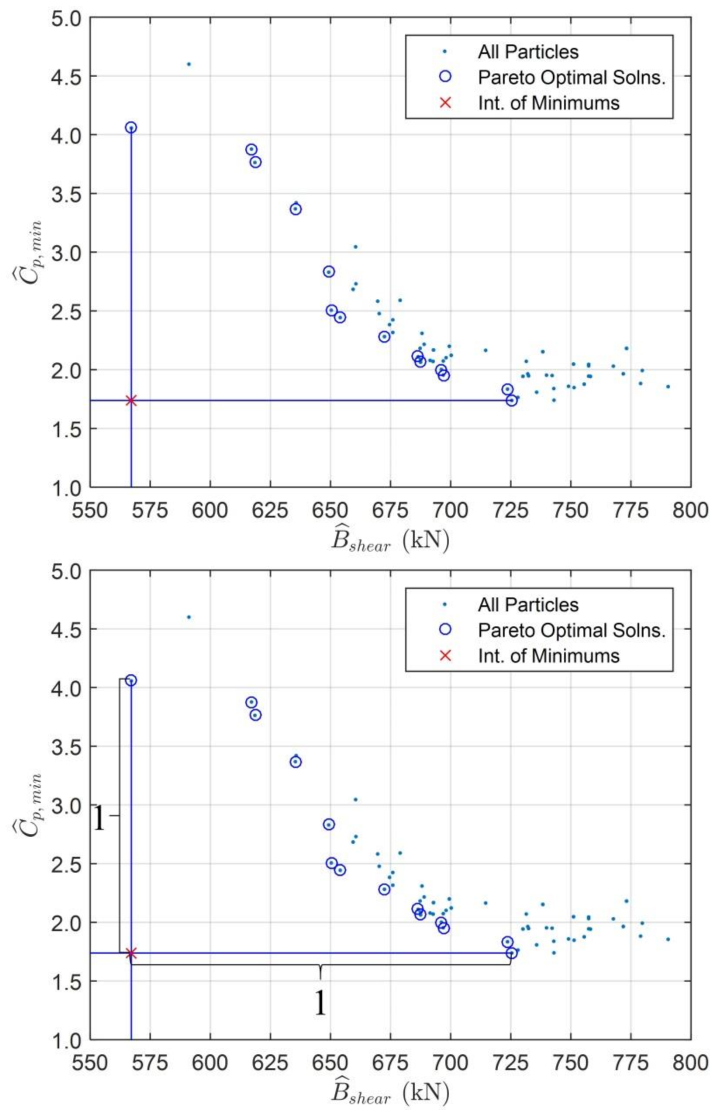

3. Calculate a particle's cost as the distance d between the particle and intersection point. Repeat for all particles on the Pareto front.

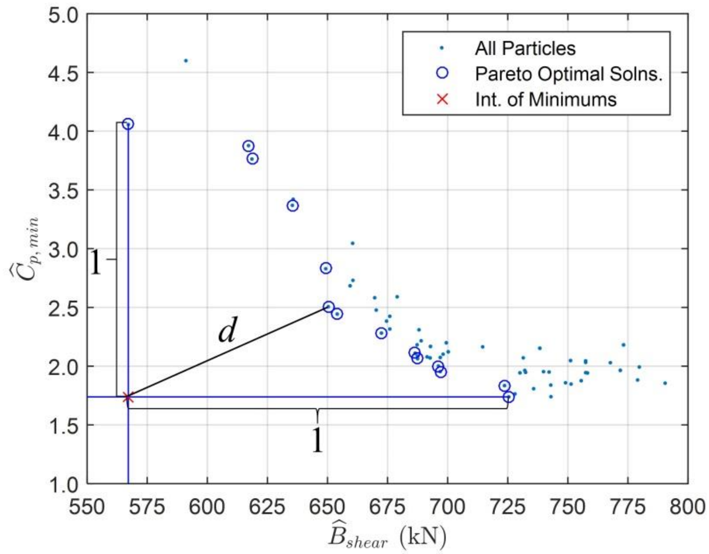

Figure 24. Procedure used for determining particle costs at each iteration.

4.4.1 Minimization of peak pressure and base shear

The problem-specific PSO parameters of $w, c_1,$ and c_2 were all selected as 0.5. These parameter values produced favorable convergence for a simulated (offline) optimization trial using previously recorded data from multiple wind angles and parapet heights. Each candidate solution was evaluated at approach wind angles of 0° and 45° to minimize the number of BLWT runs, as these angles were expected to produce critical base shear and $\hat{C}_p$ values, respectively. Considering the time limits on experimental resources, a balance was needed between sufficient particles to create the PSO swarm effect and sufficient iterations to converge. Additionally, an adequate swarm size was required to create a meaningful Pareto front with multiple Pareto optimal solutions. Based on an estimated 120 seconds per BLWT run, 60 seconds to set up the BLWT run, and two days of testing, 15 particles were selected.

The positions of the particles were initially randomly distributed within the pre-defined search space. A total of 10 iterations were conducted for the 15 particles with results summarized in Figure 25. The convergence of the particles towards the optimum model-scale height of 1.96 inches (2.94 feet full-scale) is shown in Figure 25a. 14 of the 15 particles converged toward the global best cost. The one particle which did not converge is due to the particle being equally attracted to both its personal best cost and the global best cost. The global best cost for each iteration is shown in Figure 25b. Points with both the particle number and the parapet height identified represent an update to the global best cost.

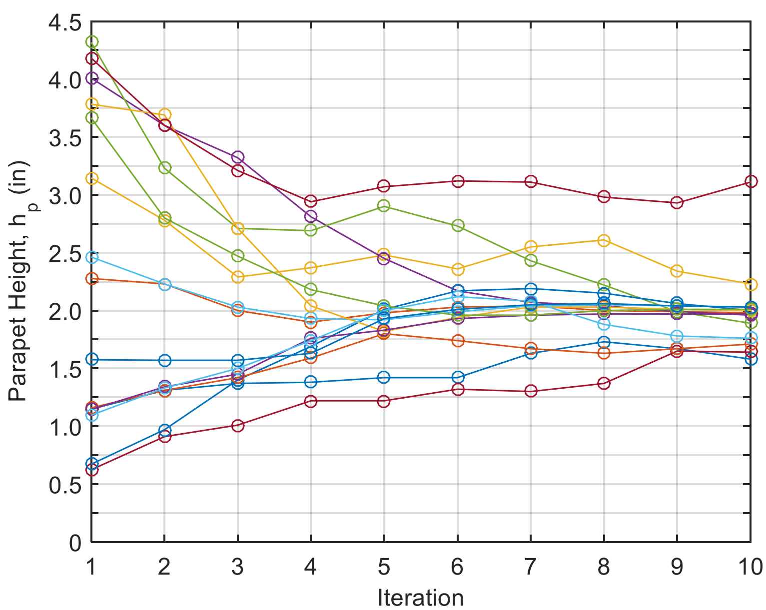

(a)

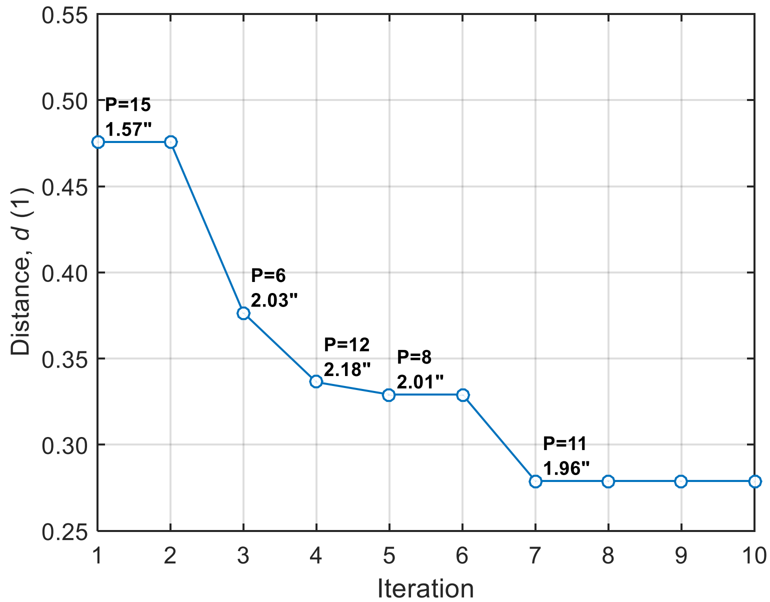

(b)
Figure 25. (a) Particle convergence at each iteration and
(b) Iteration history of global best cost (dimensions are in model-scale).

Figure 26 and Figure 27 depict the peak suction values $\hat{C}_{p,min}$ on the envelope of the building for the optimal parapet height at 0° and 45°, respectively. For the same height, the maximum peak base shear was 655 kN. Adding the base shear as a design consideration lowered the optimal parapet height in comparison to the single-objective cases due to the tradeoff that is experienced between the decreasing suction on the roof and increasing base shear for an increasing parapet height.

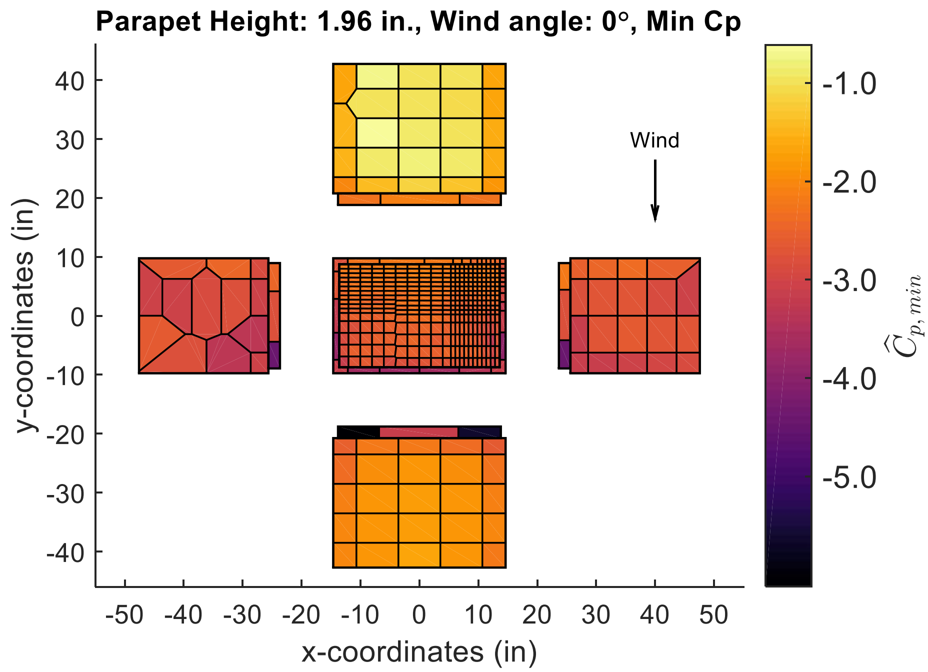

Figure 26. Minimum pressure coefficients for optimal parapet height, 0° wind angle shown (dimensions are in model-scale).

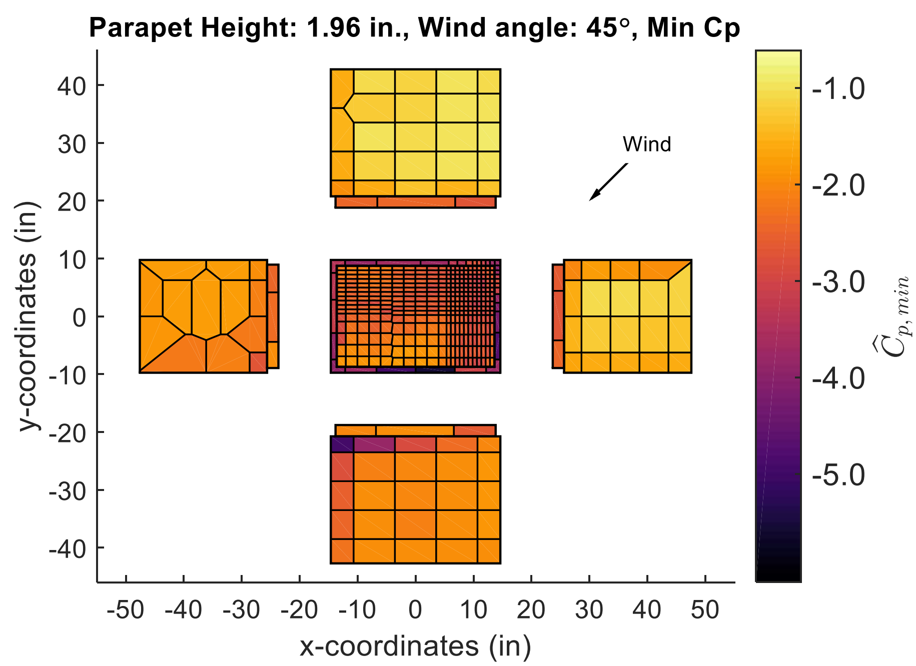

Figure 27. Minimum pressure coefficients for optimal parapet height, 45° wind angle shown (dimensions are in model-scale).

Figure 28a illustrates the Pareto front considering all of the candidate designs from all of the iterations for the defined objective functions (magnitude of peak suction and peak base shear), the intersection point of the minimum objective function values, and the solution closest to this intersection point. Figure 28b highlights the iteration that the global best cost is obtained, and the corresponding global best position. The solution obtained by the MO-PSO algorithm at the final iteration is identical to the solution considering all evaluated candidate designs over all iterations, indicating successful convergence.

The optimal design corresponds to a full-scale parapet height of 2.94 feet that minimizes suction on the roof and inner parapet walls and minimizes the base shear of the entire structure. This height satisfies the limit of 4.50 feet according to the Building Code Requirements for Masonry Structures as applied to the current building (ACI/ASCE/TMS, 2011).

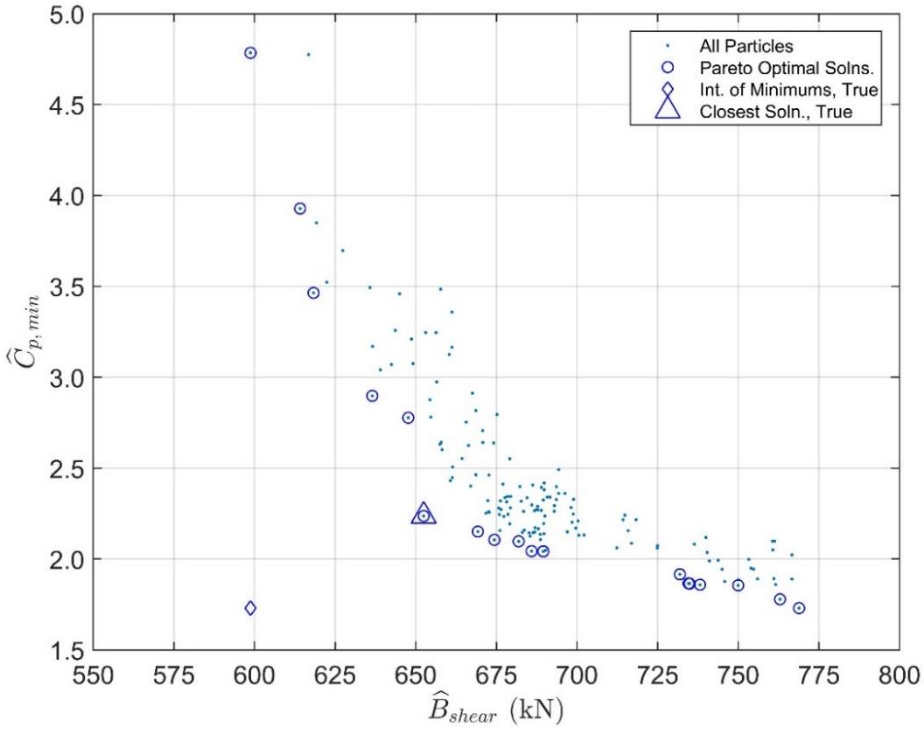

(a)

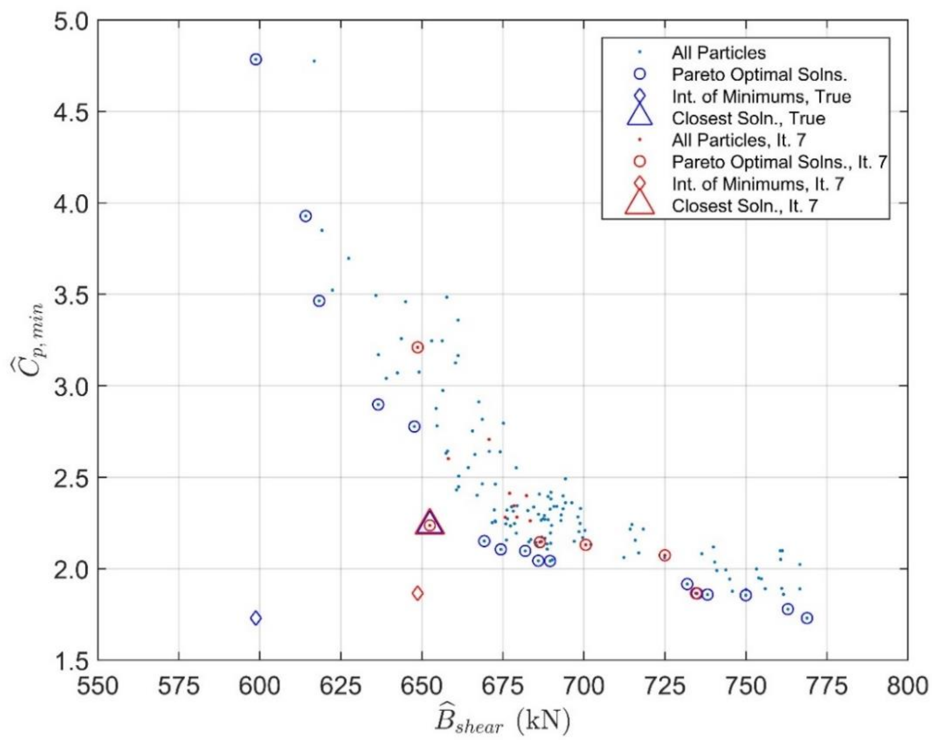

(b)

Figure 28. (a) Pareto front curve considering all iterations and (b) highlighting the iteration of global best cost.

4.5 Summary

In this chapter a combination of non-stochastic and stochastic optimization algorithms were implemented to minimize the magnitude of suction and positive pressures on the roof of the rigid, low-rise parapet building model, followed by stochastic multi-objective optimization to simultaneously minimize the magnitude of suction pressures and minimize base shear. Testing details for the low-rise parapet building model are presented in Table 6.

Table 6. Low-rise parapet building model testing details.

Test	GSS (Case 1)	GSS (Case 2)	SO-PSO	MO-PSO
Objective statement [Minimize]	Magnitude of peak suction	Magnitude of peak suction and positive pressure	Magnitude of peak suction	Magnitude of peak suction; Magnitude of peak base shear
Constraint(s)	Domain: [0, 4.50] in.	Domain: [0, 4.50] in.	Domain: [0, 4.50] in.	Domain: [0, 4.50] in.
Optimization method	GSS	GSS	PSO	PSO
Wind angle(s)	45° and 90°	45° and 90°	45° and 90°	0° and 45°
Optimal result (full-scale)	4.20 ft.	4.07 ft.	4.05 ft.	2.94 ft.
Results discussion	Chapter 4.3.1	Chapter 4.3.2	Chapter 4.2	Chapter 4.4

In contrast to single-objective optimization, a multi-objective problem formulation requires a user-defined relationship between independent objectives and the use of a Pareto front or another method of ranking candidate designs to obtain the optimal solution. When using a Pareto front, a sufficient population of candidate designs is required for each iteration to create a meaningful Pareto front with multiple Pareto optimal solutions. Therefore, more particles are required as compared to the single-objective case, resulting in more required experimental tests. A multi-objective problem formulation enables the analysis of competing design objectives which cannot be accurately evaluated using single-objective optimization.

PSO and other metaheuristics are well suited for multi-objective optimization. The formulation is problem independent, making it straightforward to include additional objective functions. Additionally, population-based search algorithms such as PSO are able to populate a meaningful Pareto front in a single iteration (Zhou et al., 2011). Alternatives such as gradient-based methods are sensitive to local minima, require continuous design objective functions, and are typically more computationally intensive. For the proposed model-in-the-loop approach to optimization, metaheuristic algorithms are better suited to address the competing objectives from multiple stakeholders.

Chapter 5: Aeroelastic Model Development and Experimental Setup

The capabilities of the CPS optimization framework were extended further to examine strength and serviceability limit states in the design and optimization of wind-sensitive tall building dynamics in a boundary layer wind tunnel (BLWT). Tall building design is more likely to include BLWT testing (as compared to low-rise buildings), providing a more practical application of the proposed CPS approach to design.

The proposed framework makes use of an aeroelastic building specimen with physically adjustable dynamic (i.e., stiffness) and aerodynamic (i.e., shape) properties. Aeroelastic models provide the capability of directly capturing the wind-induced dynamic response (e.g., accelerations and displacements) for immediate, accurate analysis without requiring modal analysis or finite element analysis. The specimen is instrumented with accelerometers and laser displacement sensors to directly capture and assess wind-induced response associated with complex fluid-structure interaction behavior. Numerical optimization algorithms were then integrated into the CPS framework to evaluate explicit structural performance criteria related to the serviceability of the structural system.

The development of the aeroelastic, tall building specimen and the experimental equipment used for all BLWT testing of the aeroelastic specimen for dynamics optimization is described in this chapter. The method for empirically deriving the lateral deflection from the measured tension readings is explained in this chapter as well. Finally, the procedure for estimating the full-scale building response with a Kalman filter using a limited number of acceleration and displacement measurements is presented.

5.1 Aeroelastic specimen

A 1:200 multi-degree of freedom aeroelastic tall building model was selected to test the CPS framework. The model is based on a prototype 76-story benchmark building presented in Yang et al. (2004). The fully-constructed specimen can be seen in Figure 29. The total height of the model was H = 1.53 m (model-scale). The skeleton of the model consisted of a 12.7 mm (0.5") square solid steel core (i.e., spine) that was rigidly bolted to seven aluminum plates acting as rigid diaphragms. The aluminum diaphragms were positioned every 187.5 mm along the height of the model. The bottom end of the steel spine was rigidly connected to a 406.4 mm (16") square (0.5" thick) steel base plate. The nominal building envelope included seven 3D-printed segments (made from ABSi) with recessed corners. The recessed corners allowed for the installation of different corner geometries (e.g., square, rounded, chamfer, fins). The corner geometry of Figure 29 was selected to follow the corner geometry of the benchmark 76-story prototype building in Yang et al. (2004), which consists of two chamfered and two square corners in plan. Adopting the same corner configuration would enable comparison and validation with previous studies that conducted experiments on the 76-story benchmark building (e.g., Lu et al. 2016). The corners with different geometries were manufactured using 15 pcf polyurethane foam (General Plastics #FR4515) and installed using 6mm × 30mm wooden dowel pins

(Bear Woods #MG-0630). Rubber gaskets were installed between adjacent envelope segments along the height of the model. The total mass of the specimen, excluding the base plate, was 21.0 kg.

The model is instrumented with fourteen accelerometers, which were mounted along the centerline of the aluminum diaphragms to measure accelerations in the local X- and Y-directions as depicted in Section A-A in Figure 29. Additionally, the four laser displacement sensors were mounted to two stanchions to capture deflections in the local X- and Y-directions at $z = 0.5H$ and $z = 0.97H$. A system of eight pretensioned steel cables were used to modify the model stiffness, which will be discussed in further detail in Chapter 5.3 and Chapter 6.1. The model and stanchions were installed on a turntable in the BLWT. The model was primarily evaluated at approach angles, α, of 0° and 45°. Dynamic similitude scaling parameters between the prototype (p) and the aeroelastic model (m) are summarized in Table 7.

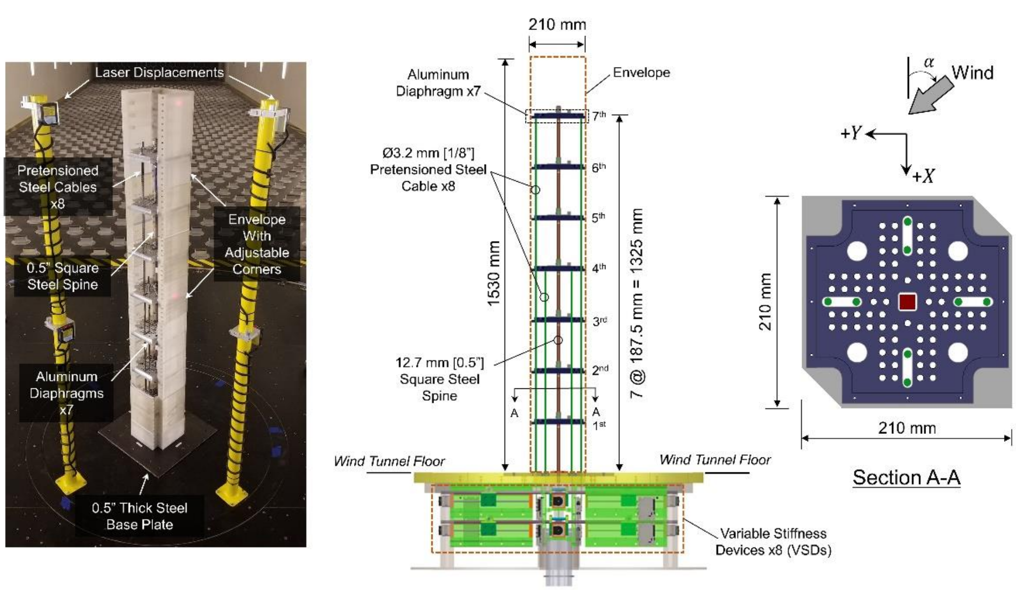

Figure 29. Multi-degree-of-freedom 1:200 aeroelastic tall building specimen with the VSDs installed.

Table 7. Dynamic similitude requirements for the aeroelastic specimen.

Scaling Parameter	Similarity Requirement	Scale
Length	L_m/L_p	$1/200$
Velocity	$U_m/U_p \ = \sqrt{L_m/L_p}$	$1/\sqrt{200}$
Time	$t_m/t_p \ = \sqrt{L_m/L_p}$	$1/\sqrt{200}$
Frequency	$n_m/n_p \ = \sqrt{L_p/L_m}$	$\sqrt{200}/1$
Displacement	L_m/L_p	$1/\sqrt{200}$
Mass	$\left(L_m/L_{fs}\right)^3$	$1/200^3$
Acceleration	$a_m = a_p$	$1:1$
Damping	$\zeta_m = \zeta_p$	$1:1$

5.2 Experimental equipment

Wind tunnel experiments with the aeroelastic, tall building model were conducted at the same University of Florida NHERI Experimental Facility as the rigid, low-rise building model as described in Chapter 3.4. The fans were operated at a constant RPM of either 225 RPM or 275 RPM depending on the optimization problem. The aeroelastic model building installed in the BLWT is shown in Figure 30. The response of the model was monitored using a series of accelerometers (PCB 333B50), laser displacement sensors (Panasonic HL-H125-A-C5), and miniature load cells (Omega LC201-200).

Figure 30. Aeroelastic model installed in the boundary layer wind tunnel, upwind view.

5.3 Tension calculation

Following a series of system identification experiments, it was observed that the lateral deflection at different locations along the height of the multi-degree-of-freedom building model could be empirically derived from the tension readings of the load cells. Opposite cable pairs were set to the same pretension force. Hence, if no external lateral force was acting on the specimen the differential tension would be zero. However, a differential tension would develop when the model was subjected to an external load, causing the tension of one cable to decrease while the tension of the other within the pair would increase the same amount. This differential tension was found to be approximately linearly proportional to the lateral building deflection; i.e., $\delta \propto \Delta T_{VSD}$; in the two principal sway modes. Measurements from the laser displacement sensors were used to calibrate and validate the load cells; under static deflection; using linear regression analysis. Figure 31 shows a representative displacement time series comparing the readings of the laser displacements with the equivalent load cell displacement values (after calibration) at heights of $z = 0.5H$ and $z = 0.97H$. A similar time series to the one in Figure 31 was used to calibrate the load cells. Very good agreement is observed between the laser readings and the calibrated load cell displacements in both the local X- and Y- directions under static loading conditions. However, preliminary BLWT experiments revealed excessive noise in the laser measurements under wind-induced dynamic loading, when compared to the load cell readings. After further investigation, these discrepancies were ascribed to signal contamination due to the dynamic response of the stanchions supporting the laser sensors (Figure 30). Therefore, the equivalent load cell displacement readings were used to assess the wind-induced response of the tall building specimen.

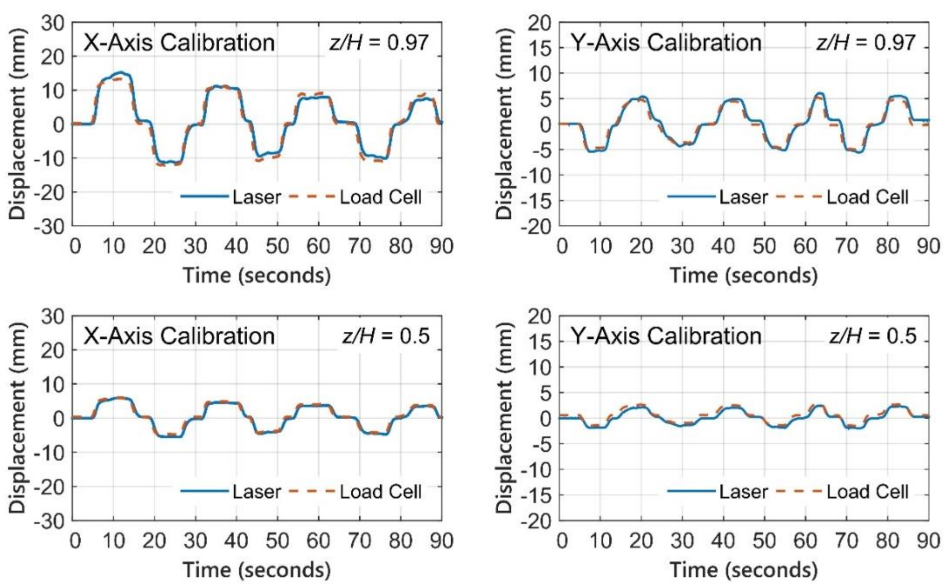

Figure 31. Equivalent load cell displacement calibrated to the laser displacement sensor (LDS) measurement at z = 0.5H and z = 0.97H (dimensions are in model-scale).

5.4 Kalman filtering

Kalman filtering (Kalman, 1960; Kalman & Bucy, 1961) was integrated into the CPS framework (see Figure 37) to estimate the full (i.e., 76 DOF) building response based on the dynamic properties of the prototype system (i.e., mass and stiffness matrix) and a limited number of acceleration and displacement measurements. This allowed for the evaluation of inter-story displacements between consecutive stories for all 76 floors.

5.5 Wind simulation

Simulation of upwind terrain was achieved via the Terraformer, a computer-controlled terrain generator located upwind of the BLWT testing section (as outlined in Chapter 3.7). For all experimental results the roughness grid was set to a uniform element height of h = 60 mm and the wide edge of each element was oriented perpendicular to the incident flow. This grid configuration was selected to simulate sparse suburban terrain exposure.

Figure 32a depicts normalized mean velocity and longitudinal turbulence intensity profiles for two wind velocities (i.e., hazard intensities). The measurements were collected at the BLWT testing section – in the absence of the building specimen – using Cobra probe sensors which were mounted to an automated gantry system. Each velocity (point) measurement was taken for 120 seconds at a sampling rate of 1250 Hz. The mean longitudinal wind velocity at 1.5 m (near the height of the specimen) was 3.5 m/s and 4.3 m/s for the two hazard intensities considered, which correspond to full-scale wind speeds of approximately 49.6 m/s and 60.88 m/s, respectively. The mean velocity profile data was fitted to the power-law profile, which is commonly used in wind engineering and can be expressed as

$$\frac{U_z}{U_{ref}} = \left(\frac{z}{z_{ref}}\right)^{\hat{\alpha}} \tag{17}$$

where U_z is the mean wind velocity at elevation z; $\hat{\alpha}$ is the power-law exponent (i.e., fitting parameter); U_{ref} is the reference mean wind velocity at elevation z_{ref} = 1.5 m above the tunnel floor. Power-law exponents of $\hat{\alpha}$ = 0.22 and 0.19 were found for U_{ref} = 3.5 and 4.3 m/s, respectively. According to ASCE 49-12 (2012), these power-law exponents represent sparse suburban terrain conditions (e.g., Exposure B). Figure 32b also includes the normalized longitudinal velocity spectra measured at 1.5 m. Very good agreement is observed between the measured fluctuating wind flow and the spectral model presented in Kaimal (1978) for the two reference wind velocities.

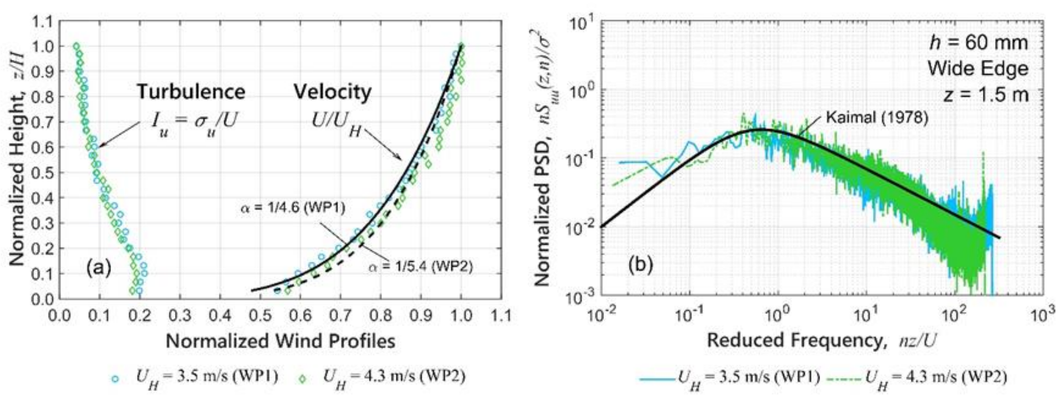

Figure 32. (a) Normalized mean longitudinal velocity and turbulence intensity profiles. (b) Longitudinal wind velocity spectra at z = 1.5 m.

5.6 Summary

In this chapter the development of the aeroelastic, tall building specimen and the experimental equipment used for BLWT testing of the specimen was described in detail. The experimental equipment implemented for the research of the model was subsequently provided. The details of the simulation of upwind sparse suburban terrain were presented. In addition, model-scale and full-scale displacements are derived from cable pair tension readings and the application of a Kalman filter. These displacements will form a portion of the basis of performance evaluation during optimization.

Chapter 6: CPS Setup for Dynamics Optimization

This chapter details the selection of the physically adjustable design variable and creation of a suitable actuation system for the control of the structural dynamics of the aeroelastic, tall building model. This is accomplished through the use of variable stiffness devices (VSDs) to adjust the model building stiffness. The control of the dynamic properties of the specimen through the VSDs are validated through initial system identification experiments. The framework for providing data and power for controlling the actuation system is described to thoroughly depict the communication between cyber and physical components in the CPS incorporating the aeroelastic model for optimizing dynamic properties.

6.1 Variable stiffness devices

Physical adjustment of the stiffness properties (i.e., modal frequencies) of the model was achieved through a system of eight 3.2 mm (1/8”) diameter steel cables, installed inside the model. The top ends of the cables were connected to the 4th or 7th diaphragms (Figure 29). The bottom end of each cable was connected to a 200 N miniature load cell (Omega LC201), located near the base of the model. The bottom of the load cell was fixed to a threaded rod, which was rigidly connected to the tip of a cantilever beam of a variable stiffness device (VSD); as shown in Figure 33. The length of the cantilever beam (d_{VSD} + b_c) was adjusted by driving a slider block along the length of the beam using a stepper motor coupled to a 300 mm captured lead screw. Encoders mounted to the back of the VSD stepper motors provided closed-loop feedback control to ensure the desired VSD cantilever length (i.e., d_{VSD}) was reached. All eight cables were pretensioned such that they remain in tension throughout testing; i.e., the cables will never "sag" when the model deflects laterally due to an external wind load.

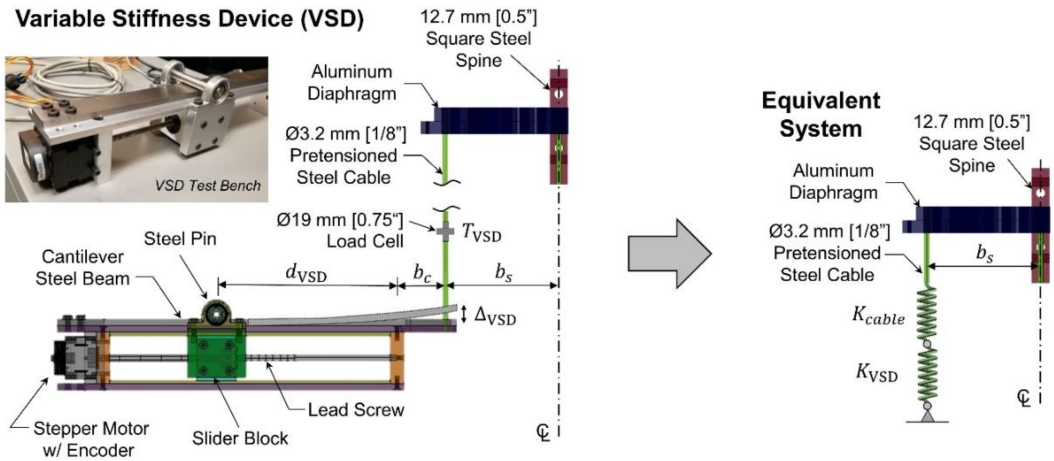

Figure 33. Physical (left) and equivalent (right) system of variable stiffness device (VSD) mechanism.

The equivalent (linear) stiffness of the steel cable ($K_{cable} = (AE/L)_{cable}$) and cantilever beam is illustrated in Figure 33. Assuming Euler-Bernoulli beam behavior, the equivalent stiffness of the cantilever beam is

$$K_{VSD} = \frac{E w_b h_b^3}{4(d_{VSD} + b_c)^3} \tag{18}$$

In Equation (18), E is the Young's modulus of the cantilever beam, and w_b and h_b are the cross section dimensions of the cantilever beam; i.e., width and depth, respectively. From Equation (18), it can be deduced that K_{VSD} is inversely proportional to d_{VSD}^3.

6.2 System identification

Initial system identification experiments were performed to validate the effect of the VSDs on the dynamic properties of the specimen. Figure 34a depicts the theoretical (FEM) and estimated 1st mode natural frequencies of the tall building model for a range of cantilever lengths (d_{VSD}). For this initial validation test, all eight VSDs were set to the same cantilever length (although each VSD is controlled individually). The theoretical curve was constructed by performing (numerical) modal analysis on the FEM model, while the experimental frequencies were obtained from the first peak of the acceleration power spectra measured at the 7th diaphragm (z = 0.87H). Reasonably good agreement is observed between the numerical and experimental results. Figure 34b also shows free vibration experiments in the X-direction for the VSD configuration d_{VSD} = 30 mm, which produced a 1st mode full scale natural frequency of approximately 0.183 Hz. Very similar natural frequencies were also observed in the Y-direction. Damping ratios in the X- and Y- directions ranged from ζ = 2.4%-3.5% and were estimated using the log decrement method. The range of ζ values is a result of changes in the VSD configuration, which alters the natural frequency of the model. These estimated damping ratios are larger than the value of 1% selected for the full-scale benchmark building (Yang et al., 2004). Attempts were made to reduce the structural damping of the physical specimen as much as possible. However, the damping values were considered acceptable to evaluate the proposed CPS framework.

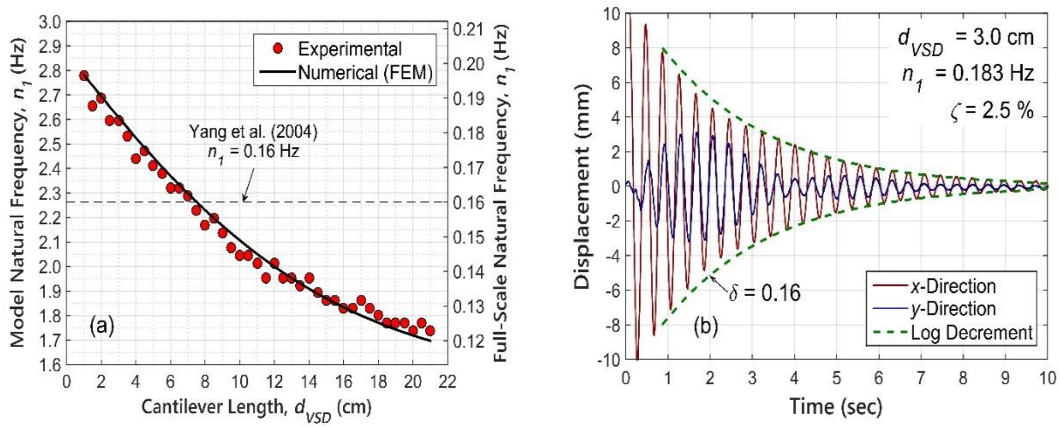

Figure 34. (a) Fundamental mode natural frequency of aeroelastic specimen in the X-direction for a range of d_{VSD}. (b) Representative free vibration time series in the X-direction for d_{VSD} = 30 mm (dimensions are in model-scale).

6.3 Cyber-physical setup

A detailed schematic of the actuation, sensor, and computer hardware setup in the boundary layer wind tunnel (BLWT) for the aeroelastic testing considering the VSDs is illustrated in Figure 35 respectively. For the aeroelastic testing considering the VSDs, computational hardware included an instrument and a coordinating computer, both located in the BLWT control room. The coordinating computer executed the main MATLAB script which would call a Python script to send commands to the instrumentation computer through a local-area network. These commands would set testing parameters (e.g., test duration or sampling rate) and initialize the data collection. The instrumentation computer would primarily collect sensor data measurements using LabVIEW software. For the model sensors, 14 accelerometers were connected to National Instruments (NI) vibration input modules (NI-9234), while voltage input modules (NI-9205) and signal conditioners (PCB 8162-011A) were used for the load cells. The NI modules were housed in an 8-slot USB NI

CompactDAQ chassis (cDAQ-9178) and the signals were directly sent to the instrument computer through USB. Sensor data from the accelerometers and load cells was synchronized and sampled at 500 Hz. Real-time measurements from all the sensors were monitored on the instrumentation computer and all data was transferred to the NHERI DesignSafe-CI Data Depot repository (Rathje et al., 2017) automatically in near real-time (within 240 seconds of data collection).

Figure 35 shows the VSD stepper motors located below the model, each equipped with a motor controller (Nanotec SMCI36). The controllers communicate with a Raspberry Pi 3 which receives commands from a Python script running on the coordinating computer to adjust the cantilever length of each VSD (i.e., d_{VSD}; see Figure 33).

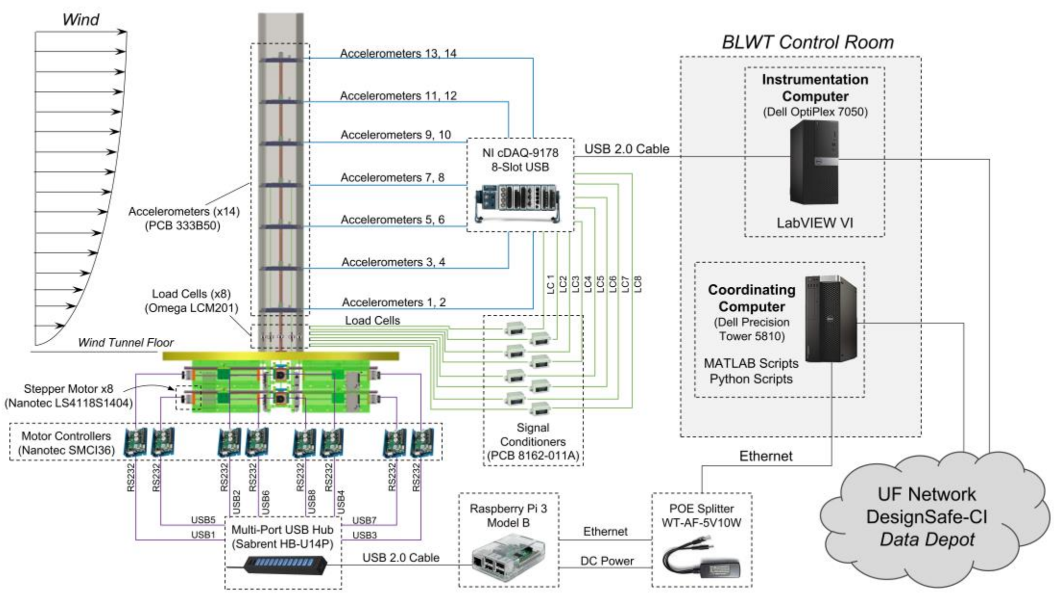

Figure 35. Schematic of actuation, sensor, and computer hardware for CPS aeroelastic experiments in the BLWT considering VSDs.

6.4 Summary

This chapter describes the development of the aeroelastic, tall building specimen required for optimization of structural dynamics within the CPS. An actuation system comprised of VSDs is used to physically adjust model building stiffness and modify structural dynamics. Control of structural dynamics is validated through initial identification experiments. The communication of both data and power within the CPS incorporating the aeroelastic model is provided to provide a better understanding of the communication between cyber and physical components.

Chapter 7: Aeroelastic Testing and Dynamics Optimization

This chapter details the testing of the aeroelastic, tall building model with the VSDs comprised of preliminary results in the form of a test matrix and then the results and analysis of stochastic optimization problems presented subsequently. The test matrix for the VSD testing includes a discrete set of wind approach angles for a comprehensive set of VSD cantilever lengths.

7.1 Initial test matrix for VSDs

A test matrix for the VSD testing was obtained by testing wind approach angles of 0º and 45º for two different corner geometries (Figure 36).

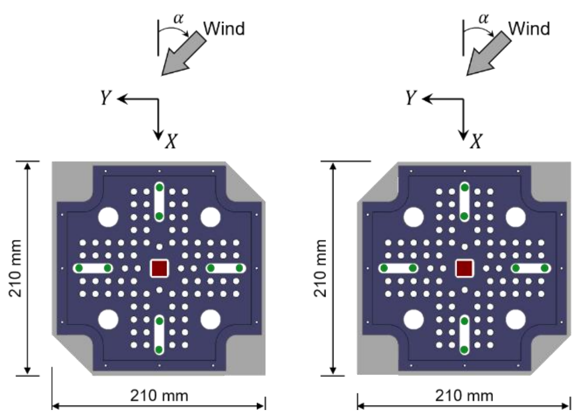

Figure 36. Corner geometries for VSD test matrix.

The different model configurations were created by exchanging the square corners for chamfered corners and vice-versa. This was performed to position the stanchions on the leeward side of the building for an approach angle of 45º to minimize blockage effects. VSD cantilever lengths from 10 mm to 220 mm were tested for 60 seconds for each wind approach angle at increments of 10 mm for each corner geometry. The test matrix served to validate that all of the accelerometers and laser displacement sensors were returning reasonable data as expected. In particular, because the building was symmetric for 0°, it was straightforward to identify any inaccuracies or inconsistencies with sensors or model construction.

The purpose of the test matrix was to obtain training data to develop a better understanding of the dynamic response of the building for varying VSD configurations. This allowed for the development of realistic objective functions for the optimization of building performance in consideration of the VSD configuration.

7.2 CPS framework for stiffness optimization with VSDs

7.2.1 CPS stiffness optimization problem

The main objective for most single-objective optimization problems for lateral stiffness design of tall buildings is minimization of structural weight (Chan et al., 2009; Spence & Kareem, 2014; Huang et al., 2015) since it typically renders a savings in material and construction cost. Weight minimization is often constrained by serviceability and/or strength requirements to ensure adequate structural performance during moderate and extreme loading events. Satisfying these constraints often warrants an increase in the lateral building stiffness, consequently leading to a heavier structural system than desired. Therefore, numerical optimization methods are commonly applied to automate the design and minimize the stiffness of the lateral structural system while meeting serviceability and strength constraints. In the case of tall and slender structures (i.e., large height-to-width ratio), serviceability (e.g., floor acceleration, building drift) constraints often control the optimum design over strength requirements (e.g., Fernández-Cabán & Masters, 2018), where the estimated (or measured) building response is compared against user-specified, or code-based, target response thresholds (or limits). These limits can be explicitly formulated in a deterministic or probabilistic manner (e.g., Spence & Gioffrè, 2012). In this study, the RMS horizontal acceleration, $a_{L,RMS}$, from Equation (13) is selected as the serviceability criteria for occupant comfort for the optimization process, since it experimentally provides a more repeatable statistical measure of acceleration. Nevertheless, measured peak accelerations are also evaluated and compared to peak threshold during post-processing.

For most tall buildings, the dominant modal frequency is commonly used as an indicator of the overall lateral building stiffness. In the proposed CPS stiffness optimization framework, the objective is to minimize the natural frequency (i.e., stiffness) of the building specimen, while satisfying serviceability requirements related to occupant comfort, overall and inter-story drift criteria. In other words, finding the most flexible VSD configuration that meets acceleration and deflection limits. Mathematically, this can be formulated as follows:

Find a solution, $\mathbf{x} = \{x_1, x_2, x_3, x_4\}$, to the problem

Maximize $f(\mathbf{x}) = x_1 + x_2 + x_3 + x_4$

subject to the constraints

$$g_i^a(\mathbf{x}) = \frac{a_m}{\tilde{a}} - 1 \leq 0 \quad \text{for} \quad i = 1, \dots, ns$$

$$x_{min} \leq x_j \leq x_{max} \quad j = 1, \dots, 4$$

or

$$g_k^{ID}(\mathbf{x}) = \frac{\delta_k - \delta_{k-1}}{\delta_{allw}} - 1 \leq 0 \quad \text{for} \quad k = 1, \dots, ns$$

$$g^{OD}(\mathbf{x}) = \Delta/\Delta_{allw} - 1 \leq 0$$

$$x_{min} \leq x_j \leq x_{max} \quad j = 1, \ldots, 4$$

where $\mathbf{x}$ is the design variable vector representing the cantilever lengths (i.e., d_{VSD}) of the four VSD pairs; $f(\mathbf{x})$ is the constrained objective function; a_m is the measured floor acceleration; $\tilde{a}$ is the target acceleration threshold; where $\delta_k - \delta_{k-1}$ is the relative lateral displacement of adjacent stories; δ_{allw} is the allowable inter-story drift limit; ns is the total number of stories; Δ is the lateral building deflection at the top story; Δ_{allw} is the allowable overall deflection limit. The objective function is chosen as the sum of the cantilever lengths of the four VSD pairs. The optimization problem is formulated as a function maximization problem since the cantilever lengths are inversely proportional to the natural frequency of the tall building specimen; i.e., increasing d_{VSD} decreases the stiffness (Figure 34).

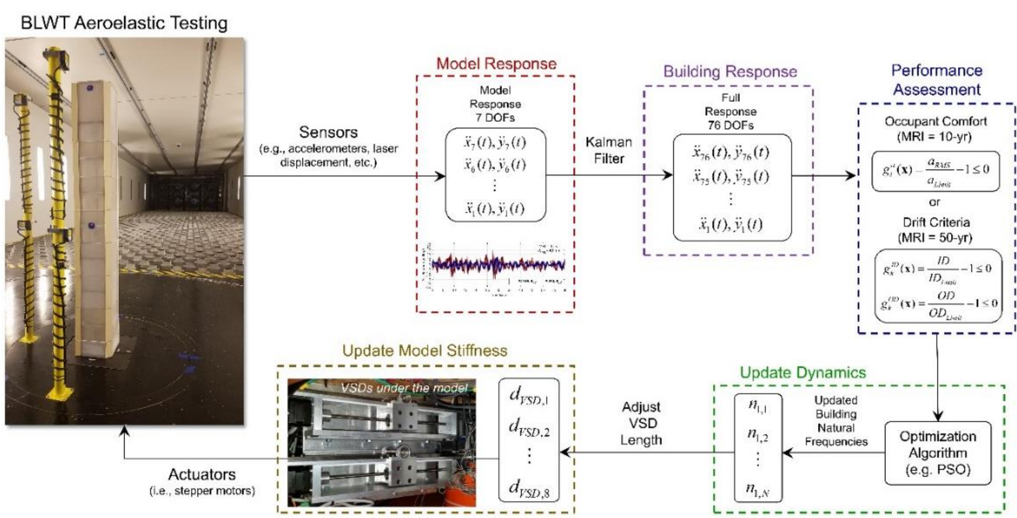

Figure 37. Cyber-physical framework for tall building dynamics optimization in the wind tunnel.

The constrained objective function $f(\mathbf{x})$ was transformed into an unconstrained one using a penalty function approach as follows:

$$\varphi(\mathbf{x}) = \frac{f(\mathbf{x})}{1 + pC(\mathbf{x})} \tag{19}$$

$$C(\mathbf{x}) = \sum_{i=1}^{nd} g_i^a(\mathbf{x}) \quad \text{for } i = 1, \dots, nd \tag{20}$$

$$C(\mathbf{x}) = \sum_{k=1}^{ns} g_k^{ID}(\mathbf{x}) + g^{OD}(\mathbf{x}) \quad \text{for } k = 1, \dots, ns \tag{21}$$

in which $\varphi(\mathbf{x})$ is the unconstrained objective function; p is a penalty coefficient and $C(\mathbf{x})$ is the penalty function.

7.2.2 CPS stiffness optimization algorithm

The generation of new candidate designs within the CPS framework is driven by a numerical optimization algorithm. The algorithm evaluates the performance of each candidate and updates their physical attributes (e.g., stiffness) until a convergence criterion is satisfied. In general, the CPS framework can be built around virtually any stochastic or non-stochastic (e.g., gradient-based) optimization algorithm. The user can select the most suitable optimization strategy after considering the nature and complexity of optimization problem; e.g., size of the search space, number of objectives, etc. Particularly, metaheuristic search algorithms have gained considerable attention in recent years due to their practicality and efficiency in finding near-optimum solution to complex (e.g., highly non-linear) engineering problems in an acceptable timescale. These algorithms apply intelligent heuristic search strategies to efficiently investigate, via randomization, the search space of candidate designs. The main components of metaheuristic algorithms are diversification (or exploration) and intensification (or exploitation). To some extent, all metaheuristic algorithms use some compromise between the local search (i.e., exploitation) and global exploration of the search space (Gandomi et al., 2013).

This study employs a recently developed explore-then-exploit (ETE) metaheuristic optimization strategy (Fernández-Cabán & Masters, 2018) into the CPS framework. The algorithm hybridizes two well-established metaheuristic strategies, namely particle swarm optimization (PSO) and Big Bang-Big Crunch. PSO is a metaheuristic technique which mimics the social behavior of organisms such as bird flocking and fish schooling (Kennedy & Eberhart, 1995) and has proven effective in the global investigation (i.e., exploration) of large design domains. The Big Bang-Big Crunch algorithm was originally developed by Erol and Eksin (2006) and was inspired by one the theories of evolution of the universe. The generation of new candidate designs is performed using the following ETE updating scheme:

$$\mathbf{x}_i^{k+1} = \text{round}\left[\theta_k \mathbf{G}^k + (1-\theta_k)\mathbf{P}_i^k\right] + \mathbf{d}_i \quad \text{for} \quad i = 1, \dots, N \tag{22}$$

where x_i^{k+1} is the position vector of particle i at iteration $k+1$ rounded to the nearest integer; G^k is the position of the best solution found among all candidates up to iteration k (i.e., global best); P_i^k is the best position found by particle i up to iteration k (i.e., particle best); θ_k is a control parameter that linearly increases over a user-specified number of generations to control the relative influence of P_i^k and G^k; d_i is a normal distribution operator from the Big Bang-Big Crunch algorithm (Erol & Eksin, 2006). In this study, d_i is defined (rounded to the nearest integer) as:

$$\mathbf{d}_i = \text{round}\left[\alpha r_i \left(\frac{\mathbf{x}_{max} - \mathbf{x}_{min}}{k}\right)\right] \quad i = 1, \dots, N \tag{23}$$

where r_i is a random number from a standard normal distribution; α is a parameter for controlling the size of the search space; x_{max} and x_{min} are the position vectors of the upper and lower bounds of each design variable, respectively. After each iteration, θ_k is adjusted to increase the influence of the global best solution (G^k) on the swarm, thus effecting a gradual transition from exploration to exploitation of the search space. In this study, θ_k is linearly increased after each iteration k following:

$$\theta_k = \left(\frac{\theta_f - \theta_i}{\beta k_{max} - 1}\right)(k-1) + \theta_i \tag{24}$$

where k_{max} is the maximum number of iterations; β is a parameter which defines the iteration when θ_k will transition from a linear variation to a final constant value; θ_i and θ_f are the initial and final values, respectively.

7.3 Stiffness optimization results and analysis

A series of CPS optimization runs were performed to investigate the efficacy of the proposed CPS framework for optimizing the dynamics of a tall building in the wind tunnel. The objective for all boundary layer wind tunnel (BLWT) runs was to seek the optimum design that would minimize the building natural frequency—i.e., maximize d_{VSD}—while satisfying multiple acceleration or deflection constraints. Since different return periods (i.e., mean recurrence intervals (MRIs)) must be used to evaluate criteria for occupant comfort and drift, CPS optimization runs were performed for two reference wind velocities. First, an equivalent 10-yr MRI (U_H = 3.5 m/s in the BLWT) windstorm event was chosen to address acceleration criteria for occupant comfort, where the acceleration threshold defined in Equation (13) was compared to the (measured) resultant root-mean-square (RMS) accelerations $a_{R,\mathrm{RMS}}$ considering the translational motion in the orthogonal directions.

$$a_{R,\mathrm{RMS}} = \sqrt{{a_{X,\mathrm{RMS}}}^2 + {a_{Y,\mathrm{RMS}}}^2} \tag{25}$$

Second, CPS experiments were repeated at a higher reference wind velocity to simulate a 50-yr MRI (U_H = 4.3 m/s) to assess overall building sway and inter-story drift constraints in the X and Y direction. In these experiments, Kalman filtering (Kalman, 1960; Kalman & Bucy, 1961) was integrated into the CPS framework (see Figure 37) to estimate the full (i.e., 76 DOF) building response based on the dynamic properties of the prototype system (i.e., mass and stiffness matrix) and a limited number of acceleration and displacement measurements. This allowed evaluation of inter-story displacement between consecutive stories for all 76 floors.

Table 8 summarizes the BLWT testing parameters and constraints for five independent CPS optimization runs. The runs were tested for a 0º wind direction (Figure 29). Different test durations T_d were selected to investigate the effect of the record length on the final solution. As an initial assessment of the CPS framework, only one design variable was chosen for all runs. That is, all eight VSDs were set to the same length for each candidate design tested in the BLWT. Parameters for the explore-then-exploit (ETE) optimization algorithm were chosen as N = 10, k_{max} = 8, θ_i = 0.3, θ_f = 0.8, α = 0.6, β = 1.0, x_{max} = 210 mm, x_{min} = 10 mm, and p = 30. The population size (N) and the maximum number of iterations (k_{max}) were selected considering the time limits of experiments in the BLWT. The total time required to perform a single CPS optimization run is approximately $Nk_{max}(t_d + t_{VSD} + t_w)$, where t_d is the BLWT tests duration (e.g., 60 sec), t_{VSD} is the time required to reconfigure all eight VSDs (~180 seconds), and t_w is the time it takes to rotate the turntable to a different wind angle; t_w = 0 for this study.

Table 8. Hazard intensity and performance criteria for six independent CPS optimization runs.

CPS Optimization Run	MRI (yr)	Wind Velocity, U_H		Duration, T_d		Serviceability Limit States
		Full Scale (m/s)	BLWT (m/s)	Full Scale (min)	BLWT (sec)	
CPS-OC-1	10	49.5	3.5	14	60	Resultant RMS acceleration (Equation (13))
CPS-OC-2	10	49.5	3.5	14	60	
CPS-OC-3	10	49.5	3.5	42	180	
CPS-DR-1	50	60.8	4.3	14	60	Overall and inter-story drift in the X- and Y-direction
CPS-DR-2	50	60.8	4.3	14	60	

7.3.1 Occupant comfort (MRI = 10-yr)

Figure 38 illustrates iteration histories from three independent CPS optimization runs for occupant comfort. The whiskers at each iteration represent d_{VSD} (or frequency n_1) statistics (i.e., mean, maximum, minimum, and 25th and 75th quantiles) from a population of N = 10 candidate designs (called "particles" in PSO) tested. In Figure 38, the 1st mode natural frequencies on the left vertical axis of each subplot were obtained from modal analysis using the numerical FEM model (Figure 34a), which provides a continuous function of n_1 for every d_{VSD}. The three subplots display similar convergence behavior. Early iterations show a broad distribution of d_{VSD} lengths, enabling exploration of the design domain. At late stages of the optimization process, the particles congregate and exploit the region around the global best solution. The final (full-scale) natural frequency for the three runs were 0.173, 0.168, and 0.176 Hz, respectively. These frequencies are slightly higher than that of the benchmark building (Yang et al., 2004; n_1 = 0.16 Hz).

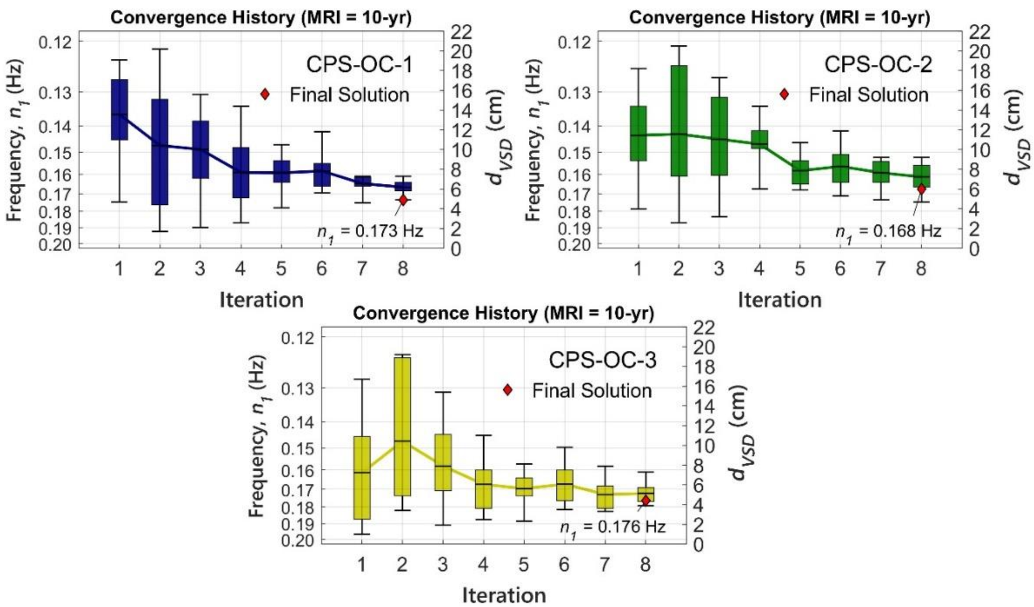

Figure 38. Convergence history from three independent CPS optimization runs (MRI = 10-yr) (full-scale n_1).

Across, along, and resultant RMS acceleration response at seven measurement heights are depicted in Figure 39 for the final solution of run CPS-OC-3. Although acceleration criteria were evaluated at the seven heights (i.e., 7 acceleration constraints), it was anticipated that the highest measurement height (z = 0.87H) would control the optimum design. Further, it is evident from Figure 39 that the across-wind response contribution to the resultant is consistently greater than the along-wind acceleration. The higher across-wind response can be attributed to vortex shedding, where n_1 is near the shedding frequency of the vortices. The Strouhal number relates the shedding frequency to the flow velocity and the characteristic dimension of the bluff body and is defined as $St = n_s B / U_H$; where n_s and B are the shedding frequency and the width of the building normal to the mean flow, respectively. Strouhal number values have been reported to be in the range 0.12–0.15 for a square building with chamfer corners (e.g., Tanaka et al. 2013). Assuming St = 0.14, then n_s~ (0.14)(49.5 m/s)/(42 m) = 0.165 Hz. This value is very close to the final natural frequencies of the building for the three CPS runs. The larger across-wind acceleration can also be observed in Figure 40, which shows acceleration time histories at z = 0.87H for CPS-OC-3.

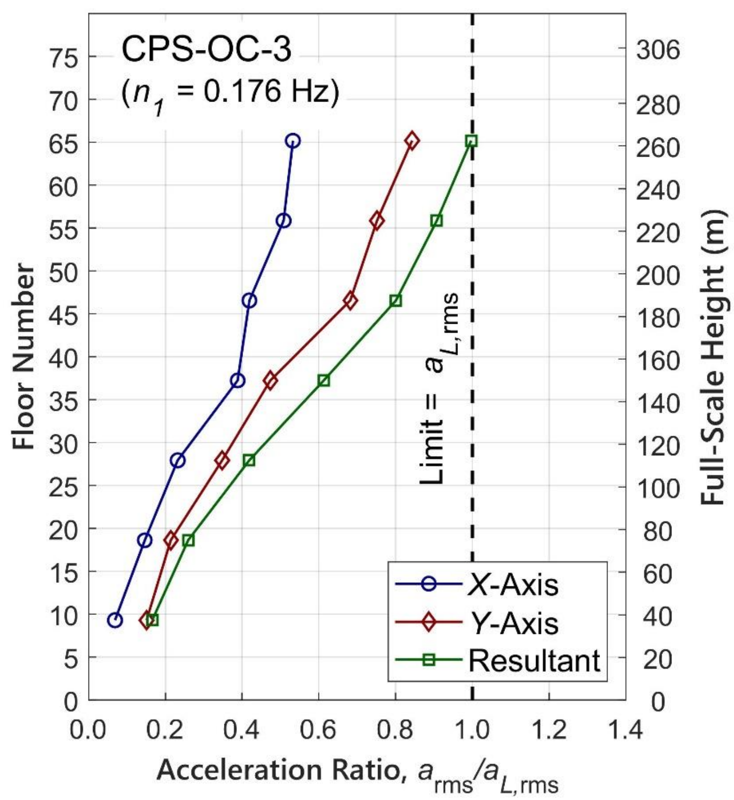

Figure 39. Final horizontal RMS acceleration ratios from of run CPS-OC-3 (full-scale n_1 = 0.176 Hz).

Table 9 reports natural frequencies and acceleration ratios obtained at different stages of the CPS optimization process for run CPS-OC-3. Means and standard deviations represent statistics of the N = 10 candidate designs evaluated at each iteration. Larger standard deviations of frequency and acceleration ratio occur at early iterations, which indicates a greater spread of candidate designs to promote exploration of the search space. The candidate designs congregate at the late stages of the optimization process, where standard deviations of frequency and acceleration reach values of 0.005 Hz and 0.069 at iteration 8, respectively. Table 10 includes the acceleration ratios at z/H = 0.87 for the three runs. Target RMS accelerations were obtained from Equation (13) based on the (full-scale) natural frequency of the building and MRI = 10-yr. The best design for run CPS-OC-3 achieved an acceleration ratio of 0.997 at z = 0.87H, while runs CPS-OC-1 and CPS-OC-2 reported minor constraint violations, with ratios of 1.023 and 1.013, respectively. Slight constraint violations are not uncommon when using the penalty functions as the constraint handling approach. Experimenting with different penalty coefficient (p) values is one method for mitigating this problem (Yeniay, 2005). Nevertheless, constraint violations in CPS-OC-1 and CPS-OC-2 are considered negligible.

Table 9. Iteration history of natural frequency and acceleration ratio for CPS optimization run CPS-OC-3 (Candidate designs tested per iteration, N = 10).

Iteration	n_1 (Hz)		$\frac{a_{R,\mathrm{RMS}}}{a_{L,\mathrm{RMS}}}$ at z = 0.87H	
	Mean	Standard Deviation	Mean	Standard Deviation
1	0.165	0.025	0.959	0.203
2	0.152	0.023	1.052	0.262
3	0.160	0.018	0.944	0.117
4	0.168	0.014	0.945	0.141
5	0.170	0.009	0.930	0.078
6	0.168	0.010	0.984	0.092
7	0.173	0.008	0.868	0.100
8	0.172	0.005	0.920	0.069

Table 10. Final acceleration response from three independent CPS optimization runs (MRI = 10-yr).

CPS Optimization Run	d_{VSD} (mm)	n_1 (Hz)	RMS Acceleration at $z = 0.87H$ (milli-g)				$\frac{a_{R,\mathrm{RMS}}}{a_{L,\mathrm{RMS}}}$
			Along $a_{X,\mathrm{RMS}}$	Across $a_{Y,\mathrm{RMS}}$	Resultant $a_{R,\mathrm{RMS}}$	Target $a_{L,\mathrm{RMS}}$	
CPS-OC-1	49	0.173	3.18	5.46	6.32	6.18	1.023
CPS-OC-2	60	0.168	3.14	5.28	6.14	6.06	1.013
CPS-OC-3	44	0.176	3.28	5.19	6.14	6.16	0.997

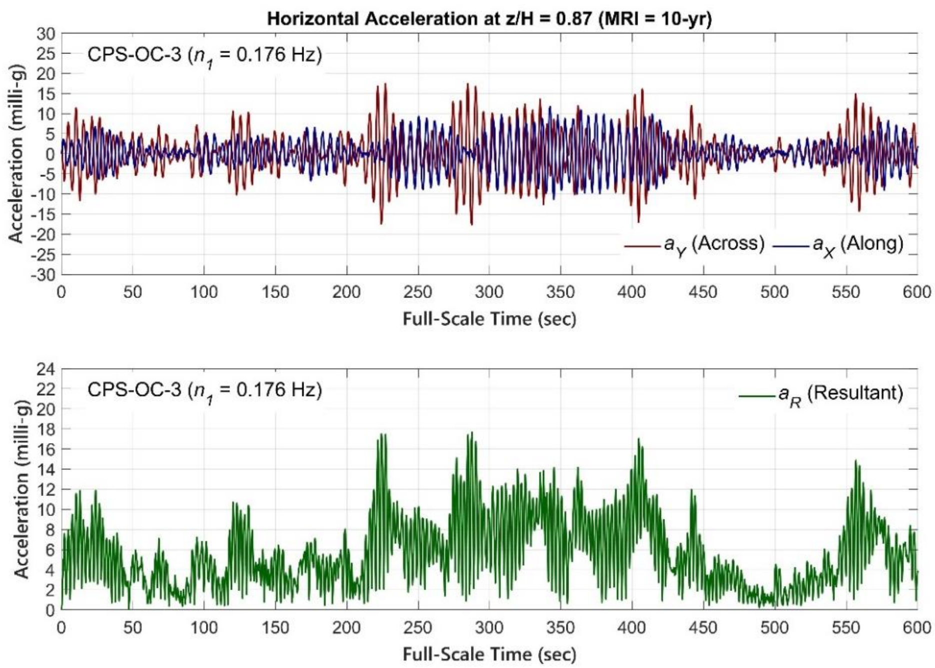

Figure 40. Time histories of along and across (top), and resultant (bottom) acceleration at $z = 0.87H$ from run CPS-OC-3 (full-scale n_1 = 0.176 Hz and model-scale accelerations).

<u>7.3.2 Overall and inter-story drift (MRI = 50-yr)</u>

Two independent CPS optimization runs, namely CPS-DR-1 and CPS-DR-2, were executed at a higher wind velocity (U_H = 4.3 m/s in the BLWT) to evaluate drift criteria; i.e., overall top building sway and inter-story drift. A total of 152 drift constraints were imposed on the optimization problem, which included 75 inter-story and one top building drift in the X and Y direction. The convergence histories of the two runs are presented in Figure 41. As previously mentioned, whiskers at each iteration denote d_{VSD} statistics from N = 10 candidate designs tested. Although noticeable distinctions can be made in the progression toward the final solution, the two runs reached nearly identical optimum results. Run CPS-DR-1 reached a final full-scale frequency of 0.180 Hz, while n_1 = 0.179 Hz for CPS-DR-2. These frequencies are somewhat larger than the final solutions found for MRI = 10-yr.

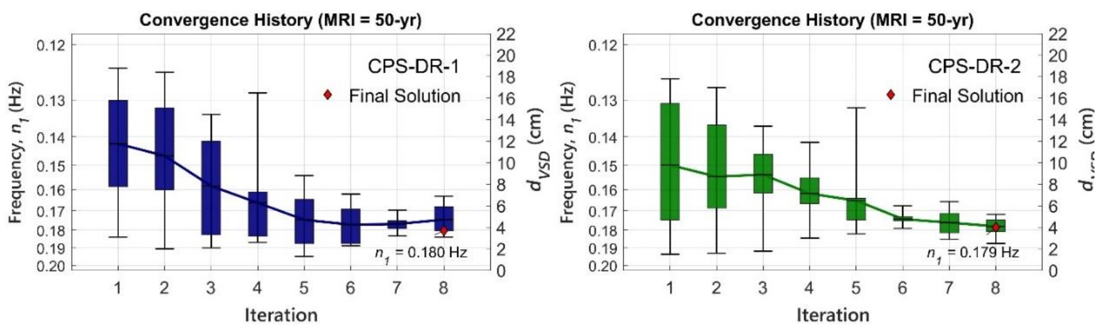

Figure 41. Convergence history from two independent CPS optimization runs for drift criteria (MRI = 50-yr) (full-scale n_1).

Figure 42 illustrates peak top and inter-story drift ratios for the final solution of CPS-DR-1. It is evident from Figure 42b that inter-story constraints in the across wind (Y) direction are controlling the optimal solution for the chosen hazard intensity and wind direction (0º). Inter-story drift ratios above floor ~60 are near (or at) the drift limit (h/400), while ratios in the along-wind (X) direction comfortably meet inter-story drift requirements. Further, top deflection limit (H/500) are easily satisfied in both X and Y, with maximum ratios of 0.44 and 0.76, respectively. Drift ratios like the one shown in Figure 42 were also observed in the final solution of run CPS-DR-2. Table 11 summarizes natural frequencies and across wind (Y) inter-story drift ratios of the top floors during different stages of the CPS optimization process of run CPS-DR-1. Maximum overall and inter-story drift for both runs are reported in Table 12, Table 13Table 14, and Table 14.

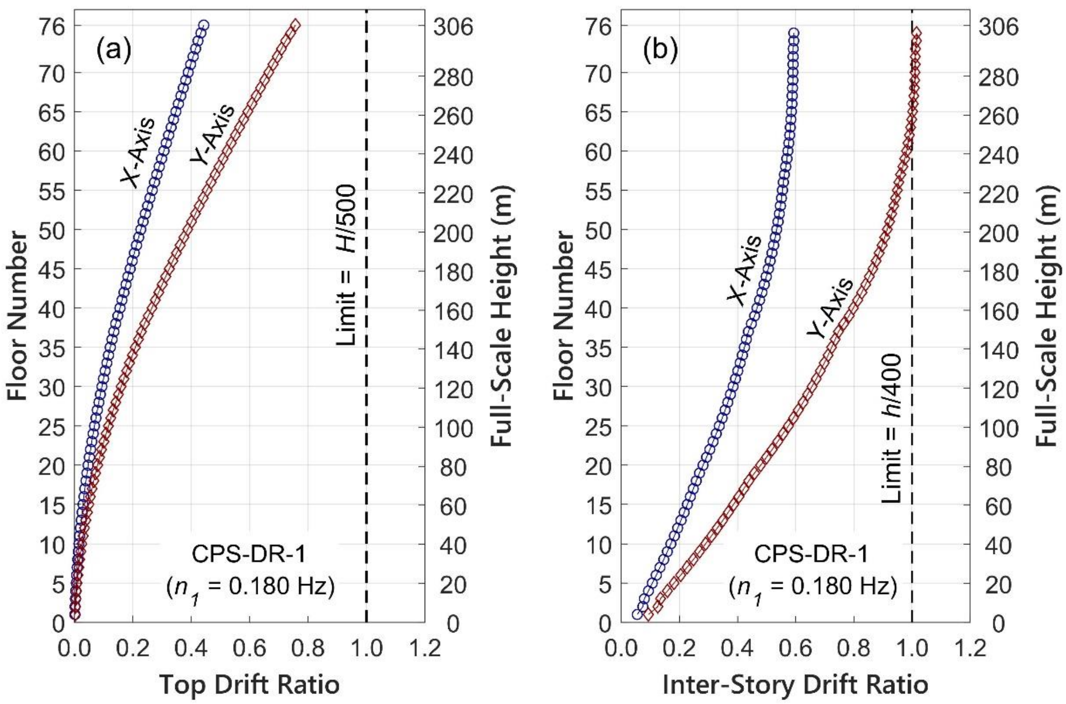

Figure 42. (a) Top building drift ratios and (b) inter-story drift ratios for final solution of run CPS-DR-1 (full-scale n_1 = 0.180 Hz).

Across wind displacement time histories (at z = 0.97H and z = 0.5H; 74$^{\text{th}}$ and 38$^{\text{th}}$ floors, respectively) for the final solution of CPS-DR-1 are shown in Figure 43. Displacements are presented in equivalent full-scale dimensions. Good agreement is observed between the measured and estimated displacement at both Y measurement locations, although small discrepancies are noticeable in some local peak values.

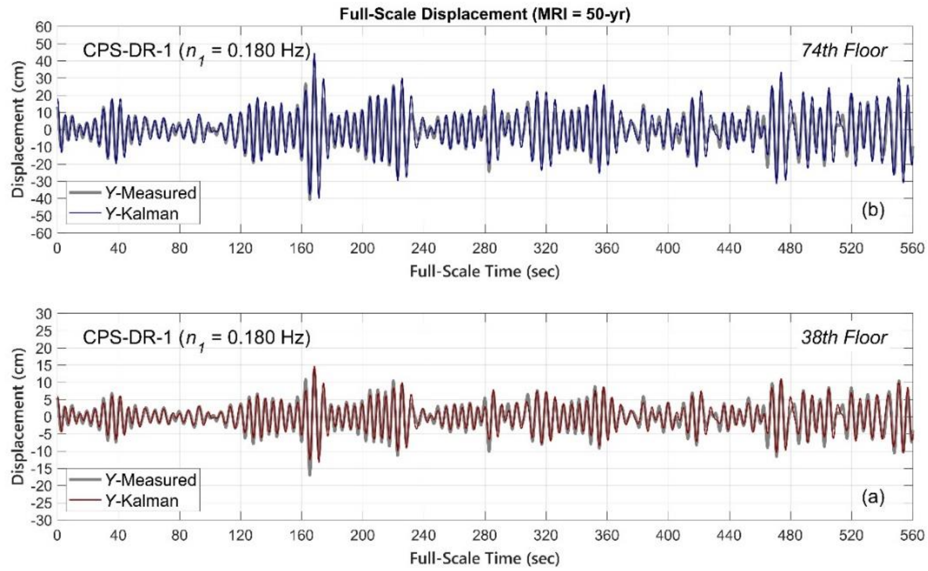

Figure 43. Equivalent full-scale across wind displacement time histories at floors (a) 38 and (b) 74 from final solution of run CPS-DR-1 (full-scale n_1 = 0.180 Hz and model-scale displacements).

Table 11. Iteration history of natural frequency and across (Y) wind inter-story drift ratio between top floors (75th and 76th floors) for CPS-DR-1 (Candidate designs tested per iteration, N = 10).

Iteration	Full-Scale n_1 (Hz)		Peak Inter-story Y-Drift Ratio (ID_Y/ID_L)	
	Mean	Standard Deviation	Mean	Standard Deviation
1	0.146	0.022	2.287	1.035
2	0.150	0.021	1.884	0.779
3	0.161	0.021	1.685	0.861
4	0.168	0.019	1.224	0.714
5	0.175	0.014	1.240	0.731
6	0.177	0.009	0.991	0.329
7	0.177	0.004	0.998	0.287
8	0.175	0.007	0.931	0.302

Table 12. Estimated and measured lateral building drift ratios in X for the final solution of runs CPS-DR-1 and CPS-DR-2.

Story	z/H	Peak Overall X-Drift Ratio (OD_x/OD_L)			
		CPS-DR-1		CPS-DR-2	
		Kalman	Measured	Kalman	Measured
10	0.13	0.01		0.01	

30	0.39	0.09		0.08	
38	0.50	0.14	0.13	0.13	0.14
50	0.66	0.23		0.20	
74	0.97	0.42	0.43	0.38	0.40
76	1.00	0.44		0.40	

Table 13. Estimated and measured lateral building drift ratios in Y for the final solution of runs CPS-DR-1 and CPS-DR-2.

Story	z/H	Peak Overall Y-Drift Ratio (OD_y/OD_L)			
		CPS-DR-1		CPS-DR-2	
		Kalman	Measured	Kalman	Measured
10	0.13	0.02		0.02	
30	0.39	0.16		0.16	
38	0.50	0.24	0.28	0.24	0.26
50	0.66	0.39		0.39	
74	0.97	0.72	0.66	0.72	0.62
76	1.00	0.76		0.75	

Table 14. Estimated peak inter-story drift ratios for the final solution of runs CPS-DR-1 and CPS-DR-2.

Stories	Peak Inter-story X-Drift Ratio (ID_X/ID_L)		Peak Inter-story Y-Drift Ratio (ID_Y/ID_L)	
	CPS-DR-1	CPS-DR-2	CPS-DR-1	CPS-DR-2
9-10	0.16	0.14	0.27	0.27
29-30	0.38	0.34	0.64	0.64
37-38	0.44	0.39	0.75	0.74
49-50	0.53	0.48	0.91	0.90
73-74	0.59	0.53	1.01	1.00
75-76	0.59	0.53	1.02	1.01

7.3.3 Discussion of stiffness optimization

Results from BLWT experiments validate the effectiveness of the proposed CPS optimization framework for—autonomously—optimizing the dynamics of a tall building in a wind tunnel, while satisfying user-specified serviceability performance criteria. Integration of an instrumented multi-degree-of-freedom aeroelastic specimen into the CPS loop enabled direct measurement and assessment of building response. Further, the stochastic optimization algorithms efficiently navigated candidate designs toward the global optimum. In the current study, CPS optimization runs for different return periods were performed to assess occupant comfort and drift criteria independently. Consequently, different optimal solutions (i.e., frequencies) may be reached depending on the serviceability criteria evaluated. In this case, the designer may select the higher natural frequency from the two serviceability criteria. For the building and testing parameters (e.g., wind direction) considered in this study, the CPS optimization runs assessing drift criteria produced higher optimal frequencies. In particular, inter-story drift in the across-wind (Y) direction controlled the optimum design of these runs.

As an initial step, the bulk of CPS runs were restricted to a single design variable in which all eight VSDs were set to the same distance (i.e., d_{VSD}). However, in principle, each VSD pair may be given a unique d_{VSD}, thus generating up to four design variables and enabling exploration of a larger design domain. For instance, the VSDs may be configured in a manner to achieve different natural frequencies in the two principal sway directions (X and Y). This is illustrated in Figure 44, which presents results from an additional CPS optimization run for two design variables. That is, VSDs pairs in the X- and Y-directions were set to cantilever lengths $d_{VSD,X}$ and $d_{VSD,Y}$, respectively. The global best solution after 10 iterations (right subplot) was $d_{VSD,X}$ = 6.7 cm and $d_{VSD,Y}$ = 7.5 cm, which correspond to full-scale natural frequencies of 0.164 Hz and 0.160 Hz, respectively. Both frequencies are slightly lower that the final solutions shown in Figure 38; where the same frequency was enforced in the X- and Y-directions. Slightly different frequencies in the two orthogonal directions could reduce the interaction (coupling) between the two fundamental (sway) modes.

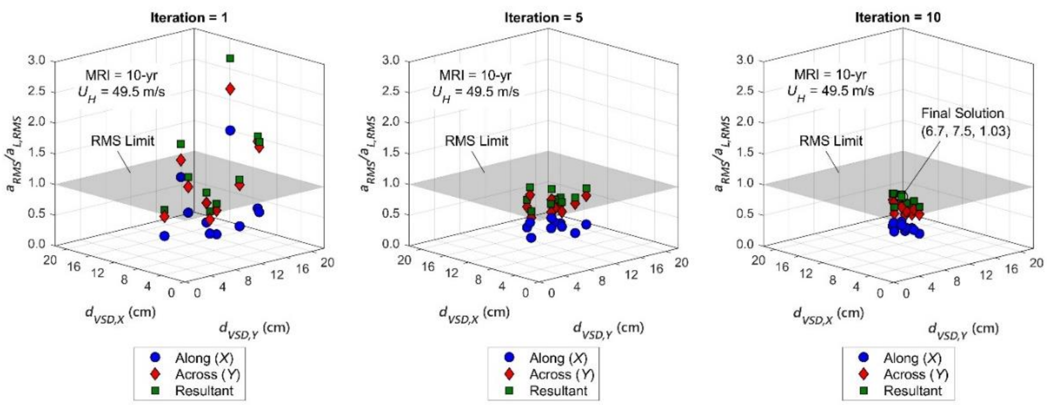

Figure 44. Convergence history of multivariate CPS optimization run (MRI = 10-yr) with independent control of lateral stiffness in the X- and Y-directions.

The proposed cyber-physical framework creates a suitable environment for optimizing the dynamics of tall buildings under more realistic loading conditions. For instance, the influence of neighboring structures can be readily incorporated into the BLWT setup and evaluated for several wind directions, turbulence levels, and hazard intensities (i.e., MRIs). In contrast, purely numerical optimization methods usually apply simplified wind loads for a single wind direction and interference effects from surrounding buildings are neglected; which may lead to conservative optimum designs. Furthermore, although the acceleration response of the aeroelastic specimen tested in the present work was primarily dominated by the two principal sway modes, torsional modes can significantly contribute to the horizontal acceleration response of many modern high-rise buildings (i.e., 3D coupled modes; Chen and Kareem, 2005). The contribution of torsion to the resultant acceleration can be captured experimentally through strategic placement of accelerometers mounted to the specimen. The use of aeroelastic models is also an attractive alternative to overcome the limitations of high frequency force balance (HFFB) techniques used in the wind tunnel, which are primarily suitable for buildings with uncoupled modes (Chan et al., 2009). However, to satisfy dynamic similitude requirements, very low wind velocities (U_H < 3 m/s assuming a 1:200 model scale) are required to simulate more frequent wind events (e.g., 1-yr MRI) in the BLWT, which may further magnify Reynolds number effects (Lim et al., 2007).

Although the present work focused on serviceability limit states, since these typically govern the design of the lateral structural system in tall buildings, strength requirements (e.g., demand-to-capacity indices) may potentially be incorporated as constraints to the optimization problem. However, constraint checks at the member level can bring physical challenges related to constructability and down-scaling of structural members comprising small-scale (e.g., 1:200) tall building models. One alternative is to integrate a finite element model of the structural system into the numerical (i.e., “cyber”) component of the CPS loop to evaluate member level performance while subjecting the structure to a realistic wind loading in the BLWT. These CPS experiments can provide direct uncertainty quantification of both the building dynamics (e.g., stiffness and damping) and the wind loading, which can help validate numerical probabilistic frameworks for tall building design and optimization (Spence & Kareem, 2014; Huang et al., 2012).

7.4 Summary

Preliminary results for the aeroelastic, tall building model with the VSDs are presented in this chapter in detail through the explanation of a test matrix. The purpose of the test matrix was to verify that all sensor instrumentation was returning data as expected and to obtain initial training data to develop an improved understanding of building behavior for different VSD configurations. This allowed for more realistic objective functions for the optimization of building performance in consideration of the VSD configuration.

The optimization problem setup is presented in this chapter in detail, including the specific objective, constraints, and ETE parameters. Testing details for the tall building model with the VSDs are presented in Table 15 and Table 16. The selection of problem-specific ETE parameters were chosen as N = 10, k_{max} = 8, θ_i = 0.3, θ_f = 0.8, α = 0.6, β = 1.0, and p = 30.

Table 15. Tall building model testing details with the VSDs for acceleration.

Test	CPS-OC-1	CPS-OC-2	CPS-OC-3
Objective statement [Minimize]	$a_{R,RMS} - a_{L,RMS}$	$a_{R,RMS} - a_{L,RMS}$	$a_{R,RMS} - a_{L,RMS}$
Constraint(s)	Domain: [10, 210] mm	Domain: [10, 210] mm	Domain: [10, 210] mm
Optimization method	ETE	ETE	ETE
Wind angle(s)	0°	0°	0°
Optimal result (full-scale)	0.173 Hz	0.168 Hz	0.176 Hz
Results discussion	Chapter 7.3.1	Chapter 7.3.1	Chapter 7.3.1

Table 16. Tall building model testing details with the VSDs for displacement.

Test	CPS-DR-1	CPS-DR-2
Objective statement [Minimize]	Overall and inter-story drift	Overall and inter-story drift

Constraint(s)	Overall: H/500 Inter-story: h/400 Domain: [10, 210] mm	Overall: H/500 Inter-story: h/400 Domain: [10, 210] mm
Optimization method	ETE	ETE
Wind angle(s)	0°	0°
Optimal result (full-scale)	0.180 Hz	0.179 Hz
Results Discussion	Chapter 7.3.2	Chapter 7.3.2

The ETE results for the aeroelastic, tall building model with the VSDs are then presented. For the aeroelastic, tall building the optimum design that would minimize the building natural frequency (i.e., maximize d_{VSD}) while satisfying multiple constraints is investigated. The iteration histories of candidate designs for independent optimization runs are provided to demonstrate their convergence to the optimum VSD configuration. The similar convergence behavior between the independent optimization runs demonstrate convergence and that it is a logical solution to the ETE algorithm which can be considered the optimum VSD configuration.

Chapter 8: CPS Modifications for Aerodynamic Optimization

The aeroelastic model with the VSDs was used in a cyber-physical approach for the optimization of tall building dynamics in a boundary layer wind tunnel (BLWT). The capabilities of the cyber-physical approach with the aeroelastic model could be further leveraged by exploring the design and optimization of tall building aerodynamics in a BLWT.

The proposed framework makes use of an aeroelastic building specimen with physically adjustable aerodynamic (i.e., shape) properties. The development of the aeroelastic, tall building specimen and the experimental equipment used for all BLWT testing of the aeroelastic specimen for aerodynamic optimization is initially presented in Chapter 5.1 and Chapter 5.2. All modifications to the aeroelastic specimen from Chapter 5.1 are presented in this chapter. The selection of the physically adjustable design variable and creation of a suitable actuation system for the control of the aerodynamics of the aeroelastic, tall building model are subsequently presented. This is accomplished through the use of an active fin system (AFS) consisting of twelve individually controllable slotted fin assemblies to adjust the model shape. The framework for providing data and power for controlling the actuation system is described to thoroughly depict the communication between cyber and physical components in the CPS incorporating the aeroelastic model for optimizing aerodynamic properties.

8.1 Aeroelastic specimen modifications

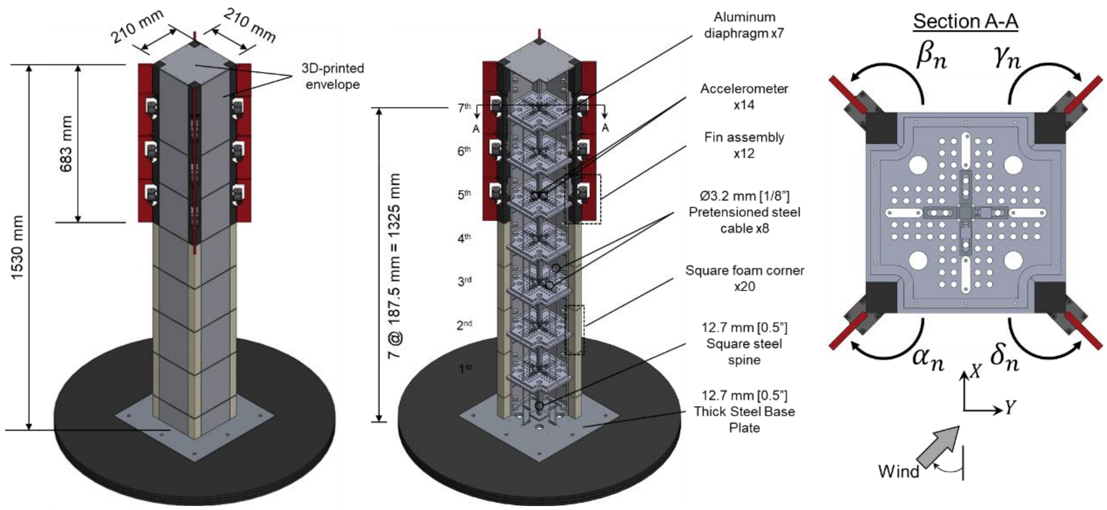

Figure 45. Multi-degree-of-freedom 1:200 aeroelastic tall building specimen with the active fin system (AFS).

The fully-constructed specimen can be seen in Figure 45. The corner geometry from Figure 29 was modified to consist of four square corners for the 1st, 2nd, 3rd, and 4th diaphragms (i.e., $n = 1$, 2, 3, and 4 in Figure 45) and four fin assemblies for the 5th, 6th, and 7th diaphragms (i.e., $n = 5$, 6, and 7 in Figure 45). The fin assemblies are discussed in further detail in Chapter 8.2. The total mass of the specimen, excluding the base plate, was 24.3 kg. Free vibration experiments were performed producing 1st mode full-scale natural frequencies of approximately 0.163 Hz. Damping ratios were estimated to be 2.5% using a log decrement method. The model with the AFS was primarily evaluated at approach angles of 0° and 25°. These angles were chosen to evaluate the effect of the AFS for different wind angles for the imposed fin symmetries, which will be discussed in further detail in Chapter 9.1.

8.2 Active fin system

Physical adjustment of the aerodynamic properties (i.e., shape) of the specimen was achieved through a series of twelve individually controllable slotted fin assemblies installed at three different heights of the four corners of a nominally square (in plan) building. The angles that the slotted fins make with respect to the building were adjusted using small (NEMA11) stepper-motors (Pololu #1206) capable of adapting to changes in both wind direction and wind speed.

An individual slotted fin assembly consisted of a core and slotted fin connected to one another and the stepper motor through the use of a connector and steel hardware. The core, slotted fin, motor-fin connector, and pin-pin connector are all individually 3D-printed components (made from ABSi). There were two different length fin assembles: a shorter one for the 5th and 6th diaphragms and a longer one for the 7th diaphragm. The cross section dimensions for a fin assembly are depicted in Figure 46, where dimension A is 20.5 mm and 143.4 mm for the shorter and longer fin assemblies, respectively. The contribution to the total model mass of each individual fin assembly (including the motor) was approximately 0.25 kg and 0.32 kg for the shorter and longer fin assemblies, respectively.

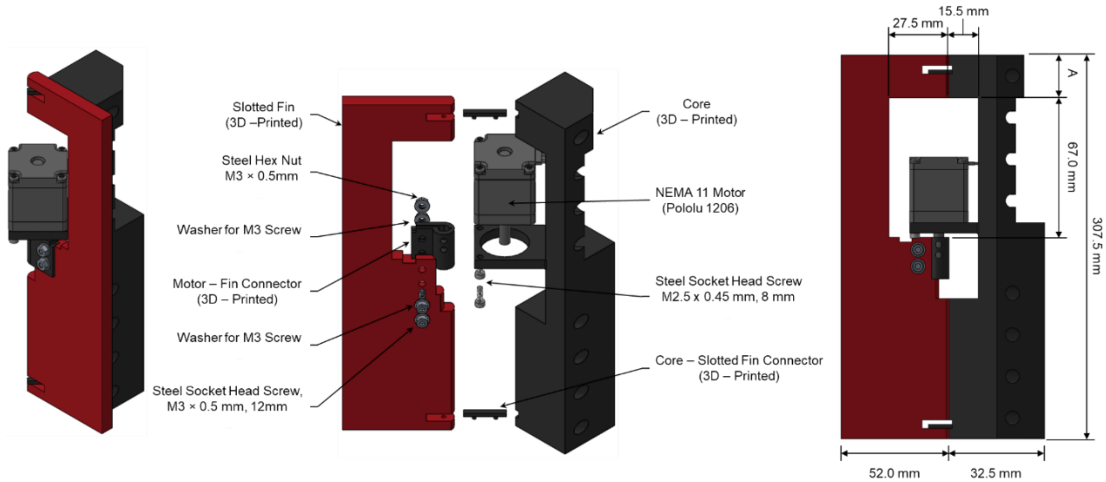

Figure 46. Schematic of a single fin assembly.

8.3 Cyber-physical setup

A detailed schematic of the actuation, sensor, and computer hardware setup in the BLWT for the aeroelastic testing considering the AFS is illustrated in Figure 47. For the aeroelastic testing considering the AFS, the cyberinfrastructure was similar to Chapter 6.3; computational hardware included an instrumentation and a coordinating computer housed in the BLWT control room. These computers were responsible for the execution of MATLAB and Python scripts, initializing the data collection, and collecting sensor data measurements using LabVIEW software. The model sensors consisted of accelerometers, vibration input modules, voltage input modules, signal conditioners, and CompactDAQ chasses identical to Chapter 6.3.

Figure 47 shows the fin assemblies located at the corners of the model, each equipped with a stepper motor (Pololu #1206). The stepper motors are connected to a motor controller (Pololu #3130) below the wind tunnel floor. The controllers communicated with a Raspberry Pi 3, which received commands from a Python script running on the coordinating computer, to adjust the fin angle relative to the model (i.e., α_n, β_n, γ_n, or δ_n; see Figure 45).

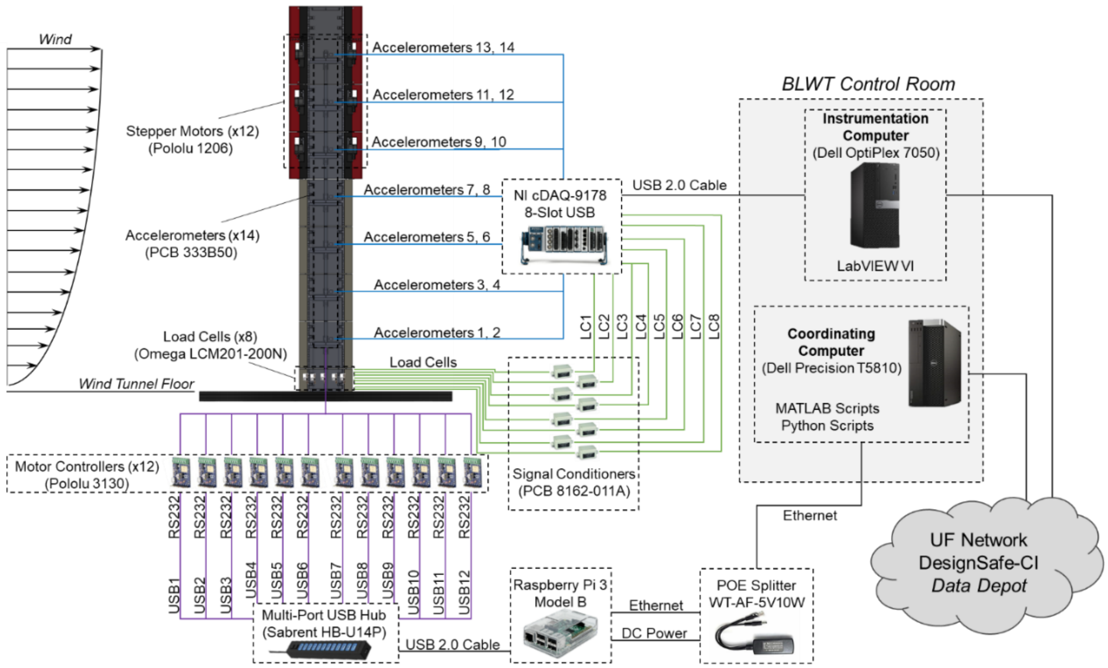

Figure 47. Schematic of actuation, sensor, and computer hardware for CPS aeroelastic experiments in the BLWT considering AFS.

8.4 CPS framework for aerodynamic optimization

8.4.1 CPS aerodynamic optimization problem

Tall buildings are continuously constructed in major cities worldwide, especially densely-populated cities where real estate is in high demand. The development and use of high-strength structural materials, lightweight flooring, and curtain wall systems facilitates this growth by reducing the structural dynamics (i.e., the weight, damping, and stiffness) of the constructed building. This increases the susceptibility of tall, slender structures to wind-induced vibrations which have the potential to cause occupant discomfort.

In the proposed CPS aerodynamic optimization framework, the objective was to make the necessary minor aerodynamic corner modifications using fins to minimize the aerodynamic response. Essentially, determine the fin configuration which minimizes the resultant acceleration or resultant displacement building response near the top of the structure.

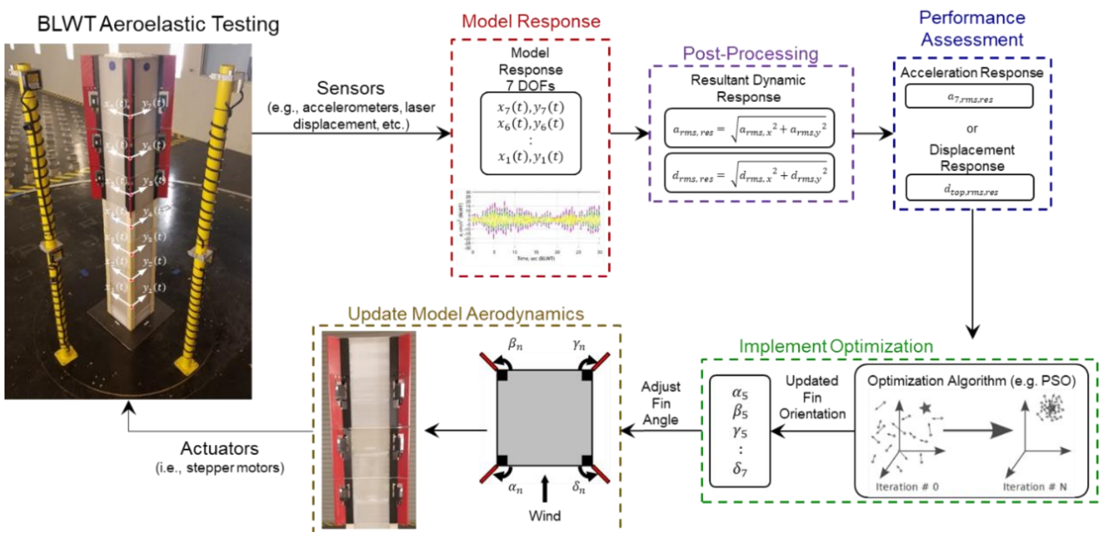

Figure 48. High level diagram of CPS approach for aerodynamic optimization.

8.4.2 Aerodynamic optimization algorithm

The type of optimization algorithm best applied to the CPS approach is problem-dependent and should be selected based on factors such as the number of design variables, expected measured variance in results for repeated tests, and total allowable trading time. The optimization algorithm integrated into the CPS approach for the study of the aeroelastic model considering the AFS was a modified PSO algorithm. PSO is a population-based metaheuristic optimization algorithm that mimics the social behavior of a population (swarm) of individuals (particles) jointly discovering and exploring promising regions within a feasible design space. Each particle within the swarm has a finite position and velocity within the search space at each iteration, as expressed by Equation (7) and Equation (8) in Chapter 2.3.2.1, respectively.

The PSO modification of a "forgetting function" first introduced in Chapter 4.2.3 was implemented in the study of the aeroelastic model with the AFS. The "forgetting function" would cause the particles within the swarm to "forget" both local and global best solutions beyond a specified number of previous iterations, preventing any convergence to an outlier experiment. The number of previous iterations to consider for local and global best calculations, j_k was selected to be 3, for a total of 4 iterations (i.e., the current iteration and 3 previous iterations). The modified velocity equation considering the forgetting function is then defined as expressed by Equation (16).

8.5 Summary

This chapter outlines the method to extend the capabilities of the aeroelastic model for a cyber-physical approach to aerodynamic optimization. All modifications to the aeroelastic specimen from Chapter 5.1 are presented in detail in this chapter. The specifications of the individually controllable slotted fin assemblies within the AFS provide a better understanding of the physically adjustable design variable and actuation system used for controlling model aerodynamics (i.e., shape). The cyber-physical setup for aerodynamic optimization is illustrated. The framework and optimization algorithms for aerodynamic optimization are subsequently presented.

Chapter 9: Aeroelastic Testing and Aerodynamic Optimization

This chapter details the testing of the aeroelastic, tall building model comprised of preliminary results in the form of a test matrix and then the results and analysis of stochastic optimization problems presented subsequently. The test matrix for the active fin system (AFS) testing includes a discrete set of wind approach angles for a comprehensive set of fin angles. For all AFS testing the variable stiffness devices (VSDs) from Chapter 6.1 are set to a constant length of 10 millimeters.

9.1 Initial test matrix and problem formulation for AFS model configuration

A test matrix for the AFS testing was obtained by testing wind approach angles of 0º and 45º for two different imposed fin symmetries (Figure 49a and Figure 49b) along the height of the AFS. Fin angles (θ, ϕ, ψ) from 0º to 270º were tested for 90 seconds for each wind approach angle at increments of 45º. The test matrix served to validate that all of the accelerometers and laser displacement sensors were continuing to return reasonable data as expected.

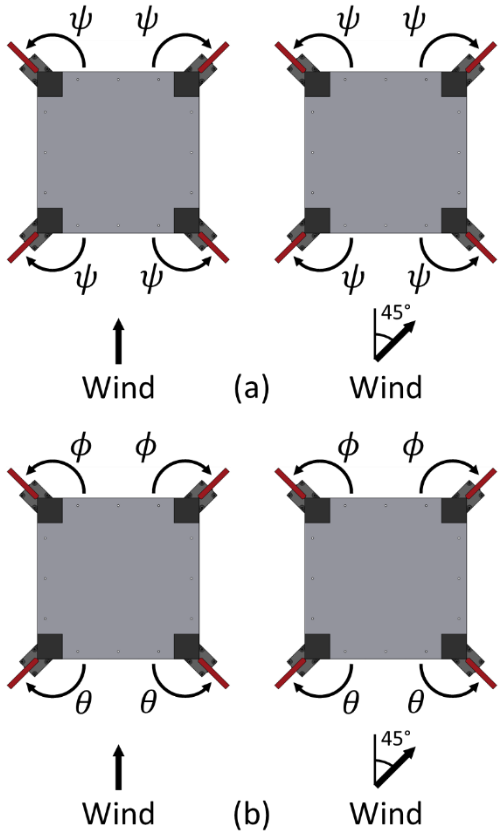

Figure 49. Fin symmetries imposed for AFS test matrix.

The purpose of the test matrix with the AFS was to obtain training data to develop a better understanding of the dynamic response of the building for varying AFS configurations. This allowed for the development of realistic objective functions for the optimization of building performance in consideration of the AFS configuration.

There is an observed tradeoff between the resultant accelerations and displacements for the studied fin symmetries. This tradeoff is best observed under the approach angle of 0º and demonstrated by Figure 50. As the windward and leeward fin pairs change angles, the tradeoff between displacements and accelerations represent a tradeoff that can be translated into a simple optimization problem.

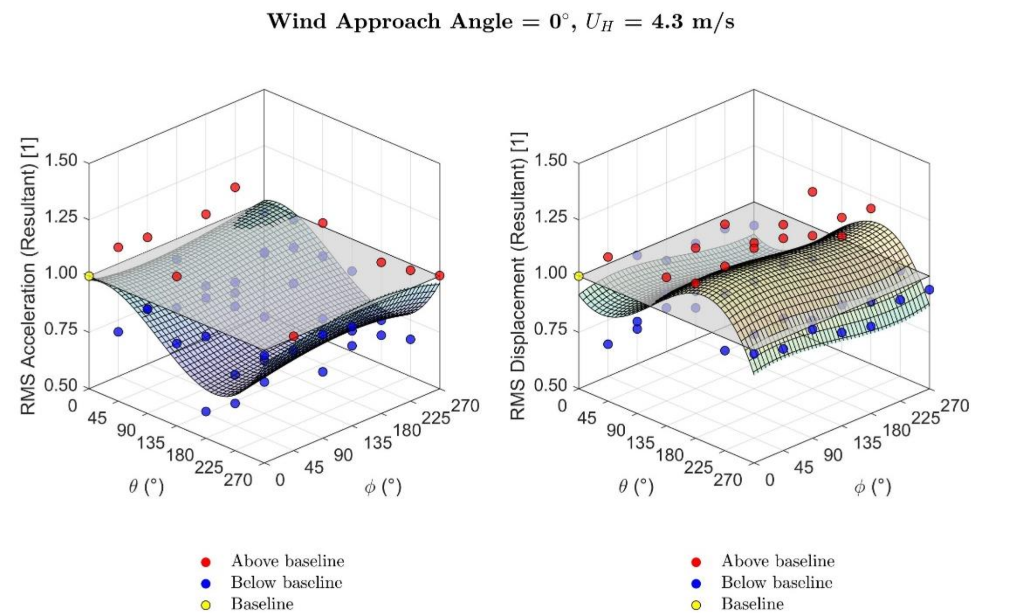

Figure 50. Root-mean-square (RMS) acceleration and displacement resultant response considering AFS with enforcement of windward (θ) and leeward (ϕ) pair symmetry.

The behavior illustrated in Figure 50 can be best explained by examining the along- and across-wind acceleration and displacement time history responses for the configuration of θ = 180º and ϕ = 90º. Figure 51 and Figure 52 illustrate the along- and across- wind accelerations and displacements for the given configuration.

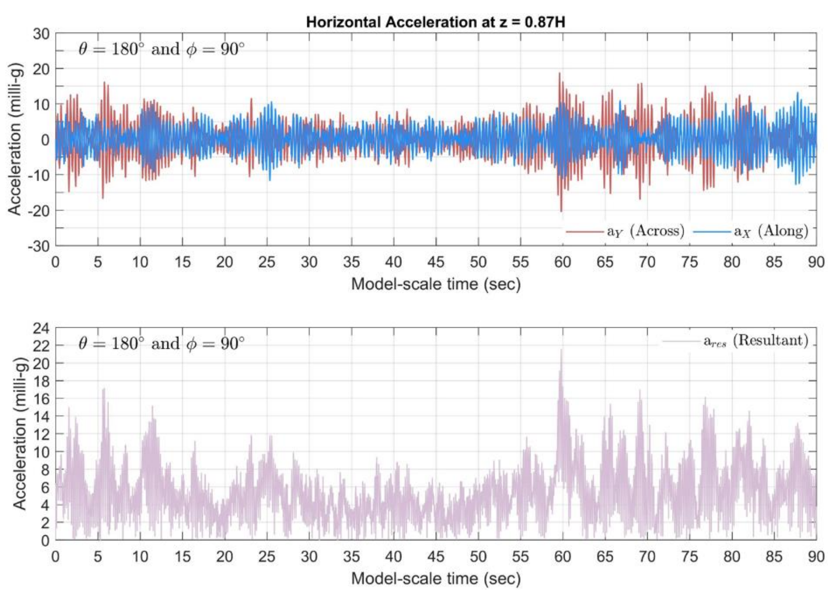

Figure 51. Along- and across-wind acceleration response for θ = 180º and ϕ = 90º (Figure 49b) for a wind approach angle of 0° (dimensions are in model-scale).

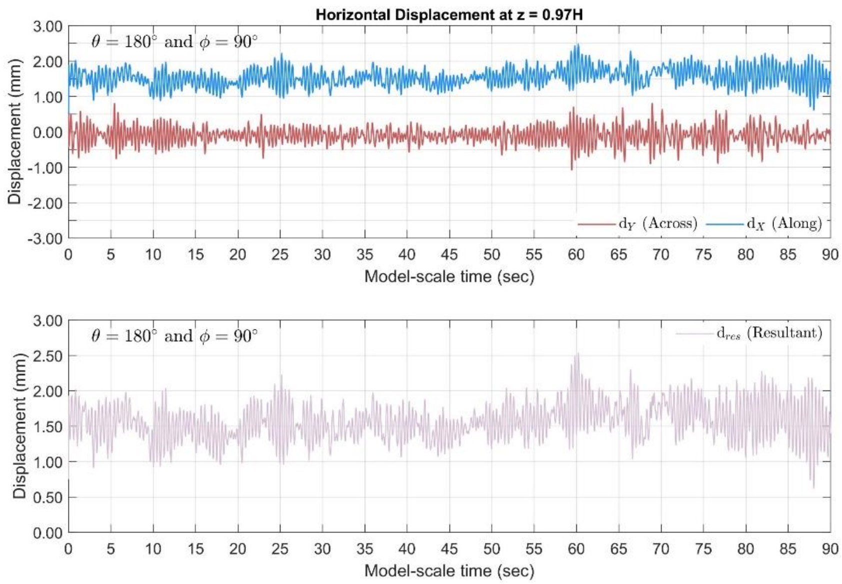

Figure 52. Along- and across-wind displacement response for θ = 180º and ϕ = 90º (Figure 49b) for a wind approach angle of 0° (dimensions are in model-scale).

Windward fin angles of 180º reduce the across-wind acceleration response while simultaneously increasing the surface area of the building normal to the flow direction, leading to an increase in along-wind displacements.

Figure 53 and Figure 54 illustrate the effect of wind directionality on building response for a given building configuration using two model configurations: 1) θ = 90º and ϕ = 180º and 2) θ = 180º and ϕ = 90º. These model configurations represent the same building configuration under two different wind directions of 0º and 180º, respectively.

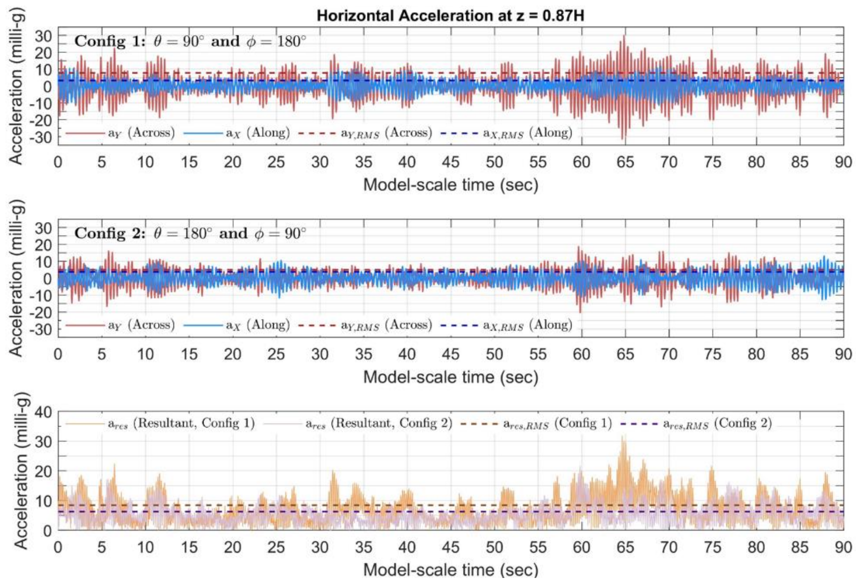

Figure 53. Acceleration response comparison for two model configurations: 1) θ = 90º and ϕ = 180º and 2) θ = 180º and ϕ = 90º (Figure 49b) (dimensions are in model-scale).

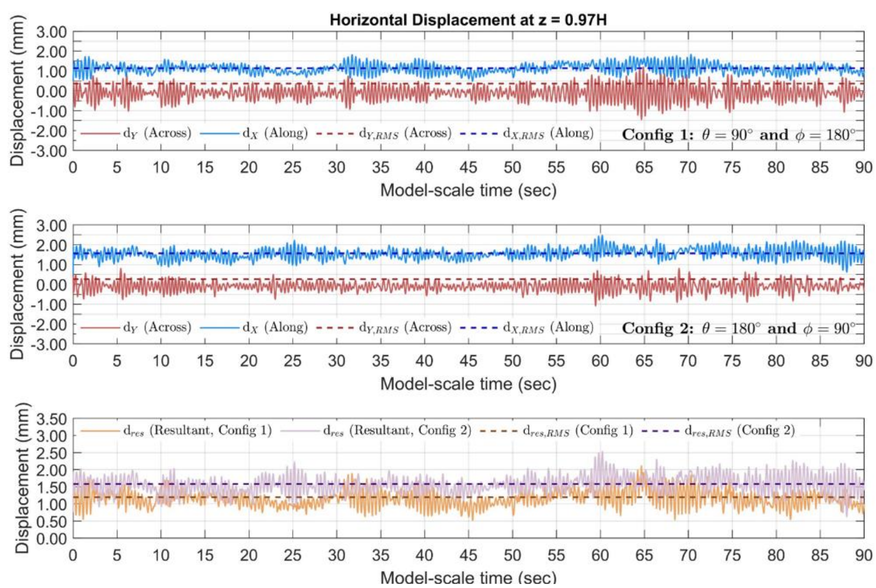

Figure 54. Displacement response comparison for two model configurations: 1) θ = 90º and ϕ = 180º and 2) θ = 180º and ϕ = 90º (Figure 49b) (dimensions are in model-scale).

Configuration 1 results in a larger resultant acceleration response and smaller resultant displacement response than Configuration 2. Therefore, the given building configuration performs better for acceleration response when wind is at 180º and better for displacement response when wind is at 0º.

9.2 Aerodynamic optimization results and analysis

In this study, three independent single-objective optimization runs were performed. The alternative objective functions considered were minimizing the resultant root-mean-square (RMS) acceleration, $a_{R,\mathrm{RMS}}$ at z = 0.87H for an approach angle of 0° (FIN-ACC-00), minimizing the resultant RMS displacement, $d_{R,RMS}$ at z = 0.97H for an approach angle of 0° (FIN-DISP-00), and minimizing $a_{R,RMS}$ at z = 0.87H for an approach angle of 25° (FIN-ACC-25) where

$$a_{R,RMS} = \sqrt{{a_{X,RMS}}^2 + {a_{Y,RMS}}^2} \tag{26}$$

$$d_{R,RMS} = \sqrt{{d_{X,RMS}}^2 + {d_{Y,RMS}}^2} \tag{27}$$

The performance criterion of acceleration and displacement are minimized to mitigate wind-induced building vibrations and to decrease overall building drift, respectively. Excessive vibrations can interfere with building occupants' overall comfort, while extreme deformations can damage non-structural elements (e.g., ceilings, cladding, and partitions). RMS statistics provide a more reliable and repeatable statistical measure of the relevant building response (i.e., acceleration or displacement). Approach angles of 0° and 25° were evaluated to investigate the effect of the approach angle on the optimal fin configuration. Although the height selected for FIN-ACC-00 and FIN-ACC-25 was z = 0.87H and z = 0.97H for FIN-DISP-00, the approach is valid for any height along the building.

The optimization problems were physically constrained by the minimum and maximum fin angles of 0 and 270°, respectively. The lower and upper physical bounds were chosen such that the search space consisted of all possible angles between orthogonal building surfaces and so that the optimal solution was confidently located within the search space. The fin angles were rounded to the nearest 0.1° based on the resolution of stepper motors used. The fin symmetry of Figure 55 was enforced for all optimization problems based off of the behavior observed using a pre-recorded test matrix of wind angles and fin configurations. Thus, θ_n (Figure 55) $= \alpha_n$ and β_n (Figure 45), and ϕ_n (Figure 55) $= \gamma_n$ and δ_n (Figure 45). This symmetry was enforced for the fins at the 5th, 6th, and 7th diaphragms (Figure 45) for a total of six design variables – two pairs of fins per diaphragm (θ_n and ϕ_n) at each of three diaphragms (i.e., $n = 5$, 6, and 7 in Figure 45). The corner geometry for the remaining diaphragms (i.e., $n = 1$, 2, 3, and 4 in Figure 45) was square corners at each corner.

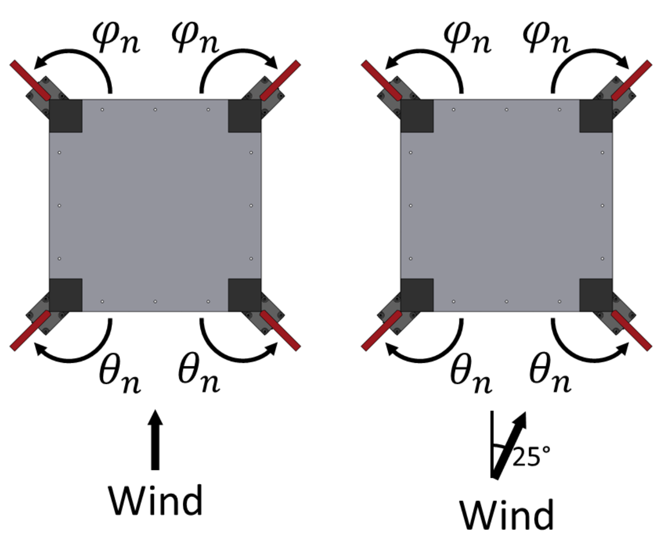

Figure 55. Fin pair symmetry enforced for each wind approach angle.

All three independent CPS optimization runs were tested using wind speeds of 4.3 m/s for 60 seconds in the boundary layer wind tunnel (BLWT), corresponding to wind speeds of 60.8 m/s for 14 minutes full-scale. FIN-ACC-00 and FIN-DISP-00 were tested at approach angles of 0° while FIN-ACC-25 was tested at an approach angle of 25° (as defined in Figure 55).

Table 17 summarizes the problem-specific PSO parameters for the three independent optimization runs, FIN-ACC-00, FIN-DISP-00, and FIN-ACC-25. The parameters of w, c_1, and c_2 were selected to provide an equal weighting to each component of particle i's velocity, v_j^i at iteration j.

Table 17. PSO parameters for three independent optimization runs.

CPS Optimization Run	w	c_1	c_2	Position initialization	Maximum iterations	Population size	j_k
FIN-ACC-00	0.5	1.0	1.0	Randomly distributed	15	10	3
FIN-DISP-00	0.5	1.0	1.0	Randomly distributed	15	10	3
FIN-ACC -25	0.5	1.0	1.0	Randomly distributed	10	10	3

9.2.1 Minimize RMS resultant acceleration, approach angle = 0°

Previous studies have demonstrated that the human perception of wind-induced motion can be directly linked to the horizontal acceleration of the building (e.g., Kwok et al. 2009; Bernardini et al. 2014). Peak and RMS floor accelerations are typically considered to represent building motion (Boggs 1997). The horizontal building acceleration is comprised of translational motion components in directions orthogonal to the principal building axes. The objective was selected as a minimization of the resultant RMS acceleration at the top of the building.

The convergence of the individual design variables towards the optimum configuration is shown in Figure 56a. The convergence is illustrated for each design variable, separated by windward or leeward pairs and by diaphragm number. A visualization of the fin assembly pairs for each diaphragm is presented, following the same angle convention as in Figure 55.

The global best cost for each iteration is shown in Figure 56b. The solid black line represents the path of the global best cost of the swarm at each iteration. The global best position determined at iteration 6 by particle 9 attracts all particles to this particular fin configuration. Different configurations similar to this optimal solution are tested and the fin configuration of particle 10 in iteration 12 is found to produce a better cost once the particular test at iteration 6 is forgotten. This suggests that the solution found to be the global best at iteration 6 was not representative of the fin configuration and could be considered an outlier.

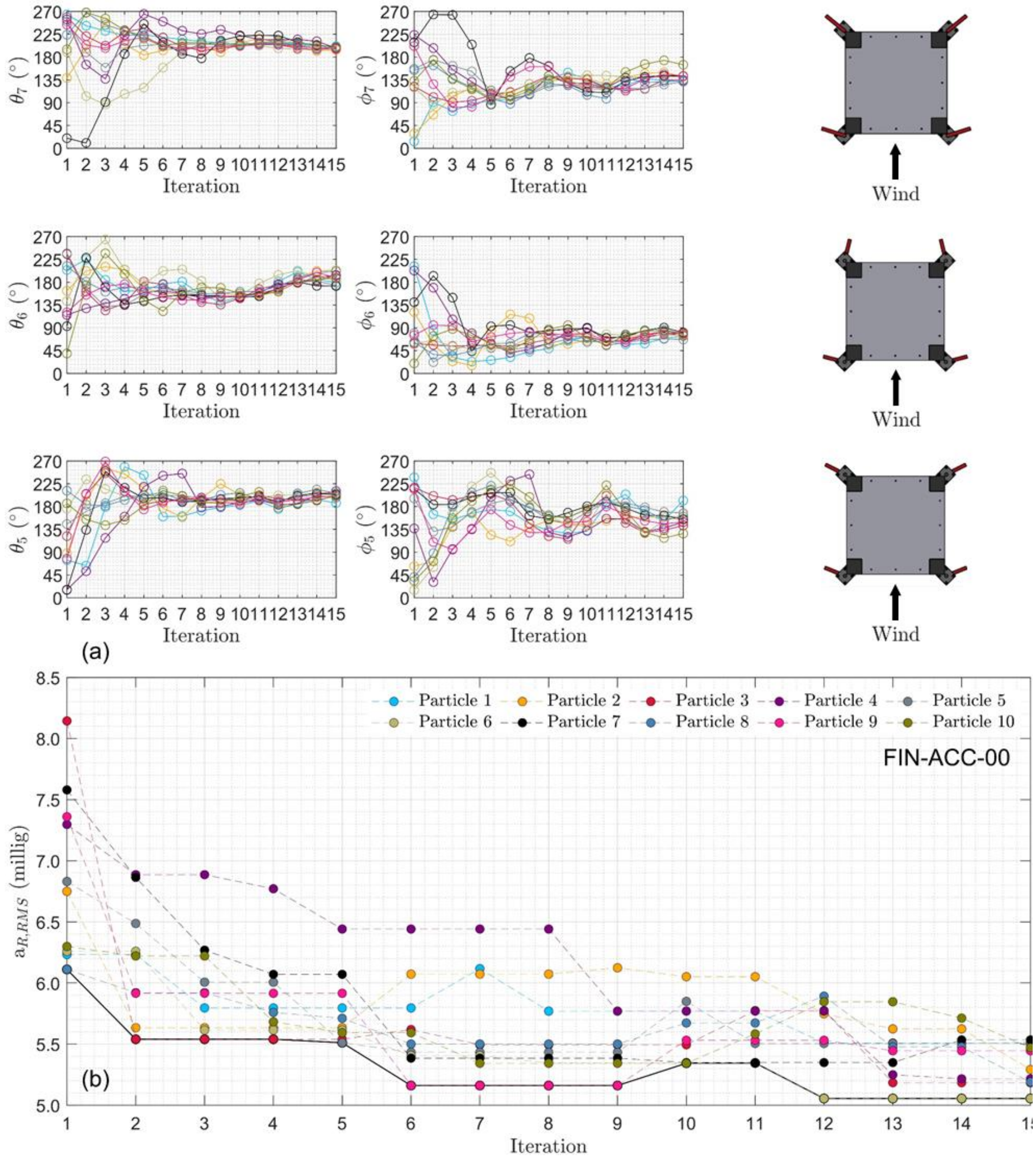

Figure 56. (a) Particle convergence at each iteration and (b) Iteration cost history for FIN-ACC-00 (dimensions are in model-scale).

<u>9.2.2 Minimize RMS resultant displacement, approach angle = 0°</u>

Serviceability limit states addressing excessive building deflections are of concern to designers for ensuring the integrity of non-structural elements (e.g., ceilings, cladding, and partitions) under wind-induced deformations (Simiu, 2011). There is an observed trade-off between the along- and across-wind displacement response for the studied fin symmetries. For example, multiple fin configurations mitigate across-wind displacement response, but might simultaneously cause large pressure buildups on the windward face, which can lead to a larger along-wind static response.

The convergence of the individual design variables towards the optimum configuration is shown in Figure 57a. The global best cost for each iteration is shown in Figure 57b.

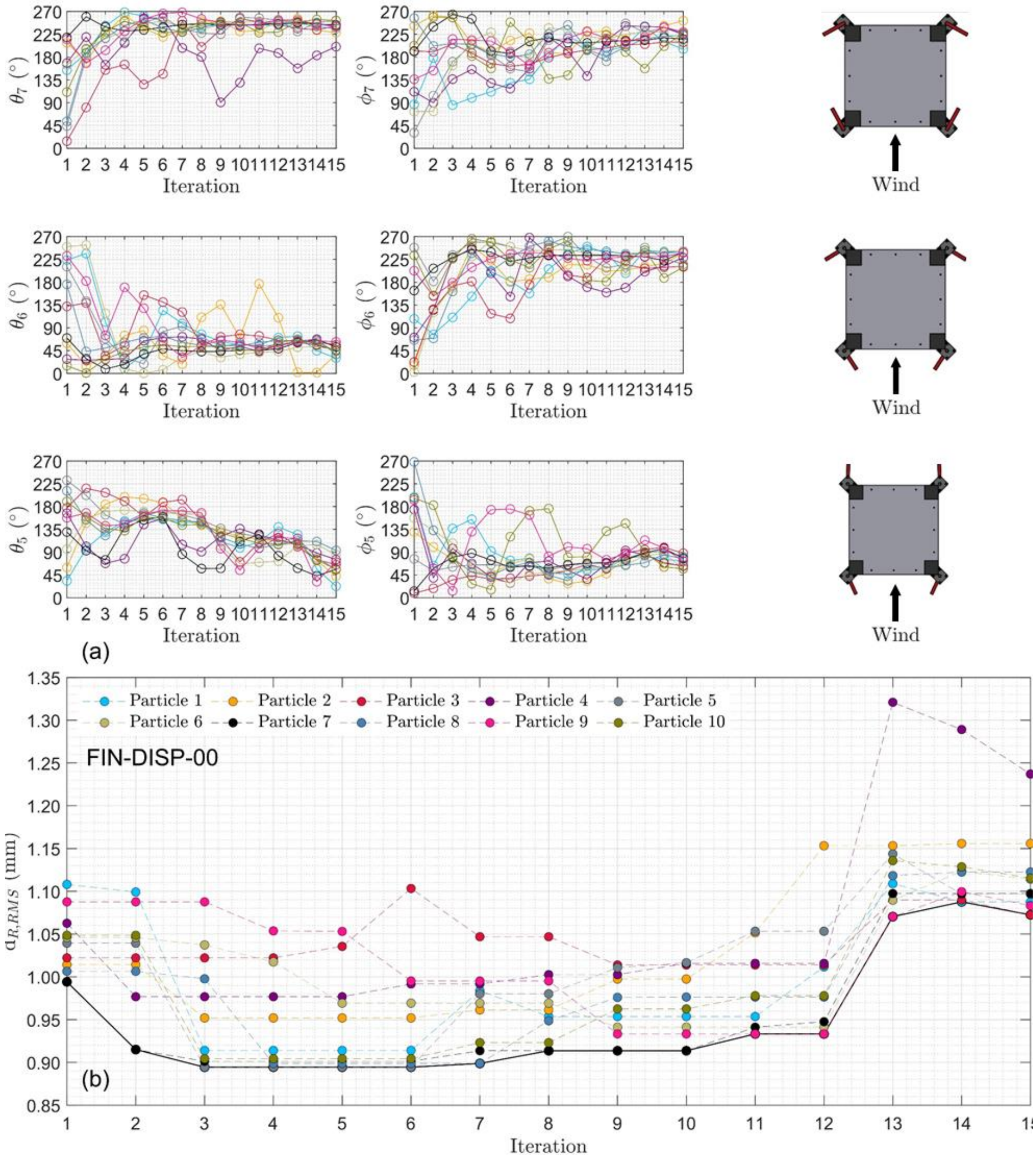

Figure 57. (a) Particle convergence at each iteration and (b) Iteration cost history for FIN-DISP-00 (dimensions are in model-scale).

9.2.3 Minimize RMS resultant acceleration, approach angle = 25°

The wind approach angle alters the overall building response; a fixed aerodynamic configuration will affect the aerodynamic response differently. In other words, a given configuration could both mitigate and amplify the dynamic response (i.e., overall drift and top-story acceleration) for two different wind approach angles. Implementing an active system could prevent this potential amplification of a fixed system and provide the configuration best-suited for the current environmental conditions, given prior knowledge of the wind approach angle.

The convergence of the individual design variables towards the optimum configuration is shown in Figure 58a. The global best cost for each iteration is shown in Figure 58b.

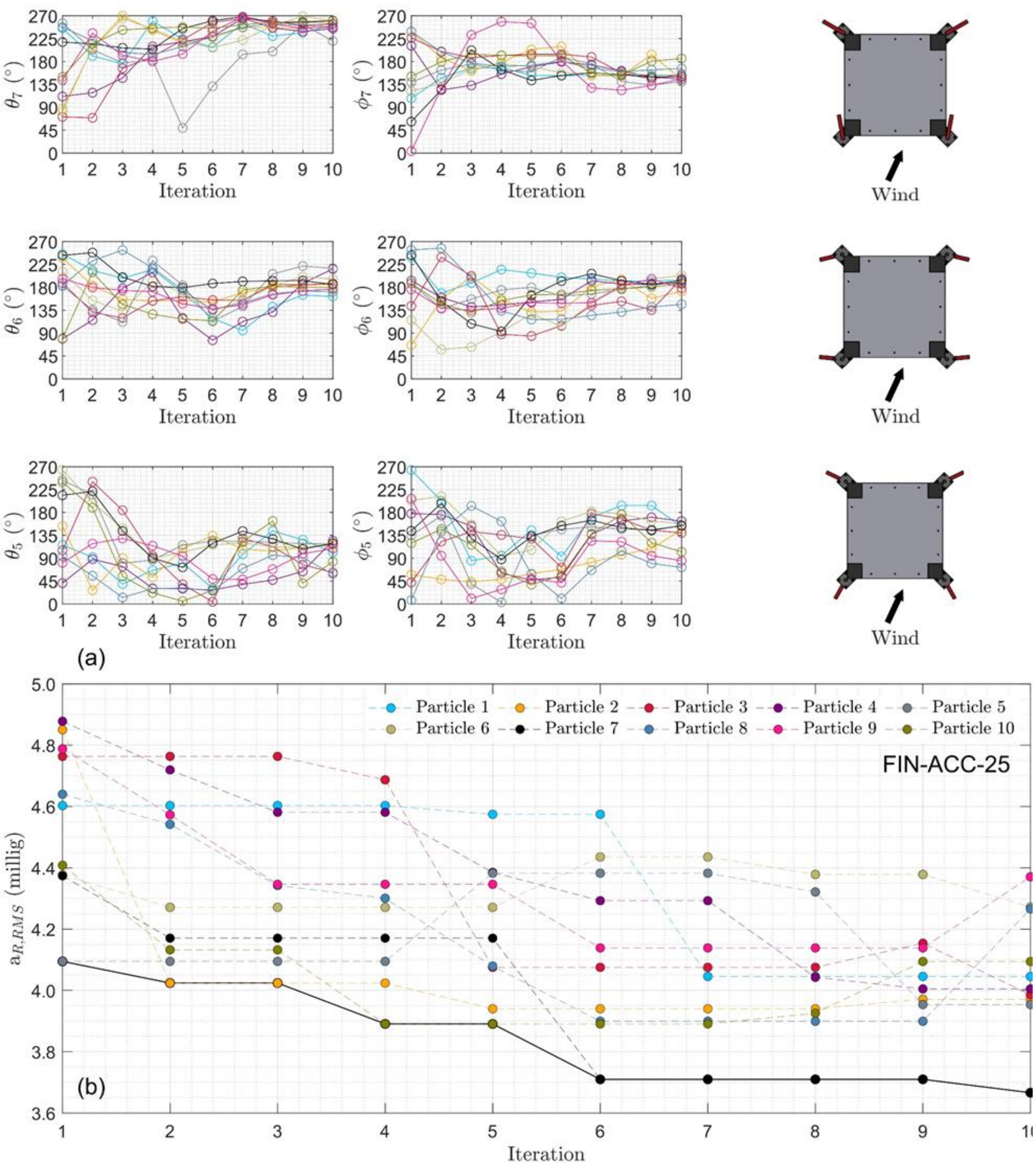

Figure 58. (a) Particle convergence at each iteration and (b) Iteration cost history for FIN-ACC-25 (dimensions are in model-scale).

9.3 Discussion of aerodynamic optimization

A visualization of the optimal fin configurations is illustrated in Figure 59 for FIN-ACC-00 (Figure 59a), FIN-DISP-00 (Figure 59b), and FIN-ACC-25 (Figure 59c).

Table 18 also includes the relevant $a_{R,RMS}$ and $d_{R,RMS}$ values for the three independent optimization runs.

For the 0° approach angle (FIN-ACC-00 and FIN-DISP-00), the optimal configuration is dependent upon the specified design objective. The optimal angle of all windward fin pairs for FIN-ACC-00 is approximately 180°. Based on offline analysis of a pre-recorded test matrix of fin configurations, the windward fins (θ_5, θ_6, and θ_7) had a significantly larger effect on the building response (i.e., accelerations and displacements) than the leeward fins (ϕ_5, ϕ_6, and ϕ_7). For an approach angle of 0°, a fin angle of 180° was found to effectively reduce the across-wind response, possibly due to the diversion of wind flow from the structure's side walls. While windward fin angles of approximately 180° reduces the across-wind acceleration, the increase in surface area of the building normal to the flow direction leads to an increase in along-wind displacements. These findings are in agreement with previous studies (Kwok and Bailey 1987). In contrast, the optimal angle of all windward fins for FIN-DISP-00 are near flush with the building. This configuration prevents the buildup of pressure that occurs from the optimal configuration of FIN-ACC-00.

For a consistent design objective (FIN-ACC-00 and FIN-ACC-25), the optimal configuration is dependent upon the wind approach angle. Whereas the windward fin pairs for FIN-ACC-00 are all approximately 180°, the optimal configuration of windward pairs for FIN-ACC-25 change based on their height along the building.

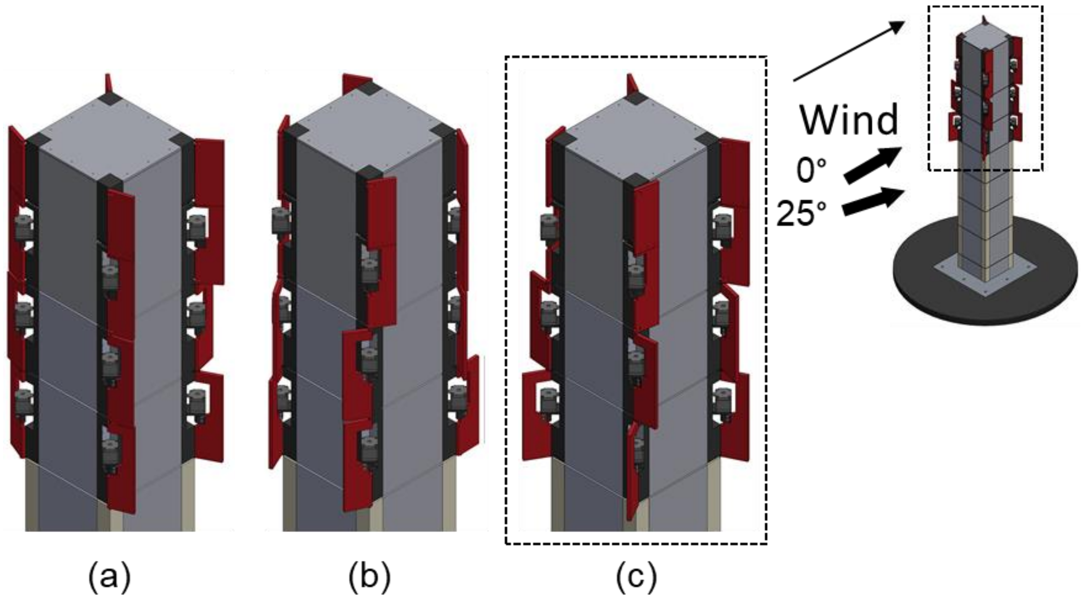

Figure 59. Optimal fin configurations for (a) FIN-ACC-00, (b) FIN-DISP-00, and (c) FIN-ACC-25.

Table 18. Final acceleration and displacement response of optimal fin configurations (see Figure 55) for FIN-ACC-00, FIN-DISP-00, and FIN-ACC-25 (dimensions are in model-scale).

Independent CPS Optimization Run	θ_5 (°)	ϕ_5 (°)	θ_6 (°)	ϕ_6 (°)	θ_7 (°)	ϕ_7 (°)	$a_{R,RMS}$ (milli-g)	$d_{R,RMS}$ (mm)
FIN-ACC-00	202.1	153.0	194.4	76.1	197.5	140.7	5.05	N/A
FIN-DISP-00	65.3	87.9	56.7	211.5	241.0	209.2	N/A	1.07
FIN-ACC-25	119.4	154.3	185.6	193.5	260.0	150.1	3.67	N/A

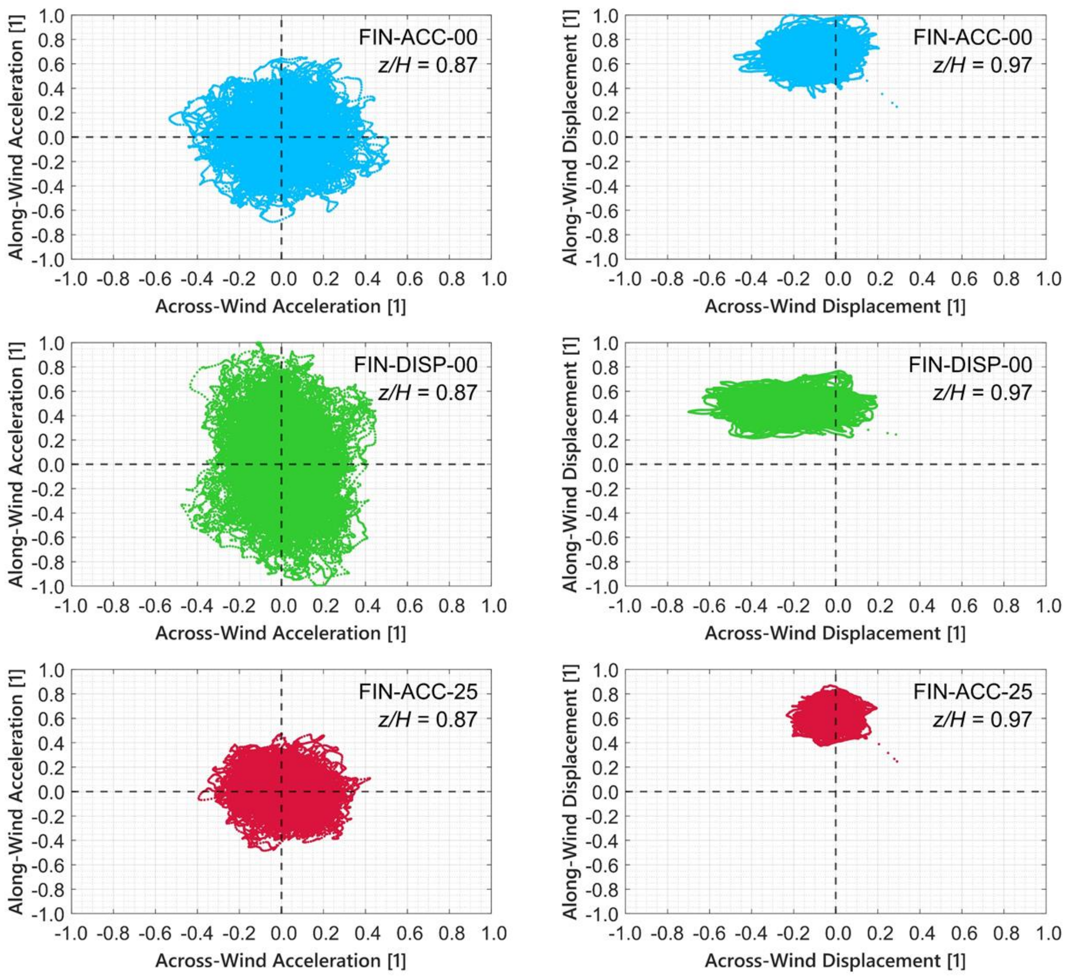

Figure 60. Normalized along-wind and across-wind acceleration and displacement response of building with optimal fin configurations for FIN-ACC-00, FIN-DISP-00, and FIN-ACC-25.

The relationship between normalized along-wind and across-wind acceleration and displacement responses for the optimal configurations of the three independent optimization runs can be seen in Figure 60. Accelerations are displacements are measured at $z = 0.87H$ and $z = 0.97H$, respectively. It is evident that both the along- and across-wind acceleration responses for FIN-ACC-00 and FIN-ACC-25 are lower than that for FIN-DISP-00. Additionally, the along-wind displacement response for FIN-DISP-00 is lower than that of FIN-ACC-00 and FIN-

ACC-25. There is an observed tradeoff between peak acceleration and displacement responses for FIN-ACC-00 and FIN-DISP-00. The optimal configuration for FIN-ACC-00 has a higher along-wind displacement response than FIN-DISP-00 due to the increased projected area normal to the wind, whereas FIN-DISP-00 has a higher along-wind acceleration response than FIN-ACC-00. Additionally, there is a balance between along- and across-wind accelerations for optimization problems considering acceleration (FIN-ACC-00 and FIN-ACC-25), whereas the optimal configuration for displacement results in significantly higher along-wind accelerations.

Given previous knowledge of both the wind direction and intensity, an active fin system would be capable of minimizing either the acceleration or displacement. Depending on the wind intensity, the user can select to minimize the acceleration or displacement to maximize occupant comfort or the structural safety, respectively. If the wind direction is also known, the fins can be adjusted to minimize the selected response based on a pre-determined optimal solution. Thus, both prior knowledge of modern weather conditions and access to an active fin system would allow for a consistent minimization of the structural response for wind storms of varying return periods.

9.4 Summary

Preliminary results for the aeroelastic, tall building model with the AFS are presented in this chapter in detail through the explanation of a test matrix. The purpose of the test matrix was to verify that all sensor instrumentation was continuing to return reasonable data, and to obtain initial training data to develop a better understanding of the building's dynamic response for varying AFS configurations. This allowed for the development of more realistic objective functions for the optimization of building performance in consideration of the AFS configuration.

The optimization problem setup is presented in this chapter in detail, including the specific objective, constraints, and PSO parameters. Testing details for the tall building model with the AFS are presented in Table 19. The selection of problem-specific PSO parameters were chosen as $w = 0.5$ and $c_1 = c_2 = 1.0$. The parameters of w, c_1, and c_2 were selected to provide an equal weighting to each velocity component, accounting for the independent random numbers r_1 and r_2 in the range [0,1] in Equation (8).

Table 19. Tall building model testing details with the AFS.

Test		FIN-ACC-00	FIN-DISP-00	FIN-ACC-25
Objective statement [Minimize]		$a_{R,RMS}$	$d_{R,RMS}$	$a_{R,RMS}$
Constraint(s)		Domain: [0°, 270°]	Domain: [0°, 270°]	Domain: [0°, 270°]
Optimization method		PSO	PSO	PSO
Wind angle(s)		0°	0°	25°
Optimal result	θ_5	202.1°	65.3°	119.4°
	ϕ_5	153.0°	87.9°	154.3°
	θ_6	194.4°	56.7°	185.6°
	ϕ_6	76.1°	211.5°	193.5°
	θ_7	197.5°	241.0°	260.0°
	ϕ_7	140.7°	209.2°	150.1°
Results Discussion		Chapter 9.2.1	Chapter 9.2.2	Chapter 9.2.3

The PSO results for the aeroelastic, tall building model with the AFS are then presented. For the aeroelastic, tall building the optimum designs that would minimize the resultant RMS acceleration for an approach angle of 0°, the resultant RMS displacement for an approach angle of 0°, and the resultant RMS acceleration for an approach angle of 25° are independently investigated. The particle position histories for the independent optimization runs are provided to demonstrate their convergence to the optimum AFS configurations. The successful convergence of the ten particles to the same set of design variables (i.e., windward and leeward angles for the 5^{th}, 6^{th}, and 7^{th} diaphragms) suggests that the configurations are logical solutions to the independent PSO algorithms and can be considered the optimal configurations.

Chapter 10: Conclusions and Future Studies

10.1 Conclusions

This dissertation provides systematic studies on the development and validation of a cyber-physical approach to the optimal design of civil structures in consideration of wind hazards. The main goal is to develop an approach which improves the efficiency and accuracy of the optimization process for wind-sensitive structures under user-specified objectives. There were two buildings selected for independent study; first, a low-rise building with a parapet wall and second, a landmark tall building. While applied to these two specific structures, the framework developed in this dissertation enables the evaluation of other structures (e.g., bridges or other buildings). Additionally, the proposed cyber-physical optimization procedure will ensure that the solution space is being more exhaustively explored than traditional approaches by incorporating optimization algorithms.

The study of the low-rise building with a parapet focused on the direction of induced pressures on the building roof due to the presence of a parapet and the determination of the optimum parapet height considering a static pressure envelope. A boundary layer wind tunnel was used to obtain a better understanding of the behavior of the flow of wind across a structure with a parapet. After performing necessary preliminary testing to ensure that model construction was performed properly and the model was exhibiting anticipated behavior, a modified single-objective particle swarm optimization algorithm, single-objective golden section search, and multi-objective particle swarm optimization were independently implemented.

The study of the landmark tall building focused on the exploration of the magnitude of dynamic response (e.g., accelerations and displacements) due to varying stiffness and aerodynamic properties considering a static pressure envelope. A boundary layer tunnel was used to better capture the wind-induced response associated with complex fluid-structure interaction (e.g., vortex shedding) behavior. After performing necessary preliminary testing to ensure that model construction was performed properly and the model was exhibiting anticipated behavior, single-objective explore-then-exploit and single-objective particle swarm optimization were independently implemented.

The exploratory properties of metaheuristic optimization algorithms (e.g., particle swarm optimization and explore-then-exploit) allow for the possibility of non-intuitive solutions, while golden section search is a root-finding method that ensures the retesting of candidate solutions, a strength in experimental testing. The modified particle swarm optimization algorithm proposed in this dissertation proved to be a feasible algorithm. Implications are significant for more complex structures where the optimal solution may not be obvious and cannot be reasonably determined with traditional experimental or computational methods. Solutions found with the CPS approach have a higher degree of realism than purely numerical (computational fluid dynamics) methods and obtain optimal results quicker than purely experimental methods.

Several unique contributions were presented, including the investigation of different types of building models (i.e., rigid and aeroelastic) and optimization algorithms (i.e., stochastic and non-stochastic), for the implementation in a CPS framework. Additionally, multi-objective optimization was integrated with consideration of both components and cladding and the main wind force resisting system. Multi-objective optimization allows the cooperation of architects, engineers, owners, and other stakeholders to obtaining a design which can satisfy competing objectives of different stakeholders. Thus, incorporating a mechatronic specimen with multi-objective optimization allows for the automation of the design process of the entire building system. The capabilities of cyber-physical systems within wind engineering were extended further to the design and optimization of wind-sensitive tall buildings through the use of an aeroelastic, tall building specimen with physically adjustable dynamic and aerodynamic properties.

10.2 Future studies

Some recommendations for future studies related to this work are detailed below based on the models used in this study, the existing CPS framework, and cyber-physical systems.

- Rigid, low-rise parapet model. In this dissertation, the optimum parapet height is determined from optimal C_p values on the roof, inner parapet walls, and top of the parapet wall. Further studies should focus on optimizing the total weight of the underlying structural frame, to include the cost of the parapet.

- Aeroelastic, tall building model. In this dissertation, the optimization for the aeroelastic, tall building model is for independent single-objective functions. Further studies should focus on multi-objective optimization of the tall building model using the variable stiffness devices (VSDs) and/or the active fin system (AFS) through the use of wind tunnel testing.
- CPS framework. In this dissertation, the CPS framework for both the rigid, low-rise parapet model and the aeroelastic, tall building model relies on no previous testing and only uses results from configurations tested during the optimization process. Incorporating predictions based on previously tested configurations through machine learning methods offers the opportunity to simultaneously improve the understanding of model behavior and reduce the number of tested model configurations, both for the test matrix and the optimization procedure. Given the limited availability of resources (e.g., time) for testing, reducing the required number of tested configurations would allow for additional optimization procedures or more complex models to be incorporated into the CPS framework.
- CPS framework. Particle swarm optimization and explore-then-exploit (a hybridization of particle swarm optimization and big-bang big-crunch) were selected for the optimization algorithms. Future work should consider alternative optimization algorithms, including gradient-based algorithms which may be more efficient for simpler design problems.

- CPS framework. The cyber-physical framework was applied to the design of structures under wind hazards but is expandable to design multi-hazard resistant structures with an accurate physical modeling.
- Cyber-physical systems. A large benefit of cyber-physical systems is the ability to deliver designs resilient to external loading. The research explored in this dissertation focuses on the application to individual structures. Expanding cyber-physical systems to consider community resilience subject to extreme natural hazards would better seize the opportunity to deliver sustainable, intelligent, and resilient infrastructure.

Bibliography

ACI/ASCE/TMS, *Building code requirements and specification for masonry structures: containing Building code requirements for masonry structures (TMS 402-11/ACI 530-11 / ASCE 5-11), Specification for mason structures (TMS 602-11 / ACI 530.1-11 / ASCE 6-11) and companion commentaries / developed by the Masonry Standards Joint Committee (MSJC)*. Boulder, Co., The Masonry Society, 2011.

Al-Hammouri, A. T. (2012). A comprehensive co-simulation platform for cyber-physical systems. *Computer Communications*, *36*(1), 8-19.

ASCE/SEI 7-16. (2017). Minimum design loads and associated criteria for buildings and other structures. Reston, VA: American Society of Civil Engineers.

ASCE. (2012). Wind tunnel testing for buildings and other structures. *ASCE 49-12*.

Banks, A., Vincent, J., & Anyakoha, C. (2008). A review of particle swarm optimization. Part II: hybridisation, combinatorial, multicriteria and constrained optimization, and indicative applications. *Natural Computing*, *7*(1), 109-124.

Bernardini, E., Spence, S. M., Kwon, D. K., & Kareem, A. (2015). Performance-based design of high-rise buildings for occupant comfort. *Journal of Structural Engineering*, *141*(10), 04014244.

Boggs, D., & Petersen, C. P. (1997). Acceleration indexes for human comfort in tall buildings–Peak or RMS. *CTBUH monograph*, 1-21.

Carassale, L., Freda, A., & Marrè-Brunenghi, M. (2014). Experimental investigation on the aerodynamic behavior of square cylinders with rounded corners. *Journal of fluids and structures*, *44*, 195-204.

Chan, C. M., Huang, M. F., & Kwok, K. C. (2009). Stiffness optimization for wind-induced dynamic serviceability design of tall buildings. *Journal of structural engineering*, *135*(8), 985-997.

Chang, F. K. (1973). Human response to motions in tall buildings. *Journal of the Structural Division*, *99*(6), 1259-1272.

Chen, P. W., & Robertson, L. E. (1972). Human perception thresholds of horizontal motion. *Journal of the structural division*, *92*(8), 1681-1695.

Chen, X., & Kareem, A. (2005). Dynamic wind effects on buildings with 3D coupled modes: application of high frequency force balance measurements. *Journal of Engineering Mechanics*, *131*(11), 1115-1125.

Cohen, D. (2019, July 15). About 60.2M Live in Areas Most Vulnerable to Hurricanes. Retrieved February 25, 2020, from https://www.census.gov/library/stories/2019/07/millions-of-americans-live-coastline-regions.html

Cook, N. J., & Mayne, J. R. (1980). A refined working approach to the assessment of wind loads for equivalent static design. *Journal of Wind Engineering and Industrial Aerodynamics*, *6*(1-2), 125-137.

Denoon, R. O., & Kwok, K. (2011). Implications of full-scale building motion experience for serviceability design. *Wind and Structures*, *14*(6), 537-557.

Erol, O. K., & Eksin, I. (2006). A new optimization method: big bang–big crunch. *Advances in Engineering Software*, *37*(2), 106-111.

ESDU. (1974). Characteristics of atmospheric turbulence near the ground. Part I: Definitions and general information. *Engineering Sciences Data Unit*, *Itm. No. 74030, 74031*.

Fernández-Cabán, P. L., & Masters, F. J. (2018). Hybridizing particle swarm and big bang-big crunch optimization methods to explore then exploit the design domain of large planar frame structures. *Computers & Structures*, *202*, 1-14.
Fernández-Cabán, P. L., & Masters, F. J. (2017). Near surface wind longitudinal velocity positively skews with increasing aerodynamic roughness length. *Journal of Wind Engineering and Industrial Aerodynamics*, *169*, 94-105.

Fourie, P. C., & Groenwold, A. A. (2002). The particle swarm optimization algorithm in size and shape optimization. *Structural and Multidisciplinary Optimization*, *23*(4), 259-267.

Gandomi, A. H., Yang, X. S., Talatahari, S., & Alavi, A. H. (2013). Metaheuristic algorithms in modeling and optimization. *Metaheuristic applications in structures and infrastructures*, 1-24.

Gavanski, E., Gurley, K. R., & Kopp, G. A. (2016). Uncertainties in the estimation of local peak pressures on low-rise buildings by using the Gumbel distribution fitting approach. *Journal of Structural Engineering*, *142*(11), 04016106.

Gierson, M. L., Phillips, B. M., Duthinh, D., & Ayyub, B. M. (2017). Wind-pressure coefficients on low-rise building enclosures using modern wind-tunnel data and Voronoi diagrams. *ASCE-ASME Journal of Risk and Uncertainty in Engineering Systems, Part A: Civil Engineering*, *3*(4), 04017010.

Griffis, L. G. (1993). Serviceability limit states under wind load. *Engineering Journal*, *30*(1), 1-16.

Hakuno, M., Shidawara, M., & Hara, T. (1969). "Dynamic destructive test of a cantilever beam controlled by an analog computer." Transactions of the Japan Society of Civil Engineers, 171:1-9 (In Japanese).

Hansen, R. J., Reed, J. W., & Vanmarcke, E. H. (1973). Human response to wind-induced motion of buildings. *Journal of the structural division*, *99*(7), 1589-1605.

He, S., Prempain, E., & Wu, Q. H. (2004). An improved particle swarm optimizer for mechanical design optimization problems. *Engineering optimization*, *36*(5), 585-605.

Huang, G., & Chen, X. (2007). Wind load effects and equivalent static wind loads of tall buildings based on synchronous pressure measurements. *Engineering Structures*, *29*(10), 2641-2653.

Huang, M. F., Chan, C. M., & Lou, W. J. (2012). Optimal performance-based design of wind sensitive tall buildings considering uncertainties. *Computers & structures*, *98*, 7-16.

Huang, M. F., Li, Q., Chan, C. M., Lou, W. J., Kwok, K. C., & Li, G. (2015). Performance-based design optimization of tall concrete framed structures subject to wind excitations. *Journal of Wind Engineering and Industrial Aerodynamics*, *139*, 70-81.

Hwang, C. L., & Masud, A. S. M. (2012). *Multiple objective decision making—methods and applications: a state-of-the-art survey* (Vol. 164). Springer Science & Business Media.

International Organization for Standardization. (2007). *Bases for Design of Structures--serviceability of Buildings and Walkways Against Vibrations*. ISO.

Irwin, A. W. (1981). Perception, comfort and performance criteria for human beings exposed to whole body pure yaw vibration and vibration containing yaw and translational components. *Journal of Sound and Vibration, 76*(4), 481-497.

Irwin, P. A. (2008). Bluff body aerodynamics in wind engineering. *Journal of Wind Engineering and Industrial Aerodynamics*, *96*(6-7), 701-712.

ISO, S. (1984). Guidelines for the evaluation of the response of occupants of fixed structures, especially buildings and off-shore structures, to low-frequency horizontal motion (0.063 to 1 Hz).

Kaimal, J. C. (1978). Horizontal velocity spectra in an unstable surface layer. *Journal of the Atmospheric Sciences*, *35*(1), 18-24.

Kalman, R. E. (1960). A new approach to linear filtering and prediction problems.

Kalman, R. E., & Bucy, R. S. (1961). New results in linear filtering and prediction theory.

Kareem, A., Kijewski, T., & Tamura, Y. (1999). Mitigation of motions of tall buildings with specific examples of recent applications. *Wind and structures*, *2*(3), 201-251.

Karimpour, A., Kaye, N. B., & Baratian-Ghorghi, Z. (2012). Modeling the neutrally stable atmospheric boundary layer for laboratory scale studies of the built environment. *Building and environment*, *49*, 203-211.

Kennedy, J., & Eberhart, R. (1995, November). Particle swarm optimization. In *Proceedings of ICNN'95-International Conference on Neural Networks* (Vol. 4, pp. 1942-1948). IEEE.

Kijewski-Correa, T., Pirnia, D., & Notre Dame, I. N. (2009, June). 'Pseudo-full-scale'evaluation of occupant comfort in tall buildings. In *Proceedings of 11th Americas conference on wind engineering, San Juan, Puerto Rico*.

Kim, J. E., Rao, V. N., Koomullil, R. P., Ross, D. H., Soni, B. K., & Shih, A. M. (2009). Development of an efficient aerodynamic shape optimization framework. *Mathematics and Computers in Simulation*, *79*(8), 2373-2384.

Kind, R. J. (1988). Worst suctions near edges of flat rooftops with parapets. *Journal of Wind Engineering and Industrial Aerodynamics*, *31*(2-3), 251-264.

Kopp, G. A., Surry, D., & Mans, C. (2005). Wind effects of parapets on low buildings: Part 1. Basic aerodynamics and local loads. *Journal of Wind Engineering and Industrial Aerodynamics*, *93*(11), 817-841.

Kopp, G. A., Mans, C., & Surry, D. (2005). Wind effects of parapets on low buildings: Part 2. Structural loads. *Journal of wind engineering and industrial aerodynamics*, *93*(11), 843-855.

Kopp, G. A., Mans, C., & Surry, D. (2005). Wind effects of parapets on low buildings: Part 4. Mitigation of corner loads with alternative geometries. *Journal of Wind Engineering and Industrial Aerodynamics*, *93*(11), 873-888.

Kwok, K. C., & Bailey, P. A. (1987). Aerodynamic devices for tall buildings and structures. *Journal of engineering mechanics*, *113*(3), 349-365.

Kwok, K. C., Hitchcock, P. A., & Burton, M. D. (2009). Perception of vibration and occupant comfort in wind-excited tall buildings. *Journal of Wind Engineering and Industrial Aerodynamics*, *97*(7-8), 368-380.

Lim, H. C., Castro, I. P., & Hoxey, R. P. (2007). Bluff bodies in deep turbulent boundary layers: Reynolds-number issues. *Journal of Fluid Mechanics*, *571*, 97-118.

Lin, S. L., Li, J., Elnashai, A. S., & Spencer Jr, B. F. (2012). NEES integrated seismic risk assessment framework (NISRAF). *Soil Dynamics and Earthquake Engineering*, *42*, 219-228.

Lu, Z., Wang, D. C., Masri, S. F., & Lu, X. L. (2016). An experimental study of vibration control of wind-excited high-rise buildings using particle tuned mass dampers. *Smart Struct. Syst*, *18*(1), 93-115.

Luque, M., Miettinen, K., Eskelinen, P., & Ruiz, F. (2009). Incorporating preference information in interactive reference point methods for multiobjective optimization. *Omega*, *37*(2), 450-462.

Luenberger, D. G., & Ye, Y. (1984). *Linear and nonlinear programming* (Vol. 2). Reading, MA: Addison-wesley.

Luke, S. (2013). *Essentials of metaheuristics* (Vol. 2). Raleigh: Lulu.

Mans, C., Kopp, G. A., & Surry, D. (2005). Wind effects of parapets on low buildings: Part 3. Parapet loads. *Journal of wind engineering and industrial aerodynamics*, *93*(11), 857-872.

McNamara, R., Kareem, A., & Kijewski, T. (2002). Ask the experts... Perception of motion criteria for tall buildings subjected to wind: A panel discussion.

Melbourne, W. H., & Palmer, T. R. (1992). Accelerations and comfort criteria for buildings undergoing complex motions. *Journal of wind engineering and industrial aerodynamics*, *41*(1-3), 105-116.

Mendis, P., Ngo, T., Haritos, N., Hira, A., Samali, B., & Cheung, J. (2007). Wind loading on tall buildings. *Electronic Journal of Structural Engineering*.

Merrick, R., & Bitsuamlak, G. (2009). Shape effects on the wind-induced response of high-rise buildings. *Journal of wind and engineering*, *6*(2), 1-18.

Miettinen, K. (1999). *Nonlinear Multiobjective Optimization* (Vol. 12). Springer Science & Business Media.

Mooneghi, M. A., Irwin, P., & Chowdhury, A. G. (2016). Partial turbulence simulation method for predicting peak wind loads on small structures and building appurtenances. *Journal of Wind Engineering and Industrial Aerodynamics*, *157*, 47-62.

Mooneghi, M. A., & Kargarmoakhar, R. (2016). Aerodynamic mitigation and shape optimization of buildings. *Journal of building engineering*, *6*, 225-235.

Muyl, F., Dumas, L., & Herbert, V. (2004). Hybrid method for aerodynamic shape optimization in automotive industry. *Computers & Fluids*, *33*(5-6), 849-858.

Nakashima, M., Kato, H., & Takaoka, E. (1992). Development of real-time pseudo dynamic testing. *Earthquake Engineering & Structural Dynamics*, *21*(1), 79-92.

National Research Council of Canada. (2010). User's guide—National Building Code 2010, Structural Commentaries (Part 4 of Division B), Ottawa.

National Weather Service. (2001). Summary of natural hazard statistics for 2000 in the United States.

National Weather Service. (2002). Summary of natural hazard statistics for 2001 in the United States.

National Weather Service. (2003). Summary of natural hazard statistics for 2002 in the United States.

National Weather Service. (2004). Summary of natural hazard statistics for 2003 in the United States.

National Weather Service. (2005). Summary of natural hazard statistics for 2004 in the United States.

National Weather Service. (2007). Summary of natural hazard statistics for 2005 in the United States.

National Weather Service. (2008). Summary of natural hazard statistics for 2006 in the United States.

National Weather Service. (2016). Summary of natural hazard statistics for 2007 in the United States.

National Weather Service. (2016). Summary of natural hazard statistics for 2008 in the United States.

National Weather Service. (2016). Summary of natural hazard statistics for 2009 in the United States.

National Weather Service. (2016). Summary of natural hazard statistics for 2010 in the United States.

National Weather Service. (2016). Summary of natural hazard statistics for 2011 in the United States.

National Weather Service. (2016). Summary of natural hazard statistics for 2012 in the United States.

National Weather Service. (2016). Summary of natural hazard statistics for 2013 in the United States.

National Weather Service. (2016). Summary of natural hazard statistics for 2014 in the United States.

National Weather Service. (2016). Summary of natural hazard statistics for 2015 in the United States.

National Weather Service. (2017). Summary of natural hazard statistics for 2016 in the United States.

National Weather Service. (2018). Summary of natural hazard statistics for 2017 in the United States.

National Weather Service. (2019). Summary of natural hazard statistics for 2018 in the United States.

Nazareth, L., & Tseng, P. (2002). Gilding the lily: a variant of the Nelder-Mead algorithm based on golden-section search. *Computational Optimization and Applications*, *22*(1), 133-144.

Perez, R. E., & Behdinan, K. (2007). Particle swarm optimization in structural design. *Swarm intelligence: Focus on ant and particle swarm optimization*, (532).

Pindado, S., & Meseguer, J. (2003). Wind tunnel study on the influence of different parapets on the roof pressure distribution of low-rise buildings. *Journal of Wind Engineering and Industrial Aerodynamics*, *91*(9), 1133-1139.

Rathje, E. M., Dawson, C., Padgett, J. E., Pinelli, J. P., Stanzione, D., Adair, A., ... & Esteva, M. (2017). DesignSafe: new cyberinfrastructure for natural hazards engineering. *Natural Hazards Review*, *18*(3), 06017001.

Shi, Y., & Eberhart, R. (1998, May). A modified particle swarm optimizer. In *1998 IEEE international conference on evolutionary computation proceedings. IEEE world congress on computational intelligence (Cat. No. 98TH8360)* (pp. 69-73). IEEE.

Shi, Y., & Eberhart, R. C. (1998, March). Parameter selection in particle swarm optimization. In *International conference on evolutionary programming* (pp. 591-600). Springer, Berlin, Heidelberg.

Shing, P. S., & Mahin, S. A. (1984). *Pseudodynamic test method for seismic performance evaluation: theory and implementation*. Verlag nicht ermittelbar.

Shing, P. B., Nakashima, M., & Bursi, O. S. (1996). Application of pseudodynamic test method to structural research. *Earthquake spectra*, *12*(1), 29-56.

Simiu, E. (2011). *Design of buildings for wind: A guide for ASCE 7-10 standard users and designers of special structures*. John Wiley & Sons.

Song, W., & Dyke, S. (2013). Development of a cyber-physical experimental platform for real-time dynamic model updating. *Mechanical Systems and Signal Processing*, *37*(1-2), 388-402.

Spence, S. M., & Gioffrè, M. (2012). Large scale reliability-based design optimization of wind excited tall buildings. *Probabilistic Engineering Mechanics*, *28*, 206-215.

Spence, S. M., & Kareem, A. (2014). Performance-based design and optimization of uncertain wind-excited dynamic building systems. *Engineering Structures*, *78*, 133-144.

Stathopoulos, T., & Baskaran, A. (1987). Wind pressures on flat roofs with parapets. *Journal of Structural Engineering*, *113*(11), 2166-2180.

Stathopoulos, T., & Surry, D. (1983). Scale effects in wind tunnel testing of low buildings. *Journal of Wind Engineering and Industrial Aerodynamics*, *13*(1-3), 313-326.

Stathopoulos, T., Saathoff, P., & Du, X. (2002). Wind loads on parapets. *Journal of Wind Engineering and Industrial Aerodynamics*, *90*(4-5), 503-514.

Takanashi, K., & Nakashima, M. (1987). Japanese activities on on-line testing. *Journal of Engineering Mechanics*, *113*(7), 1014-1032.

Talbi, E. G. (2009). *Metaheuristics: from design to implementation* (Vol. 74). John Wiley & Sons.

Tanaka, H., Tamura, Y., Ohtake, K., Nakai, M., Kim, Y. C., & Bandi, E. K. (2013). Aerodynamic and flow characteristics of tall buildings with various unconventional configurations. *International Journal of High-Rise Buildings*, *2*(3), 213-228.

Tieleman, H. W. (2003). Wind tunnel simulation of wind loading on low-rise structures: a review. *Journal of wind engineering and industrial aerodynamics*, *91*(12-15), 1627-1649.

Tse, K. T., Hitchcock, P. A., Kwok, K. C., Thepmongkorn, S., & Chan, C. M. (2009). Economic perspectives of aerodynamic treatments of square tall buildings. *Journal of Wind Engineering and Industrial Aerodynamics*, *97*(9-10), 455-467.

Venter, G., & Sobieszczanski-Sobieski, J. (2003). Particle swarm optimization. *AIAA journal*, *41*(8), 1583-1589.

Von Karman, T. (1948). Progress in the statistical theory of turbulence. *Proceedings of the National Academy of Sciences of the United States of America*, *34*(11), 530.

Whiteman, M. L., Phillips, B. M., Fernandez-Caban, P. L., Masters, F. J., Bridge, J. A., & Davis, J. R. (2018). Optimal design of structures using cyber-physical wind tunnel experiments with mechatronic models. *Journal of Wind Engineering and Industrial Aerodynamics*, *172*, 441-452.

Yang, J. N., Agrawal, A. K., Samali, B., & Wu, J. C. (2004). Benchmark problem for response control of wind-excited tall buildings. *Journal of engineering mechanics*, *130*(4), 437-446.

Yeniay, Ö. (2005). Penalty function methods for constrained optimization with genetic algorithms. *Mathematical and computational Applications*, *10*(1), 45-56.

Zhou, A., Qu, B. Y., Li, H., Zhao, S. Z., Suganthan, P. N., & Zhang, Q. (2011). Multiobjective evolutionary algorithms: A survey of the state of the art. *Swarm and Evolutionary Computation*, *1*(1), 32-49.

ZOC33 miniature pressure scanner. (2016). Retrieved from http://scanivalve.com/products/pressure-measurement/miniature-analog-pressure-scanners/zoc33-miniature-pressure-scanner/